

POLITECNICO DI MILANO

Scuola di Ingegneria Industriale e dell'Informazione

Corso di laurea in Ingegneria Biomedica



Probing lipid ordering by polarized third-harmonic generation microscopy

Relatore: Chiar.mo Prof. Rinaldo CUBEDDU

Tesi di Laurea Magistrale di:

Marco GRASSO

Matricola 799025

Anno Accademico 2013 - 2014

“Dubium sapientiae initium”

Renè Descartes

Abstract

II Faculty of Engineering

Department of Physics

Master of Science in Biomedical Engineering

By Marco Grasso

The present thesis focuses on the experimental study of the ordering of artificial lipid droplets with diseased-related composition by third harmonic generation microscopy.

Triacylglycerol-enriched and cholesteryl esters-enriched lipid droplets have been considered in this work because these lipid droplets are the most clinically relevant lipid constituents found in cells and tissues. Such lipid bodies are hallmarks of the most common lipid-related disorders worldwide.

Third harmonic generation microscopy has recently been the center of a renovated interest as a probe of the micrometer-scale organization of lipids in biological systems, due to its intrinsic optical sectioning capability and the fact that it does not require sample labeling, along with the achievement of high penetration depths in scattering tissues without an appreciable loss in spatial resolution.

Moreover, the combination of this technique with other multiphoton microscopies such as two photon excited fluorescence and coherent anti-Stokes Raman scattering provides a complete framework of structural and functional information about the sample under investigation.

In this work, linearly and circularly polarized laser light has been used as excitation source. The results demonstrated that circular polarization provides best image contrast in anisotropic samples. The structural information on artificial lipid droplets drawn by using third harmonic generation microscopy can efficiently contribute to the study of the sub-cellular arrangement of lipids in real biological tissues.

In particular, the present work aims at providing new insights on the organization of these biomolecules in tissues affected by lipid-related disorders.

The first chapter of the thesis presents an overview of the lipid droplets biology and a description of the principal non-optical and optical techniques for investigating the ordering in samples containing lipid droplets.

In the second chapter, third harmonic generation microscopy is considered in more detail. The theoretical background is given and the fundamental works that have been conducted in this field are taken into account, with a particular emphasis on the contrast mechanisms typical of this microscopy technique.

The third chapter specifically introduces the materials, i.e. the lipid droplets, and the nonlinear microscope setup used for the experimental measurements.

In the fourth chapter a showcase of the experimental THG results of the varied lipid samples and its relevant discussions are presented.

The last chapter summarizes the thesis. Future insights and recommendations are also included.

Abstract: Versione italiana

Questo lavoro di tesi si focalizza sullo studio sperimentale dell'ordinamento spaziale di corpi lipidici artificiali aventi una composizione chimica tipica di quelli che caratterizzano tessuti affetti da patologie lipido-correlate. Questo studio è svolto mediante la tecnica di microscopia di generazione di terza armonica.

In questo lavoro sono stati considerati corpi lipidici composti da trigliceridi ed esteri del colesterolo perché essi sono i costituenti lipidici più clinicamente rilevanti in cellule e tessuti. Infatti, tali corpi lipidici rappresentano i segni più comuni di patologie lipido-correlate.

La microscopia di generazione di terza armonica è stata, recentemente, il centro di un rinnovato interesse in quanto è in grado di indagare l'organizzazione, su scala micrometrica, di lipidi in sistemi biologici. Ciò è dovuto alla sua intrinseca capacità di sezionamento ottico, al fatto che non richiede il "labeling" del campione e all'ottenimento di elevate profondità di penetrazione in tessuti ad alto scattering senza una riduzione significativa della risoluzione spaziale.

Inoltre, la combinazione di tale tecnica con altre microscopie multifotoniche come two photon excited fluorescence e coherent anti-Stokes Raman scattering forniscono un panorama completo di informazioni strutturali e funzionali riguardo al campione in oggetto.

In questo lavoro, un laser a polarizzazione lineare e circolare è stato utilizzato come sorgente di eccitazione. I risultati mostrano che la polarizzazione circolare è associata al miglior contrasto d'immagine in campioni che esibiscono elevata anisotropia. Le informazioni strutturali su questi corpi lipidici artificiali ottenute attraverso la tecnica sopra menzionata possono efficientemente contribuire allo studio dell'ordinamento sub-cellulare di lipidi in tessuti biologici reali. In particolare, questo lavoro mira a fornire nuove conoscenze sull'organizzazione di queste biomolecole in tessuti affetti da patologie lipido-correlate.

Il primo capitolo della tesi fornisce una panoramica della biologia dei corpi lipidici e una descrizione delle principali tecniche ottiche e non ottiche per studiare l'ordinamento spaziale in campioni contenenti corpi lipidici.

Nel secondo capitolo, la microscopia di generazione di terza armonica è presa in considerazione con maggior dettaglio. Il background teorico e i lavori fondamentali che sono stati svolti in questo ambito vengono presentati, con un'attenzione particolare ai meccanismi di contrasto tipici di tale microscopia.

Il terzo paragrafo introduce specificatamente i materiali, ossia i corpi lipidici, e il setup di microscopia non lineare utilizzato per le misure sperimentali.

Il quarto capitolo si concentra sui risultati sperimentali derivanti da misure su diversi campioni lipidici e sulle relative discussioni.

L'ultimo capitolo riassume la tesi. Sviluppi futuri e indicazioni di lavoro sono inclusi in tale capitolo.

Acknowledgements

This work has been conducted during the academic year 2013/2014 at the Optics Laboratory of Tampere University of Technology (TUT), at Tampere, Finland.

First of all, I would like to thank Prof. Rinaldo Cubeddu for helping me finding a suitable thesis topic abroad and for his advices. At the same time, a special thanks to Prof. Martti Kauranen for accepting me as a research visitor at the Optics Laboratory.

My most profound thanks to Dr. Godofredo Bautista for being my guide throughout the experiments and the thesis writing. Your advices have been priceless to me. Thank you also for your patience. Without you this work would have not be possible.

I would also like to thank Dr. Abdallah Slablab and Dr. Matti Virkki for letting me use their microscopy tools during the experiments.

Thanks to Prof. Elina Ikonen for the visit to her research group at the Institute of Biomedicine, University of Helsinki, Finland. Thanks to Dr. Ranjan Sanjeev for helping me with the sample preparation.

Finally, special thanks to my family and friends for constantly supporting me throughout the year abroad.

Content

Chapter 1: Overview	1
1.1 Introduction	3
1.2 Biomolecules and lipids	4
1.3 Biology of a lipid droplet	6
1.4 Lipid ordering	10
1.5 Non-optical methods for investigating lipid ordering.....	11
1.6 Optical techniques	14
Chapter 2: THG microscopy	27
2.1 Principles in imaging.....	29
2.2 Application in LD imaging.....	35
Chapter 3: Materials and Methods	43
3.1 LD samples	45
3.2 Sample preparation.....	46
3.3 THG microscopy setup.....	48

Chapter 4: Experimental THG imaging of various lipid samples and discussion.....51

4.1 Polarized THG imaging of LDs53

 4.1.1 TAG-enriched lipid droplets53

 4.1.2 CE-enriched lipid droplets58

 4.1.3 Mixed TAG and CE-enriched lipid droplets66

4.2 THG-CD imaging of LDs.....76

 4.1.1 TAG-enriched lipid droplets77

 4.1.2 CE-enriched lipid droplets80

 4.1.3 Mixed TAG and CE-enriched lipid droplets84

4.3 Polarized THG imaging of lipid films89

Chapter 5: Conclusions93

References95

List of Figures

1.1 Chemical structure of glycerol and fatty acids.....	4
1.2 Lipid shape and supramolecular organization (polymorphism)	5
1.3 Basic architecture of a LD	7
1.4 Deaths by cause (2012 in Europe).....	10
1.5 Basic setup of a typical confocal microscope that uses fluorescence to generate signal contrast	14
1.6 Jablonski diagrams for TPEF, SHG, THG and CARS	19
1.7 Linear and nonlinear excitation	23
1.8 Simplified setup of a typical nonlinear optics microscope for coherent processes	25
2.1 THG intensity versus axial position for a thin film of index-matching oil between two glass plates	31
2.2 SHG and the anisotropy parameter as a function of sample (GaAs (001) crystal) position	33
2.3 Images of single larval spicules using linearly and circularly polarized light	34
2.4 (a) Experimental setup, showing trans and epi-detection modalities. (b) Dependence of the ratio epi/trans THG signal on the number of scattering mean free paths	38
2.5 Normalized electric field and intensity distributions of a tightly focused Gaussian beam at the focal plane	41
3.1 Basic chemical structure of agarose	47
3.2 THG microscope setup	48
4.1 Experimental TAG images (site 1).....	54

4.2 Experimental TAG images (site 2, $z = 10 \mu\text{m}$)	55
4.3 Experimental TAG images (site 2, $z = 12 \mu\text{m}$)	56
4.4 Experimental TAG images (site 2, $z = 14 \mu\text{m}$)	57
4.5 Experimental CE images (site 1, $z = 8.4 \mu\text{m}$)	59
4.6 Experimental CE images (site 1, $z = 10.4 \mu\text{m}$)	60
4.7 Experimental CE images (site 1, $z = 12.4 \mu\text{m}$)	61
4.8 Experimental CE images (site 2, $z = z = 10 \mu\text{m}$)	62
4.9 Experimental CE images (site 2, $z = 12 \mu\text{m}$)	63
4.10 Experimental CE images (site 2, $z = 14 \mu\text{m}$)	64
4.11 Experimental CE images (site 2, $z = 16 \mu\text{m}$)	65
4.12 Experimental TAG/CE images (site 1, $z = 8.5 \mu\text{m}$).....	67
4.13 Experimental TAG/CE images (site 1, $z = z = 10 \mu\text{m}$).....	68
4.14 Experimental TAG/CE images (site 1, $z = z = 11.5 \mu\text{m}$).....	69
4.15 Experimental TAG/CE images (site 2, $z = 10 \mu\text{m}$).....	71
4.16 Experimental TAG/CE images (site 2, $z = 12 \mu\text{m}$).....	72
4.17 Experimental TAG/CE images (site 2, $z = 14 \mu\text{m}$).....	73
4.18 Experimental TAG/CE images (site 2, $z = 16 \mu\text{m}$).....	74
4.19 Experimental TAG/CE image taken by varying linear polarization between two orthogonal directions.....	75
4.20 THG-CD image of a TAG sample (site 1)	78
4.21 THG-CD image of a TAG sample (site 2, $z = 10 \mu\text{m}$)	78
4.22 THG-CD image of a TAG sample (site 2, $z = 12 \mu\text{m}$)	79
4.23 THG-CD image of a TAG sample (site 2, $z = 14 \mu\text{m}$)	79
4.24 THG-CD image of a CE sample (site 1, $z = 8.4 \mu\text{m}$).....	81
4.25 THG-CD image of a CE sample (site 1, $z = 10.4 \mu\text{m}$).....	81

4.26 THG-CD image of a CE sample (site 1, $z = 12.4 \mu\text{m}$).....	82
4.27 THG-CD image of a CE sample (site 2, $z = 10 \mu\text{m}$).....	82
4.28 THG-CD image of a CE sample (site 2, $z = 12 \mu\text{m}$).....	83
4.29 THG-CD image of a CE sample (site 2, $z = 14 \mu\text{m}$).....	83
4.30 THG-CD image of a CE sample (site 2, $z = 16 \mu\text{m}$).....	84
4.31 THG-CD image of a TAG/CE sample (site 1, $z = 8.5 \mu\text{m}$)	85
4.32 THG-CD image of a TAG/CE sample (site 1, $z = 10 \mu\text{m}$)	85
4.33 THG-CD image of a TAG/CE sample (site 1, $z = 11.5 \mu\text{m}$)	86
4.34 THG-CD image of a TAG/CE sample (site 2, $z = 10 \mu\text{m}$)	86
4.35 THG-CD image of a TAG/CE sample (site 2, $z = 12 \mu\text{m}$)	87
4.36 THG-CD image of a TAG/CE sample (site 2, $z = 14 \mu\text{m}$)	87
4.37 THG-CD image of a TAG/CE sample (site 2, $z = 16 \mu\text{m}$)	88
4.38 Image of a CE lipid film taken by keeping constant the direction of the linear polarization and by varying the plane of imaging	89
4.39 Experimental THG image of a CE lipid film taken with left and right circular polarization ($z = 8 \mu\text{m}$).....	90
4.40 Experimental THG image of a CE lipid film taken with left and right circular polarization ($z = 9 \mu\text{m}$).....	90
4.41 Experimental THG image of a CE lipid film taken with left and right circular polarization ($z = 11 \mu\text{m}$).....	91
4.42 Experimental THG image of a CE lipid film taken with left and right circular polarization ($z = 12 \mu\text{m}$).....	91
4.43 THG-CD image of a CE lipid film at varying depth z	92

List of abbreviations

3D	Three Dimensional
CARS	Coherent Anti-Stokes Raman Scattering
CE	Cholesteryl Ester
CD	Circular Dichroism
CVD	CardioVascular Disease
LD	Lipid Droplet
MLV	MultiLamellar Lipid Vescicle
MPM	MultiPhoton Microscopy
NA	Numerical Aperture
NLO	NonLinear Optics
P-THG	Polarized Third Harmonic Generation
SHG	Second Harmonic Generation
TAG	TryAcylGlycerol
THG	Third Harmonic Generation
TPEF	Two-Photon Excited Fluorescence

Chapter 1

Overview

In the following, a complete overview of the fundamental elements that constitute the framework of this thesis is presented. After the introduction, biomolecules and in particular lipids are considered, with a special emphasis on their structure, function and on the disorders associated to them. The overview then continues with a description of the biology of a lipid droplet, which is essential to understand in order to interpret the THG images. The concept of ordering of lipids in biological tissues is also introduced. The level of ordering can be studied both by means of nonoptical and optical techniques, both of which are presented in the last two sections of this chapter.

1.1 Introduction

In the world of biological imaging, recent improvements in multiphoton microscopy (MPM) techniques opened a rapidly expanding field of imaging studies for probing molecular order in intact biological tissue. Some of the most widely used MPM techniques are two-photon excited fluorescence (TPEF), second and third-harmonic generation (SHG and THG, respectively) and coherent anti-Stokes Raman scattering (CARS). Such techniques involve nonlinear optical processes in the sense that the rate at which they occur depends nonlinearly on the input light intensity. As mentioned, these techniques are particularly suitable for biological samples, providing inherent 3D resolution and previously unachieved penetration depths without encountering common issues such as photodamage. Moreover, they do not require the labeling with fluorescent dyes (they are “label-free”), because the harmonic signals result from spontaneous light-matter interaction processes within a material, given that the intensity of the incident beam is sufficiently high. Although TPEF is label-free, the technique is still limited to autofluorescent samples which emit isotropically.

In particular, there has been a growing interest in SHG and THG microscopies, mostly because these methods are able to highlight symmetry-sensitive features within the sample. In fact SHG and THG rely on distinct and novel contrast mechanisms (e.g. non-centrosymmetric structures sensitivity for SHG and presence of interfaces, inhomogeneity and anisotropy for

THG) that can be easily combined to provide an overall picture of the sub-cellular organization and ordering of various components in complex samples.

The present thesis focuses on the use of THG microscopy as a probe of structural ordering in artificially-prepared lipid droplets. Solution of triglycerides and cholesterol esters immersed in agarose gel were considered in this study, because these are the lipids most often found in tissues affected by lipid-related disorders, e.g. tuberculosis and atherosclerosis. It is shown that these LDs are the main source of THG contrast and that the mentioned solutions provide a useful model to study the structures and the degree of anisotropy of lipids. This information may then be applied to gain insights on the micro-scale arrangement of lipids in healthy and diseased tissues.

1.2 Biomolecules and lipids

Lipids are made of one, two or three fatty acids (monoglycerides, diglycerides and triglycerides, respectively) attached to a molecule of glycerol. The fatty acids consist of a long hydrocarbon chain with a terminal carboxyl group; if they contain only single covalent bonds, they are termed saturated fatty acids, otherwise they are termed unsaturated fatty acids. The chemical structure of glycerol and fatty acids is shown in Figure 1.1.

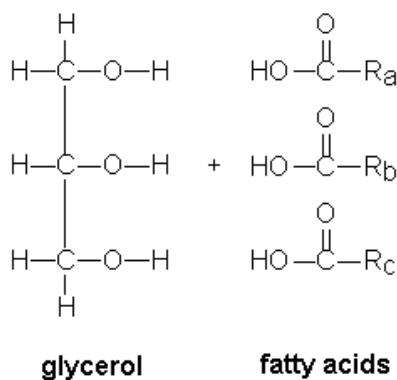


Figure 1.1: Chemical structure of glycerol and fatty acids. R_a, R_b and R_c represent three alkyl group side chains.

[1]

Chapter 1: *Overview*

Given this chemical structure, it is clear that fatty acids are non-polar and thus highly hydrophobic, whereas glycerol is polar and thus hydrophilic. Therefore, lipids are amphipathic molecules. Hydrophobic moieties of lipids self-associate and hydrophilic moieties tend to interact with water: this behavior represents the physical principle of the spontaneous formation of the lipid bilayer in cell membranes. Of course lipids self-organize so as to reach an energy minimum for the structure they form.

Lipids can form different supramolecular structures [2], depending on the molecular shape assumed by the single lipid molecule (e.g. inverted cone, cylindrical shape and conical). This is depicted in Figure 1.2.

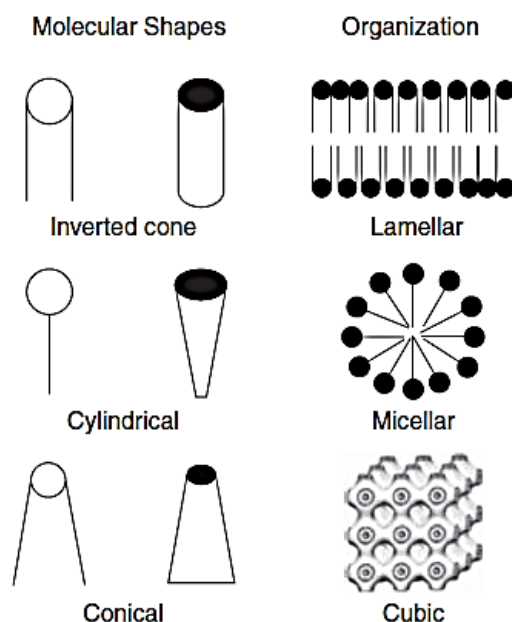


Figure 1.2: Lipid shape and supramolecular organization (polymorphism). The lamellar organization represents the bilayer structure found in cells' membranes. [2]

An important class of lipids are sterols, such as cholesterol, and phospholipids. Both of them play a key role as structural components of mammalian cells. In particular, how cholesterol affects the membrane's physical properties has been a field of active research [3], [4]. Another interesting field of study relates to how lipids are arranged in the bilayer of cells'

membranes and how these lipid domains interact with the other organelles. This last question is of timely interest in the medical field, since knowing the lipid arrangement in the 3D space provides the clinician with a powerful tool to monitor lipid-related disorders. It has been shown [5] that the self-organizing properties of some lipids (e.g., cholesterol and sphingolipids) drive the formation of specialized domains within cellular membranes; in particular, these lipids self-associate to form condensed, liquid-ordered domains, also called lipid “rafts” [6] within the more fluid environment of the rest of the membrane. These domains are involved in signal transduction, protein sorting and membrane transport. All of these findings suggest that lipids are not mere building blocks in cells but act as regulatory elements.

Apart from being located in cellular membranes, lipids are also found clustered within organelles called lipid droplets, which are introduced in the next paragraph.

1.3 Biology of a lipid droplet

Lipid droplets (LD) are intracellular and cytoplasmic organelles that contain neutral lipids in their core. Their size usually ranges from 1 μm up to 20 μm in diameter, although less than 200 nm-sized droplets can also be found in cells [7]. The core is highly hydrophobic and it is surrounded by a monolayer of polar lipids [8], [9]. This feature contrasts with the structure of other vesicular organelles that are typically characterized by an aqueous core enclosed in a phospholipid bilayer. The LD monolayer is made of different types of phospholipids, such as phosphatidylcholine (PE) and phosphatidylethanolamine (PE). Free-cholesterol (FC) is also likely to be in the LD surface monolayer. Moreover, this monolayer also contains a set of proteins, namely, peripheral membrane proteins (PAT proteins), tail-interacting protein (TIP47), which serve regulatory purposes, proteins related to signaling and cytoskeletal proteins.

With regard to the core of the LD, it is usually composed of several lipid esters, such as triacylglycerol (TAG), diacylglycerol (DG) and cholesterol ester (CE), which are found in different proportions depending on the cell. For example, in white adipocytes, TAG is the

most abundant lipid ester. A very interesting fact is that these lipid esters have heterogeneous properties like the melting point. This results in the formation of typical structural patterns (e.g., multiple fracture planes of onion skin appearance) during the sample preparation. Another consequence associated with the melting point is a thermodynamically complex behavior (e.g., studies [10] of tertiary systems containing cholesterol, CE and TAG showed that the melting point of saturated, high melting CE is depressed by unsaturated, low melting CE and TAG). In addition, the core exhibits structural heterogeneities among LDs: for instance, membrane bound to ribosomes have been observed inside the mast cell LD [11]. This fact may suggest that a possible origin of the LDs is the endoplasmic reticulum (ER). In this case, we can consider the LD's biogenesis as the budding of a lipid ester globule covered by the cytoplasmic leaflet of the ER membrane [10].

The structure of a typical LD is shown in Figure 1.3.

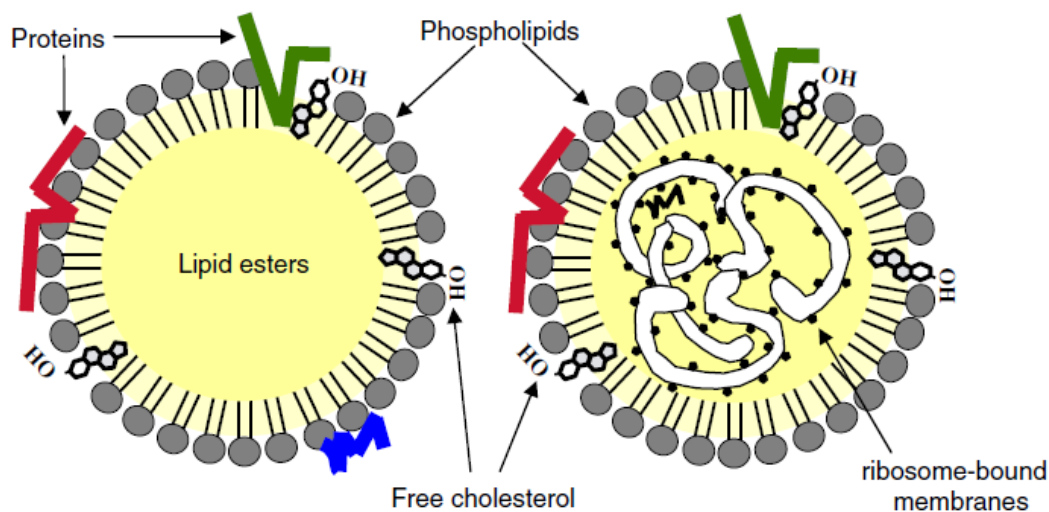


Figure 1.3: Basic architecture of a lipid droplet. Both lipid ester alone and ribosome-bound membranes have been observed as fundamental structures of the core, which is surrounded by a phospholipid monolayer with proteins and free cholesterol molecules attached to it. [7]

The general function associated with LDs is storage of lipid esters. Studies [12] confirmed that the synthesis of lipid esters and their accumulation in LDs are not only for later lipid utilization but act as a defense mechanism for the cell against saturated free fatty

acids (FAs), in order to prevent lipotoxicity. In fact, newly synthesized unsaturated FAs can protect the cell against saturated FAs by promoting TAG production and accumulation in LDs. Moreover, other studies [13] suggest that some metabolic reactions and lipid synthesis also occur within LDs.

Now, depending on the particular cell in which LDs are located, they serve other interesting functions. For example, in the hepatocyte lipid esters in the LDs are utilized for lipoprotein formation. In steroidogenic cells, CE in LDs are used for steroid synthesis. It has been shown [13] that some LD-associated proteins (among which the PAT proteins mentioned above) cause the clustering of LDs, their fusion into fewer and larger droplets and the subsequent accumulation of TG. The same clustering process can be triggered by other events, such as the release of a virus, e.g. Hepatitis C virus, in a cell [14]. It is thus straightforward to conclude that the LDs are not static organelles but they play an active role in lipid homeostasis.

Disorders in LDs function yields to several diseases, which are pandemic in many countries. For example, an elevated expression of Perilipin, another LD associated protein, is found in obese animals and humans. This fact suggests that *obesity* is a disorder caused by both environmental and genetic factors. Obesity is a disorder affecting heavily the US's population. In fact, a recent report [15] pointed out that the estimated prevalence of overweight and obesity in US adults (≥ 20 years) is 154.7 million and that nearly 35% of US adults are obese (body mass index ≥ 30 kg/m²). Obesity is associated with marked excess mortality in the US.

Another example is the *neutral lipid storage disease*, which is characterized by a TAG deposition in multiple tissues, though not in the adipose tissue. In addition, *lipodystrophy* is a disorder characterized by an abnormal, degenerative condition of the adipose tissue or sometimes by the total lack of adipose tissue. Both neutral lipid storage disease and lipodystrophy are mainly due to genetic mutation of specific LD-related proteins.

It is also reported [16] that TAG-rich LDs highly accumulate in lung macrophages which have been infected with *Mycobacterium tuberculosis* (Mtb); in fact, it is known that a lipid-rich microenvironment is typically the storage form of energy for this bacterium.

Tuberculosis is a widespread pulmonary disease, which affects roughly 11 million people worldwide; nearly 1.8 million deaths are due to tuberculosis, as recently estimated by the World Health Organization.

Lipids are also specific structural components of *atherosclerotic plaques* [17]. Atherosclerosis is an inflammatory disease characterized by the thickening of artery walls due to the accumulation of calcium and lipids within the artery. The exact process explaining this phenomenon is not fully understood but it is known that the early stages of atherosclerosis development are triggered by a subendothelial retention of atherogenic lipoproteins, which are responsible for the transport of fats along the bloodstream [18]. Cholesterol, CE and TAG are the most common lipids found in the plaques, although a remarkable content of phospholipids has also been reported [19]. Depending on the stage of development of the plaque, its composition varies from a liquid and liquid crystalline droplets to more solid material made of crystalline cholesterol and amorphous CE and TAG. In early stages, atherosclerosis is typically characterized by a large accumulation of lipids, especially CE, in isotropic and birefringent droplets.

Advanced stages of atherosclerosis yields to infarction (e.g, myocardial infarction or stroke if the involved artery is located in the brain) and it is considered as the major cause of cardiovascular disease (CVD). CVD is the first cause of death in Europe as reported by a recent study [20]. This fact is depicted in Figure 1.4.

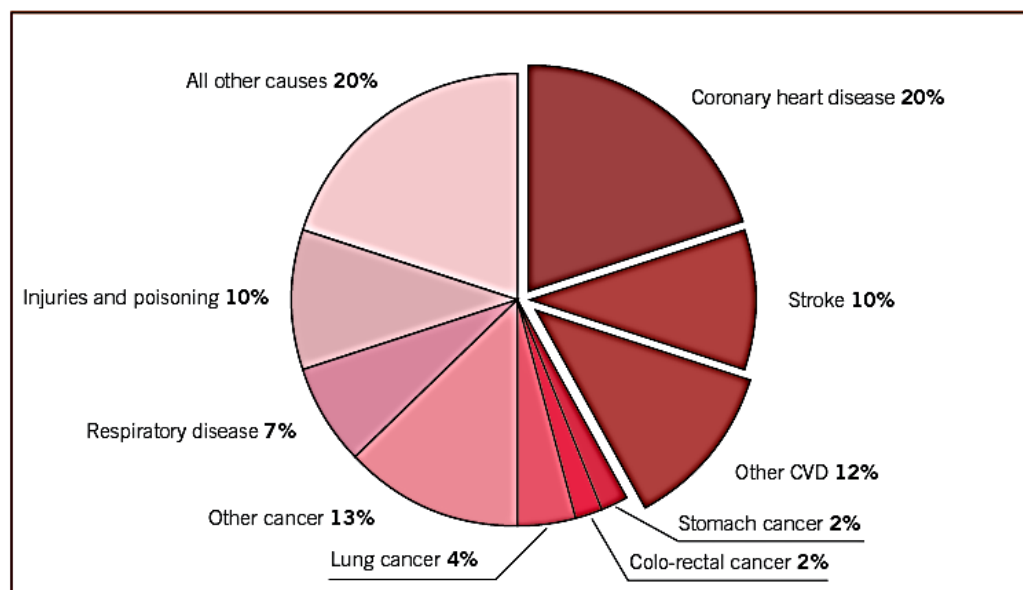


Figure 1.4: Deaths by cause (2012 in Europe). CVD (coronary heart disease, stroke and other CVD) makes up 42% of the total deaths. [20]

It is thus of fundamental importance to develop new characterization and imaging systems that are able to identify and probe the molecular order of lipid assemblies in biological tissues: in this way, monitoring lipid-related disorders would be facilitated and it would allow for a rapid medical intervention.

In the next paragraphs we first clarify the concept of lipid ordering. Then, we move on to describe non-optical methods for studying LDs. Finally, we consider the linear and nonlinear optical techniques used to probe lipid ordering.

1.4 Lipid ordering

Lipid ordering refers to the 3D spatial organization of lipids in biological tissues. As described earlier, lipids are mostly found in cells membranes and within lipid droplets. In both cases it is interesting to study how lipids spatially self-organize, whether by forming specific clusters or

by spreading along the whole available space. Already during the '90s [7] it was shown that lipids, in particular sphingolipids and cholesterol, are asymmetrically distributed over the exoplasmic and cytoplasmic leaflets of the cell membrane. They also form microdomains within the fluid environment of the bilayer. These microdomains act as platforms for the attachment of proteins and play important roles in signal transduction. As far as LDs are concerned, lipids can be organized in various levels of ordering, ranging from nearly isotropic (disordered) structures to anisotropic (ordered) ones. All of these different conditions can be studied by means of non-optical and optical techniques. The first are introduced in the next section.

1.5 Non-optical methods for investigating lipid ordering

Already during the '70s, *X-ray diffraction* was a popular technique for studying the arrangement and the physical state of lipid molecules within LD. This method is based on the detection and analysis of the scattered X-rays that hit a given sample as a function of different parameters, such as energy, incidence angle, wavelength and polarization. From the diffraction pattern it is possible to extract information about the crystal lattice, i.e. how the atoms are spatially arranged in the crystal, and also on the electronic band structure of the material. In the context of measurements on biological samples, CE in fatty streaks of human aorta have been investigated by means of this technique [21]. CE are known to exist in a liquid-crystalline mesophase, meaning that they are typically more ordered than a liquid but still less than a crystal. Liquid crystals can be found in different mesophases, e.g., smectic phase and nematic phase. In the former molecules tend to point in the same direction while still having no positional order, whereas in the latter they also organize themselves in planes within which the motion is restricted. It is reported [21] that these fatty streaks are mainly composed of CE droplets organized in a smectic mesophase. X-ray diffraction is capable to distinguish between

the above mentioned structures and therefore to provide insights on the molecular arrangement of these CE droplets. It is interesting to notice that other traditional techniques, e.g. optical crystallography, are not able to provide this kind of information about the sample. In [21] and in a successive paper [22], Engelman et al. also pointed out two other characteristics of CE droplets. Firstly, they are highly birefringent; a thermotropic change in the birefringent pattern, as can be seen with a polarized light microscope, is often taken as a sign of a change of the sample physical state. Secondly, they exhibit a transition from the liquid-crystalline smectic mesophase to a less ordered structure when heated; the transition temperature T_{TR} between the two states is found to fall near the body temperature. Since T_{TR} depends on the chemical composition of the sample, a thermally controlled stage capable to record T_{TR} for different LD (e.g. LD in fatty streak lesions) is used to obtain information on the lipid molecules in the LD under investigation.

A second interesting class of methods for probing lipid ordering is based on *thermal analysis*. For example, thermal properties of CE mixtures have been studied by means of Differential Scanning Calorimetry [23]. If we consider mixtures of the two CE species cholesteryl palmitate and cholesteryl oleate, it is shown that below 49°C-50°C they form two immiscible crystalline phases, whereas above this temperature they form an isotropic liquid of eutectic composition, i.e. a liquid whose chemical composition allows it to solidifies at a lower temperature than that of any other liquid made up of the same components. From these results, we can already predict that the addition of CE droplets to a solution of TAG droplets makes the sample more ordered at room temperature, compared to a sample of pure TAG droplets. This complex behavior is highlighted in the section describing the results of our P-THG microscopy measurements of TAG, CE and TAG/CE solutions. The thermodynamic properties of samples comprising two constituents are often studied by the help of binary phase diagrams (e.g. [17], [23]), that show the phase of the sample for a given temperature and concentration of the constituents.

Especially during the '80s and '90s, *nuclear magnetic resonance* (NMR) has often been used to study the molecular organization of lipids in various solutions and in atherosclerotic plaques. For example, ^{13}C NMR spectra of human low-density lipoprotein have

been used to study the arrangement of cholesterol in this particle [24]. Moreover, structural information regarding mixtures of triglycerides and phospholipids have been investigated by means of ^{31}P , ^{13}C and ^1H NMR [25].

More recently, Horn et al. [26] developed a novel technique for direct organelle *mass spectrometry* (DOMS) in 2010. They applied this technique to the study of the TAG composition of LDs from different plant sources. DOMS was proved to be useful in:

- identifying the lipid composition of LDs by using the spectra of the masses of the LD constituents.
- quantifying the prevalence of TAG molecules.
- providing insights on the heterogeneity in composition of the LDs under investigation.

In general, non-optical techniques have proved to be useful in studying the spatial ordering of atoms in a material (X-ray diffraction, NMR), its thermal properties (thermal analysis) and composition and quantity of a given constituent in the sample (DOMS). However, this information is available only at the expense of the integrity of the system, e.g. X-ray photons can ionize the atoms, heating changes the physical state of the material and mass spectrometry involves the manipulation and acceleration of single lipids through a nanospray. These techniques also do not make use of signals generated by the sample, which would be favorable over the detection of modulated external signals, e.g. modulated X-rays. In fact, information based on intrinsic processes in a material is always more trustful than the one obtained from the simple modulation of an external source of energy.

We now present the optical techniques suitable for microscopy studies of LDs, starting from the linear ones (one-photon absorption) and then describing the most important nonlinear (multi-photon) ones, i.e., two-photon excited fluorescence (TPEF), second-harmonic generation (SHG), third-harmonic generation (THG) and coherent anti stokes Raman scattering (CARS).

1.6 Optical techniques

Traditional optical microscopy techniques rely on (linear) one-photon absorption processes as contrast mechanism. Several of the most widely used traditional techniques include conventional light microscopy, phase contrast microscopy, differential interference contrast microscopy (DIC) and confocal microscopy. Let us first consider the setup of a typical confocal microscope, which is illustrated in Figure 1.5.

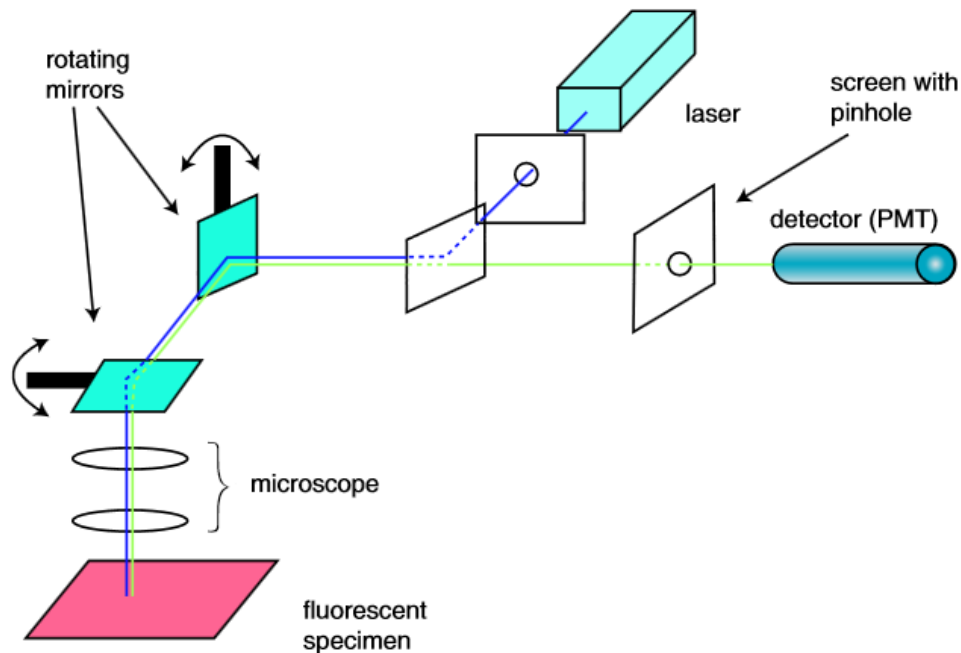


Figure 1.5: Basic setup of a typical confocal microscope that uses fluorescence to generate signal contrast. Light from the laser (blue) is scanned across the sample by means of the rotating mirrors. A dichroic mirror (i.e. the first mirror light encounters in the reflection pathway) directs the laser towards the specimen and let the fluorescent light (green) pass through it before reaching the detector. [27]

The confocal microscope was invented by Minski in 1955 [28]. It was meant to work either by collecting the light reflected off the specimen or by stimulating fluorescence from dyes attached to the specimen. Nowadays, a modern confocal microscope for biomedical applications works in the second way described. By looking at Figure 1.5, we notice that by

focusing the light on the specimen in a point-by-point fashion, most of the unwanted scattered light (that would obscure the image if the whole specimen were illuminated at the same time) is avoided. This fact represented a great advantage over standard light microscopes.

A second fundamental feature of a confocal microscope is the rejection of out-of-focus light. This is accomplished by using a pinhole along the way to the detector. A second pinhole, positioned in front of the light source, is also used to minimize how much of the specimen is illuminated and thus to increase the probability that the collected light comes from one single point within the sample. The combination of point-by-point illumination and rejection of out-of-focus light makes it possible to obtain higher resolution, i.e., discrimination of finer details, compared with conventional microscopes. Other characteristics of a confocal microscope are the choice of a laser source and its ability to achieve optical sectioning. The first one stems from the fact that, since imaging a point onto the specimen would result in a collection of very few photons, an intense monochromatic light source, i.e., a laser, is needed to get a signal strong enough for imaging. As far as optical sectioning is concerned, it is obtained by focusing the light at different depths and thus generating thin optical sections. From these optical sections an image reconstruction is possible, yielding a 3D visualization of the specimen.

The resolution of a confocal microscope is intrinsically diffraction-limited. It depends on the laser wavelength λ and on the microscope objective NA (numerical aperture) according to the Rayleigh Criterion:

$$R = \frac{1.22\lambda}{2NA} \quad (1.1)$$

The best lateral resolution of a confocal microscope is typically 200 nm [28]. Of course it is possible to rule out higher orders of the diffraction pattern (i.e., reduce the Airy disc radius) by closing down the confocal pinhole's aperture to a reasonable extent; however, in this case less photons would reach the detector and thus the image would be darker.

Confocal microscopy has been successfully used to study 3D dynamics in living cells, although some issues have prompted the need for new techniques to be developed. In fact, the use of this traditional technique is limited to regions near the surface of the sample (maximum penetration depths less than 100 μm) because, at higher depths, light scattering blurs the image. Moreover, optical sectioning is achieved only if a detection pinhole is used to filter out light not originated in the focal plane. In addition, the use of fluorescent dyes introduces the problem of the fluorophore influencing the cell behavior, often compromising the integrity of the system under investigation [29]. Dyes also suffer from photobleaching, meaning that they irreversibly fade when exposed to excitation light. Therefore, after a certain amount of time a fluorescent signal is no longer available to be measured. Several dyes have also phototoxic effects because, upon repeatedly exposure to high intensity laser illumination, they tend to react with molecular oxygen producing free radicals that can damage subcellular components. Photodamage is also caused by the focused high intensity excitation light, which is usually in the visible range of the spectrum.

Recently, advancements in MPM made it possible to overcome these limitations. In particular, SHG and THG have become elective techniques for the non-invasive imaging of biological specimens. In addition, they are often combined with other MPM techniques (multimodal imaging), such as TPEF, in order to provide more complete information about the microscopic environment in terms of chemical, structural and operative mechanisms characterizing the sample. CARS has also been used to image biological specimens, as it is able to provide vibrational contrast (e.g. [30] and [31]). All of these techniques are based on nonlinear light-matter interactions involving multiple photons to generate signal contrast. These nonlinear processes are induced at the focus of a high NA microscope objective.

In general, nonlinear optical processes are described by the branch of physics known as nonlinear optics (NLO), which focuses on the study of nonlinear optical phenomena that occur as a consequence of the interaction between a high intensity optical field provided by a laser and a material system.

Let us first consider the linear optical response of a material, in which the dipole moment per unit volume, i.e., the polarization $\tilde{\mathbf{P}}(t)$ ¹, is directly proportional to the electric field $\tilde{\mathbf{E}}(t)$:

$$\tilde{\mathbf{P}}(t) = Nq\mathbf{d} \quad (1.2)$$

$$\tilde{\mathbf{P}}(t) = \varepsilon_0\chi^{(1)}\tilde{\mathbf{E}}(t) \quad (1.3)$$

N is number of dipoles per unit volume, q is the magnitude of two opposite charges, \mathbf{d} is their distance and the proportionality constant $\chi^{(1)}$ is called linear susceptibility. Equation (1.3) tells us that, for a linear response, the dipoles in the material will oscillate at the same frequency of the applied electric field. The nuclei can be usually considered stationary because the electron is lighter than the proton by a factor of nearly 2000 (Born-Oppenheimer approximation): within this approximation, we can apply a model in which the electrons are held by springlike forces to the fixed nuclei. In this case, the oscillations are produced by the electrons that, in turn, will act as a source of radiation in accordance to the Larmor's theorem of electromagnetism². From the Maxwell's equations it is possible to derive the wave equation in a nonlinear optical medium, which has the following form:

$$\nabla^2\tilde{\mathbf{E}}(t) - \frac{n^2}{c^2}\frac{\partial^2\tilde{\mathbf{E}}(t)}{\partial t^2} = \frac{1}{\varepsilon_0c^2}\frac{\partial^2\tilde{\mathbf{P}}(t)}{\partial t^2} \quad (1.4)$$

where n is the refractive index and c the speed of light. The term on the right hand side of equation (1.4) is the source term arisen from the nonlinear optical response of the material. This equations shows that an oscillating polarization (accelerated charges) leads to the

¹ The symbol \sim defines quantities that vary rapidly in time.

² The Larmor's theorem states that accelerated charges generate electromagnetic radiation.

generation of an oscillating electric field, that is, of a new electromagnetic wave. This new wave has the same frequency as that of the time-varying polarization.

If the applied optical field $\tilde{\mathbf{E}}(t)$ is sufficiently strong, e.g., $\tilde{E}(t) \cong 5.14 \times 10^{14} \frac{V}{m}$ (characteristic atomic field strength), we express the resultant polarization by a power series because the higher order terms are no longer negligible:

$$\tilde{\mathbf{P}}(t) = \varepsilon_0[\chi^{(1)}\tilde{\mathbf{E}}(t) + \chi^{(2)}\tilde{\mathbf{E}}^2(t) + \chi^{(3)}\tilde{\mathbf{E}}^3(t) + \dots] = \tilde{\mathbf{P}}^1(t) + \tilde{\mathbf{P}}^2(t) + \tilde{\mathbf{P}}^3(t) + \dots \quad (1.5)$$

The quantity $\chi^{(n)}$ represents the material n th-order susceptibility. Mathematically, $\chi^{(1)}$ is a second order rank tensor, $\chi^{(2)}$ is a third order rank tensor and so forth. From equation (1.5) a nonlinear material may be defined as any optical medium for which at least one coefficient (other than $\chi^{(1)}$) of this expansion is nonzero. Nonlinear optical phenomena such as SHG and THG result from the contributions of the second and third order terms of this power series, respectively.

Given this theoretical background common to all nonlinear optical processes, the interaction between the incoming photons and the sample is different for each technique in MPM, as illustrated schematically in Figure 1.6.

In TPEF, a molecule reaches an excited state by the energy combination of two photons typically in the infrared (IR) region. This two-photon absorption process was first shown theoretically by the German theoretical physicist Maria Goeppert-Mayer (Nobel Prize for Physics in 1965) in the early '30s. At this point, the molecule proceeds along the normal fluorescence-emission pathway. TPEF is thus a nonparametric process, because the initial and final quantum state of the system are different as the two-photon absorption occurs. Conversely, SHG, THG and CARS are parametric processes, in the sense that they are energy-conserving processes; in fact, they involve only virtual states (very short-lived states that are not eigenfunctions of the molecule). They are also coherent processes, e.g., the radiated

photons show the same directionality as the incoming ones, whereas TPEF is isotropically emitted.

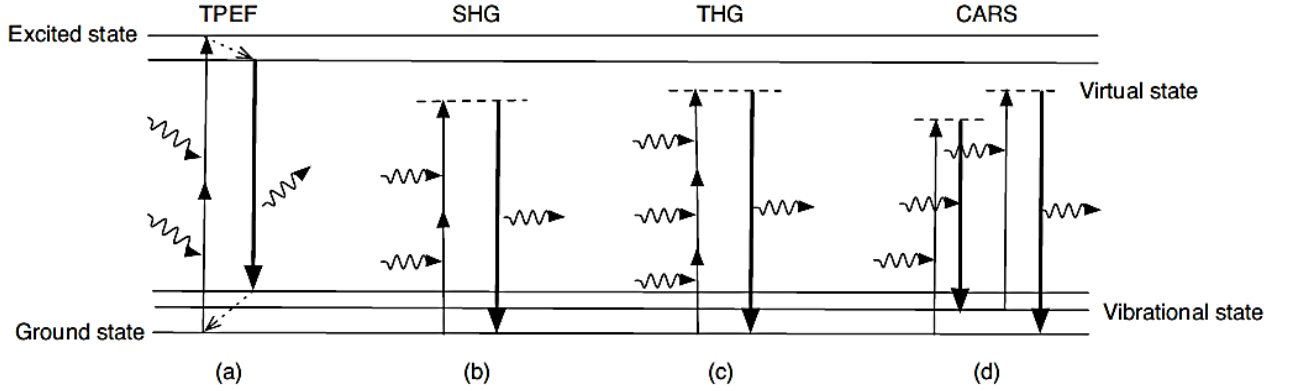


Figure 1.6: Jablonski diagrams for (a) TPEF (b) SHG (c) THG (d) CARS. Except for TPEF, the other processes do not involve an electronic excitation and thus they are parametric processes. [32]

TPEF has been used, for example, to study molecular orientations of the lipid bilayer in cells using different polarized excitations [33].

With regard to SHG processes, if we express the electric field as:

$$\tilde{E}(t) = E(\omega)e^{-i\omega t} + E^*(\omega)e^{i\omega t} = E(\omega)e^{-i\omega t} + c.c. \quad (1.6)$$

The nonlinear polarization caused by the incident light is given by:

$$\tilde{P}^{(2)}(t) = \varepsilon_0 \chi^{(2)} \tilde{E}^2(t) = \varepsilon_0 \chi^{(2)} [E^2 e^{-i2\omega t} + (E^*)^2 e^{i2\omega t} + 2EE^*] \quad (1.7)$$

The explicit frequency dependence ($E = E(\omega)$) has been omitted for simplicity. Equation (1.7) may be decomposed into three frequency components:

$$P(2\omega) = \varepsilon_0 \chi^{(2)} E^2$$

$$P(-2\omega) = \varepsilon_0 \chi^{(2)} (E^*)^2 = P^*(2\omega) \quad (1.8)$$

$$P(0) = 2\varepsilon_0 \chi^{(2)} E E^*$$

The first term corresponds to dipole oscillations at frequency 2ω , which is double the frequency of the incident light. This polarization oscillating at 2ω generates electromagnetic radiation at this same frequency. The second term is the complex conjugate of the first, which comes from the choice of a complex notation for the electric field. Finally, the last term represents a DC polarization component also called *optical rectification*. We notice that this component is predominant over the oscillating one due to additional factor of 2. The overall result of this nonlinear process is the presence of a radiation at frequency 2ω together with the stronger first-order field at the fundamental frequency ω . In other words, as depicted in Figure 6, two photons of frequency ω are destroyed and a photon of frequency 2ω is created.

SHG microscopy has become an elective technique for studying the structure of biological samples with a noncentrosymmetrical molecular organization, e.g., collagen [34], protein crystals [35] and, more interestingly, cholesterol crystals in atherosclerotic plaques [36]. Moreover, SHG polarization (P-SHG) anisotropy measurements can be used to determine orientation and degree of organization of molecules and for studying chiral samples [37] and, more generally, to reveal the material anisotropy. SHG microscopy is actively used to investigate molecular aggregates and cellular structures that form interfaces for which the two media have a different second-order susceptibilities.

THG is the simplest third order optical process, for which the nonlinear polarization is proportional to the third power of the electric field:

$$\tilde{P}^{(3)}(t) = \varepsilon_0 \chi^{(3)} \tilde{E}^3(t) \quad (1.9)$$

Expanding this expression leads to two distinct frequency components for the polarization:

$$\begin{aligned} P(3\omega) &= \varepsilon_0 \chi^{(3)} E^3 \\ P(-3\omega) &= \varepsilon_0 \chi^{(3)} (E^*)^3 \\ P(\omega) &= 3\varepsilon_0 \chi^{(3)} E^2 E^* \\ P(-\omega) &= 3\varepsilon_0 \chi^{(3)} E (E^*)^2 \end{aligned} \quad (1.10)$$

The first two terms correspond to third harmonic generation, whereas the last two are frequency components that oscillate at the same frequency as the input laser beam. The Jablonski diagram in Figure 1.6 shows that, in this process, three incident photons are annihilated and a three-times more energetic photons is created.

It is worth noting that both SHG and THG are coherent processes, meaning that they maintain the directionality of the incident field. Therefore SHG and THG signals are typically detected using a transmission configuration for the microscope. They are also parametric because only virtual levels are involved in the interaction with the molecule. Another important characteristic of harmonic generation is that these processes are enhanced near a resonance, although in this case a parasitic absorption occurs. THG has recently found a novel application in microscopy, allowing the imaging of molecular ordering in LD [38] and multilamellar lipid vesicles [39]. This technique, which was used in the present work, is fully explained in the next chapter.

Finally, CARS is a nonlinear four-wave mixing process (a third order process) recently applied to LD research [40]. If the frequency difference between the pump beam (arrow pointing upward) and the Stokes beam (arrow pointing downward) approaches the characteristic lowest vibrational frequency of the molecule, a CARS signal is generated, whose direction is given by the phase matching condition. This high intensity signal is actually in the Anti-Stokes region because $\omega_{cars} = 2\omega_{pump} - \omega_{stokes}$. Like SHG and THG, CARS does not involve any excitation of the molecule and therefore it can be considered a parametric process.

This microscopy technique is sensitive to molecular vibration states and can be used to detect the presence of specific chemical bond types. This fact provides a powerful tool for vibrational imaging of living cells in physiological conditions, without the need of dyes that would affect their metabolism.

TPEF, SHG and THG can be easily combined to provide multimodal imaging that allows one to highlight structures in unstained biological samples and have also information about biochemical functions and physiological conditions of the different organelles. This is achievable, for example, by using an optical parametric oscillator (OPO) where the pump laser is a Ti:S laser, so that appropriate wavelengths (typically 730-900 nm for 2PEF and 1050-1250 nm for SHG and THG) are obtained for the different multiphoton techniques.

We can now consider the general characteristics shared by these MPM techniques, as well as their advantages over conventional (linear) optical microscopy.

We first notice that the use of IR wavelengths provides deeper penetration in biological specimens (up to few hundred microns in highly scattering specimens) and therefore these methods are well suited for studying thick tissue samples. This is the case because IR wavelengths minimize scattering in tissues ,i.e., Rayleigh scattering has a dependence on the wavelength λ of the type λ^{-4} . IR light is also generally less phototoxic because IR photons are not sufficiently energetic to generate significant endogenous absorption in most tissues. Since MPM techniques require intensities in the TW/cm^2 regime to achieve a high quantum

efficiency, IR photons are favorable over visible ones because the latter would be photodestructive to the sample at these intensities.

In addition, nonlinear signals are induced in a femtoliter focal volume and the excitation is thus highly 3D localized. This is the case because nonlinear optical processes only occur if a high intensity light is used (i.e., their quantum efficiency is very low); to achieve this goal, tight focusing is required, along with the use of a pulsed laser that further increases the probability that two photons will simultaneously interact with the molecule. For a TPEF process, the two photon cross-section σ_{2p} [$\text{cm}^4 \text{ s}$] can be used as a quantitative measure of the probability for a two-photon absorption to occur [41]. Figure 1.7 schematically shows how the nonlinear excitation differs from the linear one.

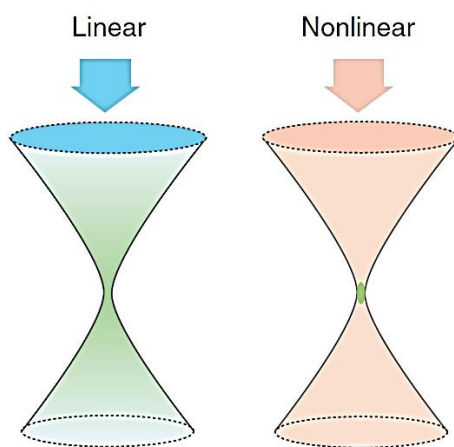


Figure 1.7: In conventional microscopy (left-hand side), visible light, e.g., blue light, is used; the one-photon emission shows fluorescence at the waist but also in a cone-like region below and above the focal volume. Conversely, in MPM (right-hand side) the excitation is given by IR pulsed lasers, which spatially confine the signal generation to the vicinity of the focal spot. [42]

We clearly see that in MPM the interactions between the photons and the sample are confined to the focal plane of the objective because in that region the beam intensity is maximum and therefore the probability of triggering a nonlinear process is highest. This fact can also be explained by considering that the signal depends nonlinearly (second power for SHG and TPEF and third power for THG and CARS) on the input intensity. As a result of the

localized excitation, in MPM there are no out-of-focus contributions (no need for a confocal pinhole) and this results in an intrinsic three-dimensional resolution, i.e., inherent optical sectioning capabilities. The localized excitation also implies less photodamage to the sample. Apart from TPEF, the other nonlinear processes described above generate signal contrast by exploiting intrinsic nonlinear optical properties of the material. Two important consequences come from this fact: first, no labeling with exogenous molecular probes, e.g., dyes, is required, and second, it is possible to image the specimen over hours without a decrease in signal intensity.

The axial (focal depth) and lateral (focal diameter) resolutions of a MPM technique are quantified by a three-dimensional Point Spread Function (PSF), whose analytical expression can be calculated based on the paper by E. Wolf [43]. The PSF basically depends on the size of the interaction volume, which in turn varies with the order of nonlinearity; for example, it is shown [44] that for an N -th order nonlinear process the interaction volume decreases by a factor \sqrt{N} compared to the linear interaction, if the wavelength stays the same. The effective PSF depends of many complex factors, such as the wavelength, the objective NA and the optical configuration of the detection. Given that the confocal pinhole is not infinitely small, the achievable spatial resolutions of a confocal microscope and MPM are similar, although the resolution of the latter is often far superior in scattering samples [45]. In literature (e.g. [44]) the lateral and axial resolution of an ultrashort pulse microscope are often expressed as:

$$\text{Lateral resolution: } r_0 = \frac{0.61\lambda}{NA} \quad (1.11)$$

$$\text{Axial resolution: } z_0 = \frac{2n\lambda}{(NA)^2} \quad (1.12)$$

Focusing our attention on coherent nonlinear optical processes (SHG, THG and CARS), we now consider a typical MPM setup, which is schematically illustrated in Figure 1.8. The most common laser source for multiphoton imaging is Ti:sapphire due to its average power

capability (up to several watts), broad tuning range (700-1100 nm) and thus short pulse duration (less than 10 fs). Before reaching the XY scanner (usually made of two mirrors), the laser is expanded with a telescope and spatially filtered with a pinhole located at the focus between the two telescope's lenses. Furthermore, after the XY scanner the beam passes through an achromatic lens and a tube lens to match the back aperture of the excitation objective: matched filling of the back aperture leads to a diffraction-limited focus and resolution, whereas underfilling of the back aperture leads to an axially extended focus and lower resolution. On the detection side of the microscope, a dichroic mirror is placed after the collection objective/condenser for separation of SHG and THG signals. Once these signals are collected on a pixel-by-pixel basis, the image is constructed via software and shown on the screen. An epi-detection is also possible, although the signals are much weaker in this direction due to the coherence property of the nonlinear processes. Of course, for *in vivo* applications, only an epi-collection mode is used.

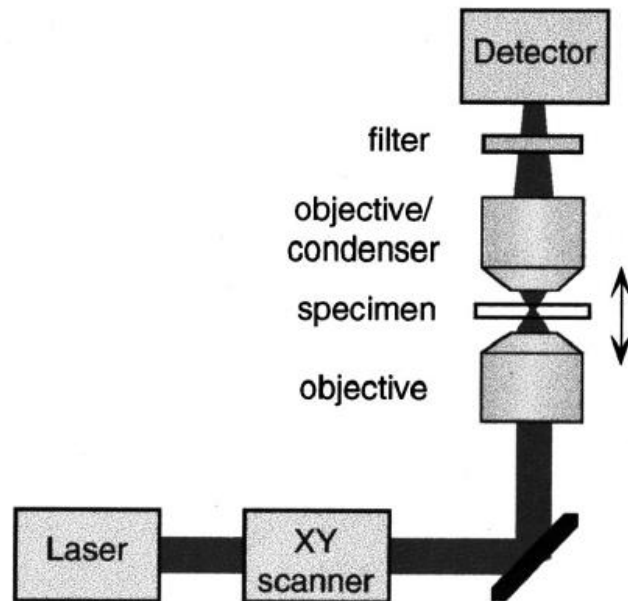


Figure 1.8: Simplified setup of a typical nonlinear optics microscope for coherent processes. A femtosecond laser is focused by high NA microscope objective onto the specimen. The scanning along the Z-direction is usually performed by translation of the specimen, whereas the XY scanner is used for the lateral direction. The signal is detected in the forward direction typically with a photomultiplier tube, after passing through a filter that blocks the fundamental frequency. [44]

Chapter 1: *Overview*

We notice that a NLO setup needs only slight modifications to a conventional confocal microscope, i.e., optics adapted for IR region, a pulsed laser, the incorporation of wave plates and polarizers.

In conclusion, in this chapter we have showed that lipid ordering is critically important in the study of biological tissues affected by lipid-related disorders. We have also remark the usefulness of both non-optical and optical techniques in investigating lipid assemblies.

The next chapter presents THG microscopy in more detail and highlights its most important applications in the biomedical field.

Chapter 2

THG microscopy

2.1 Principles in imaging

In 1992 [46], benefiting from solutions already known from the '60s, a complete theory explaining harmonic generation using focused Gaussian beams was developed. In particular, we notice that the solution of the paraxial wave equation for the amplitude of third harmonic is given by:

$$A_3(z) = \frac{i3\omega}{2nc} \chi^{(3)} A_1^3 J_3(\Delta k, z_0, z) \quad (2.1)$$

where:

$$J_3(\Delta k, z_0, z) = \int_{z_0}^z \frac{e^{i\Delta k z'} dz'}{\left(1 + \frac{2iz'}{b}\right)^2} \quad (2.2)$$

A_1 is the amplitude of the fundamental field, $\Delta k = 3k_\omega - k_{3\omega}$ is the phase mismatch, z_0 is the value of z at the entrance of the nonlinear medium and b is the focal depth of the focus lens (i.e., the confocal parameter). If we consider an homogeneous bulk medium for which $b \ll |z_0|, |z|$, the limits of the integral in (2.2) can be replaced by minus and plus infinite leading to:

$$J_3(\Delta k, z_0, z) = \begin{cases} 0 & \Delta k \leq 0 \\ \frac{\pi b^2 \Delta k}{2} e^{-b\Delta k/2} & \Delta k > 0 \end{cases} \quad (2.3)$$

We clearly see that no THG is expected for a normally dispersive ($\Delta k < 0$) medium. This result can be understood considering the so called Gouy phase shift of π rad experienced by

any beam of light near its focus; this phase shift leads to destructive interference between the wave before and after the focus. Therefore the only way to compensate for this effect is to introduce a positive phase mismatch Δk . However, in the case of inhomogeneities, such as material interfaces, the limits of the integral are finite and a THG signal is generated. Specifically, THG is radiated from the bulk of the media on both sides of the interface.

What has been just described is the theoretical background that represents the basis for THG microscopy sensitivity. Starting from the mid-'90s and thanks to the continuous improvement of laser sources, experimental studies have been carried out that confirmed what predicted by theory and, moreover, discovered new intriguingly features of THG microscopy.

The first study about the contrast mechanisms underlying this technique is reported by Tsang et al. in 1995 [47]. In this work, it is experimentally shown that THG production is allowed if an interface is present within the focal volume of the excitation beam. If this is the case, no phase mismatch is required and THG is efficiently triggered for $\Delta k = 0$.

This fundamental experimental finding about THG sensitivity lead to a rapidly expanding field of imaging studies based on THG contrast mechanisms. Probably the first work on THG microscopy is that conducted by Barad et al. in 1997 [48]. What they did was probing non-biological transparent samples using a tightly focused laser beam (125 fs pulse duration, 80 MHz repetition rate, 380 mW average power and 1500 nm wavelength) and detecting the THG signal from these structures. They basically considered three samples: a thin film of index-matching oil between two glass plates, a single glass plate and glass fibers mounted between two glass plates and immersed in index-matching fluid. For all of these cases they found a strong THG signal at the interfaces, i.e., oil/glass interface and air/glass interface, as depicted in Figure 2.1.

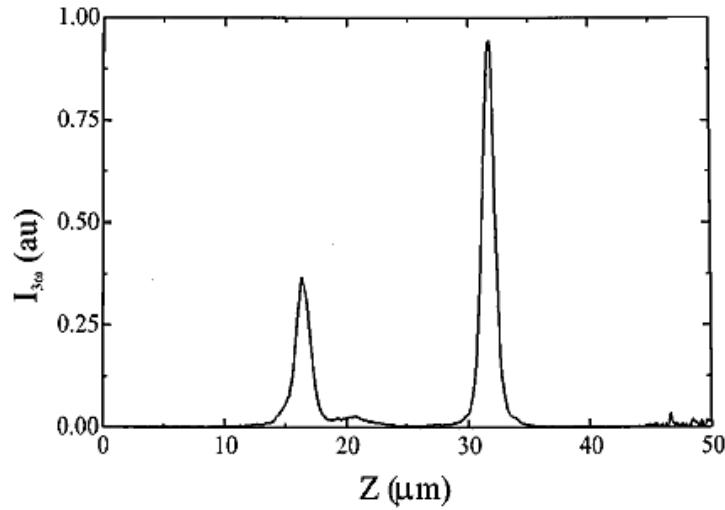


Figure 2.1: THG intensity versus axial position for a thin film of index-matching oil between two glass plates. The two peaks correspond to the crossing of the glass/oil interfaces crossing the focal point. This result shows the high THG sensitivity for discontinuities/inhomogeneities in a sample. [48]

They also obtained 2D images of the samples for a selected axial position. From these results we highlight the capability of THG microscopy to generate 2D distributions of the third order susceptibility in transparent samples. It is interesting to notice that even though in samples where the linear index of refraction is matched for the two media at an interface, a different value of $\chi^{(3)}$ gives rise to a large THG signal. We can thus say that this imaging technique is able to detect inhomogeneities in the nonlinear optical properties of the material. This fact is related to the interface detection capability of THG microscopy.

The abovementioned study restricted its attention to non-biological samples. In 1998 a paper by Squier et al. [49] proved THG microscopy as a viable technique for imaging living systems. They first examined conversion efficiency, power scaling and optical sectioning capabilities of THG under tight focusing conditions (laser: 100 fs pulse duration, 250 KHz repetition rate, 18 mW average power and 1200 nm wavelength). Then they checked the dependency of the THG signal on the interface orientation within the focal volume with respect to the excitation beam's direction of propagation, another contrast mechanism typical of third harmonic. Finally they managed to obtain dynamical and volumetric images (9s for

each sectioned image series with 1 μ m axial step) of Chara plants cells. The presented work demonstrated that THG microscopy is also suitable for biological samples, which are not damaged due to the continue exposure to the laser beam. Moreover, the imaging process can last over hours without loss of signal intensity and there is no need of labeling the samples with fluorescent dyes before starting the measurements. We can consider the work by Squier et al. as the starting point for all the successive applications of THG microscopy to bioimaging.

Further studies showed the dependancy of the third harmonic wave on the polarization of the incident field. For example, it is shown [50] that, for circularly polarized light, THG is not allowed in a isotropic medium, regardless of its composition (homogeneous/inhomogeneous). Mathematically, the $\chi^{(3)}$ tensor for an isotropic medium reduces to 21 nonzero elements, of which only 3 are independent. $\chi^{(3)}$ can be expressed as [51]:

$$\chi_{ijkl}^{(3)} = \chi_0(\delta_{ij}\delta_{kl} + \delta_{ik}\delta_{jl} + \delta_{il}\delta_{jk}) \quad (2.4)$$

The third harmonic nonlinear polarization is given by:

$$\mathbf{P}^{(3\omega)} = \chi_0 \begin{bmatrix} E_x(E_x^2 + E_y^2 + E_z^2) \\ E_y(E_x^2 + E_y^2 + E_z^2) \\ E_z(E_x^2 + E_y^2 + E_z^2) \end{bmatrix} \quad (2.5)$$

Where $\mathbf{E} = (E_x, E_y, E_z)$ is the incident electric field. For circularly polarized light we have $E_y = E_x e^{i\pi/2} = iE_x$; therefore $\mathbf{P}^{(3\omega)}$ identically vanishes for the case considered.

This fact implies that a THG signal is expected to be zero when isotropic areas of the samples are illuminated using circular polarization. Therefore, the crystalline (i.e., ordered) or amorphous (i.e., disordered) structure of materials can be probed by means of this technique,

often called circular P-THG (polarized THG). Circular P-THG is efficiently used to detect anisotropies and inhomogeneities within a sample, whereas linear P-THG highlights the interfaces. To account for effects such as Fresnel losses at the surface and scattering, an anisotropy parameter β which is sensitive only to the degree of disordering can be defined as [50]:

$$\beta = \frac{I_{circular}(\omega)}{I_{linear}(\omega)} \quad (2.6)$$

Comparing this method to the use of SHG (which is sensitive to the degree of disordering since it is only allowed in noncentrosymmetric structures), circular P-THG seems more robust to fluctuations due to the abovementioned effects, as shown in Figure 2.2.

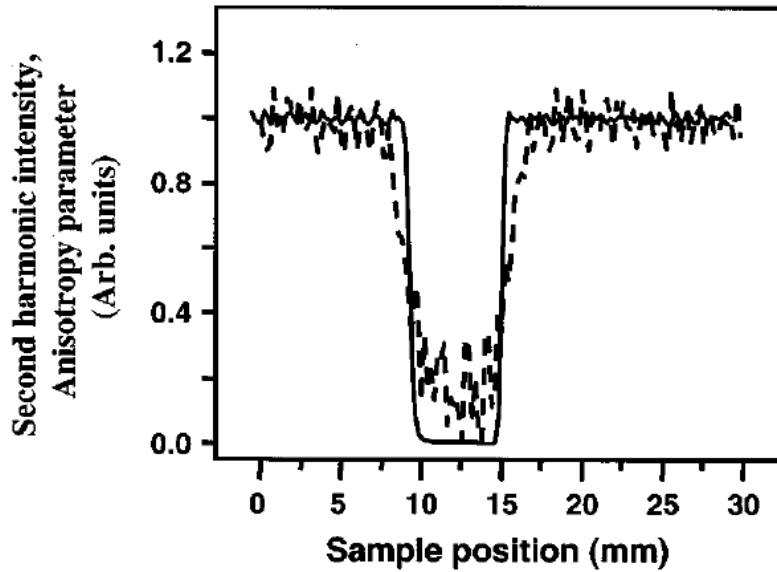


Figure 2.2: SHG and the anisotropy parameter β as a function of sample (GaAs (001) crystal) position. The surface area between 10 mm to 15 mm has been irradiated with a short UV pulse leading to a disordered structure. SHG and β are normalized to their respective values in the nonirradiated area. As expected, both SHG and the anisotropy parameter decreases as the beam is scanned along the amorphous region, but the latter is clearly less sensitive to surface modulations. [50]

In 2003, Oron et al. [52], [53] reported microscopy studies using P-THG microscopy. In particular, a linear polarization was used to highlight interfaces between media with different $\chi^{(3)}$ in biological samples. These inhomogeneities are on the scale of the beam focus. In addition, they used circular P-THG to study the anisotropy of biogenic crystals, e.g. calcite, that are highly birefringent. In such crystals, positive phase-matching ($\Delta k > 0$) is achieved and therefore a THG signal can be detected. It is also possible to extract information about the crystal orientation from the polarization state of the THG signal [53]. In this second study, they demonstrated the ability of circular P-THG of selectively address anisotropic structures in a sample, ruling out completely the signal generated by an isotropic background. Conversely, linear polarization is capable to detect inhomogeneities within crystalline samples.

An example of P-THG images [52] is shown in Figure 2.3. The sample consists of single larval spicules (tiny spike-like structures) immersed in $n=1.61$ index-matching oil on a glass microscope slide.

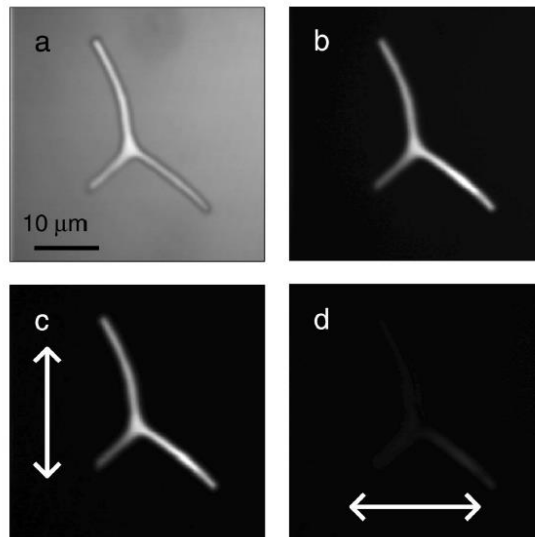


Figure 2.3: (a) Image obtained using linearly polarized light. We notice a strong background due to the glass-immersion-oil interface and a slightly higher signal from within the spicule (i.e. from calcite). (b) when circularly polarized light is shone on the sample, the image is background-free because circular P-THG is zero for an isotropic medium. (c) and (d) are the same as (b), but a polarizer allowing either vertical or horizontal polarization states is placed between the sample and the detector. (c) and (d) images indicate that the crystal orientation is maintained throughout the sample. [52]

Other factors such as beam focusing and object size influence the intensity of the THG signal. Let us consider the case of a beam focused at the center of a small (diameter $\sim\mu\text{m}$) spherical object immersed in a homogeneous solution. As the beam size increases, theoretical calculations show an increase in THG intensity [54], which reaches a maximum and then drops off after a certain value of the diameter. The position of the maximum depends of the focusing conditions, i.e., lower NA (higher focal volumes) lead to a left shift of the maximum, whereas higher NA (lower focal volumes, better axial resolution) give rise to a right shift. It is also noteworthy that the THG signal decreases when defocusing the excitation beam away from an interface. Only if the interface is surrounded by several small objects (as in the case of biological organelles), then the dependency of the THG signal on the focus position is reversed, i.e., it increases with increasing defocusing. This interesting phenomenon is due to the fact that defocusing implies a higher focal volume; therefore more objects are illuminated at the same time, generating a coherent summation of their radiated fields and thus a higher intensity. We notice that, in general, the THG signal is always the overall result of the contributions from the micrometer-scale objects within the excitation volume; therefore, the number and geometry of the scatterers and the property of the input beam play a fundamental role in generating this signal.

2.2 Application in LD imaging

Having delineated the most important characteristic of THG-microscopy, its application to biology and in particular to the imaging of LD is considered.

The first work reporting THG-microscopy studies of LD has been conducted by Débarre et al. in 2006 [55]. They basically proved LD to be a major source of contrast in THG-microscopy for a variety of biological samples, i.e., hepatocytes, liver tissue, *D. Melanogaster* embryos, plant seeds and fresh lung tissue. In order to correctly interpret the THG images, they first derived the nonlinear optical susceptibilities of several biological solutions, given that the intensity of a THG signal induced by a moderately focused laser beam

(NA < 0.8) at an interface between two media a and b is proportional to the following expression:

$$I_{THG} \cong (\alpha_a - \alpha_b)^2 \quad (2.7)$$

where:

$$\alpha = \frac{\chi^{(3)}}{n_{3\omega}(n_{3\omega} - n_{\omega})} \quad (2.8)$$

$n_{3\omega}$ and n_{ω} are the linear refractive indices at the third harmonic and excitation wavelength, respectively and $\Delta n = (n_{3\omega} - n_{\omega})$ is the refractive index dispersion between the two waves.

It is shown that, at $\lambda = 1180 \text{ nm}$:

$$\chi^{(3)}_{tryglicerides} = 2.58 \pm 0.5 \left[\times 10^{-22} \frac{m^2}{V^2} \right]$$

$$\chi^{(3)}_{oil} = 2.71 \pm 0.5 \left[\times 10^{-22} \frac{m^2}{V^2} \right]$$

whereas for water and ionic solutions:

$$\chi^{(3)}_{water} = 1.68 \pm 0.08 \left[\times 10^{-22} \frac{m^2}{V^2} \right]$$

$$\chi^{(3)}_{water+1M NaCl} = 1.79 \pm 0.09 \left[\times 10^{-22} \frac{m^2}{V^2} \right]$$

These values lead to the following THG intensities:

$$I_{THG} \cong (\alpha_{tryglicerides} - \alpha_{water})^2 = 479.61$$

$$I_{THG} \cong (\alpha_{oil} - \alpha_{water})^2 = 795.61$$

$$I_{THG} \cong (\alpha_{water+1M NaCl} - \alpha_{water})^2 = 4.41$$

$$I_{THG} \cong (\alpha_{water} - \alpha_{water})^2 = 0$$

Lipid solutions should thus give a high contrast in THG images. This was proved true in successive measurements on the samples cited above. In particular, the proof was given by the excellent correlation between THG and 2PEF images. The latter were taken by staining the samples with the hydrophobic fluorescent dye Nile Red, which has the interesting property of accumulating in LD. As reported in the paper, THG images can also be used to extract information about the size distribution of LDs in healthy or abnormal tissues; this provides a tool for assessing its physiological state and also the processes underlying certain diseases, such as atherosclerosis, which involves a deregulated fat metabolism.

Another interesting experiment concerns the epi-detection of the THG signal in a sample of microspheres embedded in agarose of adjustable scattering properties. This experiment is illustrated in Figure 2.4.

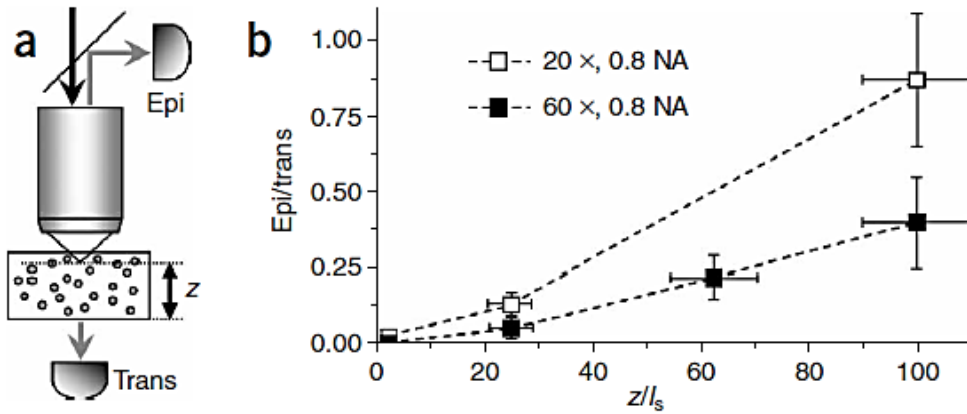


Figure 2.4: (a) Experimental setup, showing trans and epi-detection modalities. z represents the thickness of the sample below the focal plane (dotted line). (b) dependence of the ratio epi/trans THG signal on the number of scattering mean free paths. It is clear that the epi-detection is more efficient for highly scattering samples and for a lower-magnification (20 x) objective. [55]

This is particularly challenging since, as described in the previous chapter, THG is a coherent process and therefore most of the signal propagates in the forward direction, i.e. the direction of the excitation beam. Débarre et al. [55] demonstrated that an epi-detection of the THG signal is possible in weakly absorbing tissues because in this case bulk scattering can redirect a detectable amount of photons back to the surface; since the backscattered light is not originated by a point source but rather by an extended source within the tissue, a low magnification objective that provides a higher lateral field of view allows a better collection of the backscattered photons.

As the laser beam is focused farther from the surface (i.e., the coordinate z decreases), the efficiency of the epi-detection is lowered until no more THG photons are detected in the backward direction. More precisely, it showed that the signal approximately scales as $e^{-z/40 \mu m}$, where $z = 0$ corresponds to the sample's surface on the side of the excitation objective.

More recently, in 2010, a paper by Olivier et al. [51] showed the capability of THG microscopy to investigate, along with other MPM techniques such as TPEF, the microstructure of intact biological tissue for clinical usage. Specifically, the authors presented a microscopy

study of human corneas combining SHG and THG microscopy and confirmed that it is possible to extract information about anisotropies and inhomogeneties of the tissue under investigation; these data can then be used for assessing eye disorders like corneal dystrophy. It is known that the cornea consists of six layers: the epithelium (the outermost layer), the Bowman's layer, the stroma, the Descemet's membrane and the endothelium. The stroma is particularly interesting because it is composed of $\sim 2\mu\text{m}$ thick collagen lamellae of different orientations and sparsely distributed keratocytes.

In order to distinguish between different structures, they used SHG and P-THG (linearly and circularly polarizations) microscopies. By doing this, they found that, for a linearly polarized light, the lamellae (i.e. fibrillar collagen) give maximum SHG signal, whereas interfaces (cell/cell and nucleus/cytoplasm) are associated with a strong THG. If the polarization state of the incident beam is changed from linear to circular, then the THG signal stems from anisotropy changes between differently oriented lamellae in the stroma and the contributions of the (isotropic) cells is excluded. Moreover, it was noticed that, if we consider two successive lamellae in the xy plane (i.e, the plane perpendicular to the propagation direction of the incident beam), the polarization of the THG signal changes with respect to the axial position, that is, the output THG light is circularly polarized at the interface between two lamellae and it is elliptically polarized within each lamella. As if facts were not complex enough, the main axis of the ellipse varies between two perpendicular directions for each lamella.

Numerical simulations reported in this work confirmed that no THG signal is obtained when circularly polarized light is focused across an interface between isotropic media; conversely, this interface is detectable by using linear polarization. In the case of an interface between an isotropic and an anisotropic medium, such as the stroma, it is showed that the THG signal is nonzero. For example, if we consider a crystal with exagonal symmetry around the x axis, the THG signal approximately scales as $|\chi_{||} - \chi_{cr}|^2 + |\chi_{cr} - \chi_{\perp}|^2$, where $\chi_{||} = \chi_{xxxx}^{(3)}$, $\chi_{cr} = 3\chi_{xxyy}^{(3)}$ and $\chi_{\perp} = \chi_{yyyy}^{(3)}$ are the three independent tensorial components of $\chi^{(3)}$ for the crystal. The presented study [51] shows once again that P-THG microscopy is able to

map heterogeneities and anisotropies in biological samples, providing information about the organization and ordering of micrometer-scale structures.

The most recent work on P-THG microscopy of lipid assemblies has been conducted by Zimmerley et al. [56] in 2013. They performed microscopic studies on multilamellar lipid vesicles (MLVs) and on stratum corneum (i.e., the outermost layer of the human skin) samples. First, they developed a multiscale model for the third harmonic process generated by lipid assemblies and then they compared the results derived from numerical simulations with the obtained THG images.

At the atomic level, they introduced the hyperpolarizability tensor γ as the term of proportionality that relates the induced dipole moment $e\mathbf{r}_i^{(3)}$ to the incident electric field \mathbf{E} :

$$e\mathbf{r}_i^{(3)}(\omega_4) \sim \sum_{jkl} \gamma_{ijkl}(-\omega_4; \omega_3, \omega_2, \omega_1) \times E_j^{loc}(\omega_3) E_j^{loc}(\omega_2) E_j^{loc}(\omega_1) \quad (2.9)$$

where $\omega_4 = \omega_3 + \omega_2 + \omega_1$ (for THG $\omega_3 = \omega_2 = \omega_1$), e is the electronic charge, $E_j^{loc}(\omega_n)$ is the local electric field oscillating at frequency ω_n and $ijkl$ are any of the three Cartesian coordinates in the molecular frame. It is shown that, at the atomic level, the CC bonds are the source of the measured THG signal. This is the case because the hyperpolarizability associated with CC bonds is roughly six times higher than that of CH bonds [57]. Of course, at the molecular level, the THG signal is due to the summation over the contributions of all the dipoles within the molecule. Finally, if we consider the entire MLV, its nonlinear susceptibility $\chi^{(3)ML}$ depends on the orientations of each molecule composing the system and therefore $\chi^{(3)ML}$ is thought to be the average of the molecular hyperpolarizability (sum over the atomic hyperpolarizabilities). Zimmerly and colleagues were able to compute these nonlinear optical properties and thus to predict the intensity of the THG signal for different structural conditions of the sample, e.g, the level of disordering. Experimentally, given an ordered material, linear P-THG can be used to probe different $\chi^{(3)ML}$ tensor elements. In addition to this, they also numerically shown that the linear P-THG response from the lipid

bilayer is modulated when the incident polarization is varied from being perpendicular (maximum signal) to parallel to the surface (minimum signal). In particular, if Ω is the direction of the field relative to the polarization axis, the modulation in the transverse plane scales approximately as $\cos(\Omega)^2$ with an amplitude that depends on the NA of the excitation objective.

In their work it was also highlighted that the tight focusing of a laser beam leads to an electric field asymmetry at the focal volume. For example, given light linearly polarized along the x-direction, a distribution of electric field components also exists in the y and z directions, as shown in Figure 2.5.

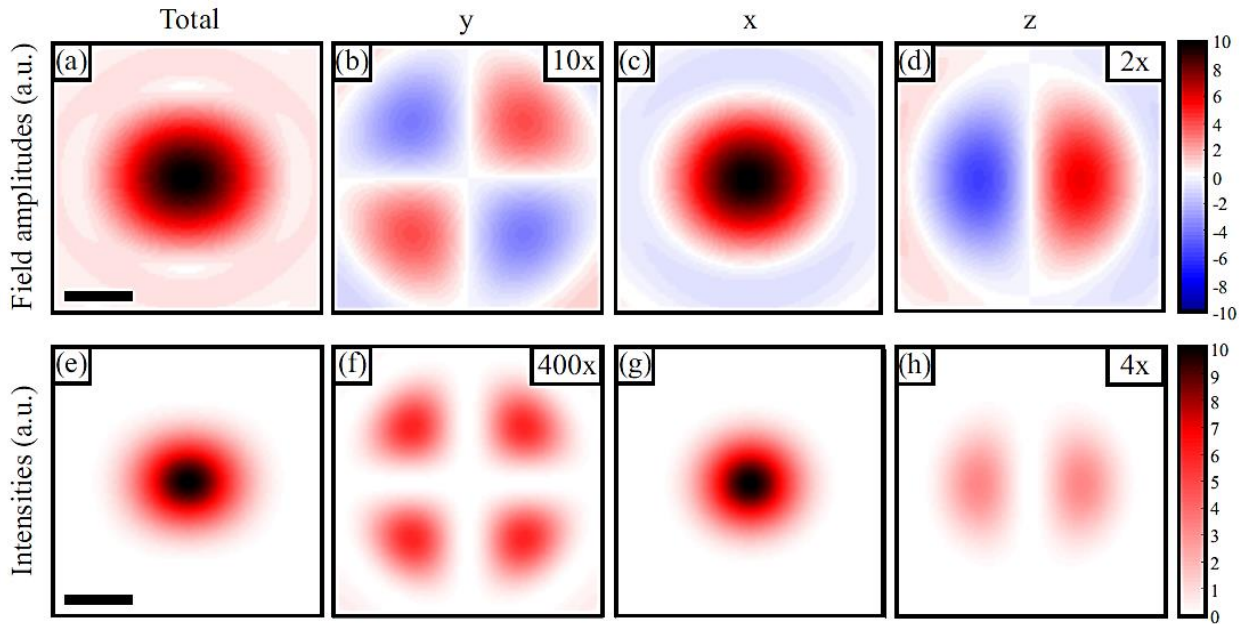


Figure 2.5: Numerical calculations showing normalized electric field and intensity distributions of a tightly focused (NA=0.8, filling factor=1) Gaussian beam at the focal plane $z=0$. The beam is linearly polarized along the x-direction (horizontal). It is clear that the \mathbf{E} components are nonzero for directions different from that of the incident polarization. Images (b), (d), (f) and (h) have been enlarged for clarity (black scale bar = one wavelength). [58]

In order to describe this phenomenon, a full vectorial description of the propagating electromagnetic beam is used instead of the simpler scalar approach. A new theory accounting

for the tight focusing of a Gaussian laser beam was already known in the '60 [43] and it was more recently further studied and applied to SHG microscopy [58]. We point out that the longitudinal field component becomes stronger for higher NA, thus increasing the level of asymmetry. This process occurring for tight focusing conditions casts doubt on the validity of linear P-THG images in providing information about sample anisotropy. In fact, as will be shown in the section dedicated on the result of our experiments, given two P-THG images taken with two linear polarizations perpendicular to one another, different structures of the samples light up and this event would be a sign of anisotropy. However, this same event could also be due to the electric field asymmetry at the focal volume; therefore we used circularly polarized excitation, which is highly favorable over linearly polarized light for anisotropy measurements because it does not suffer much from focus asymmetry.

Therefore, we expect linear P-THG to give the best results, i.e. highest contrast in the images, for TAG LDs, because these exhibit the most isotropic structures. Conversely, circular P-THG is expected to be more suitable for CE LDs, which are more anisotropic compared to previous ones. Of course, in the case of mixtures of the two types of LDs, a combination of linear and circular P-THG measurements provides useful information on the presence of both isotropic and anisotropic structures in the sample.

In this second chapter, we have provided an overview of the state of the art concerning THG microscopy studies of LDs, stressing the fact that this type of measurements have so far given the best results in mapping the degree of ordering of lipid molecules in LDs, as compared to non-optical and linear optical techniques.

The next chapter presents the materials and methods used for the experimental measurements.

Chapter 3

Materials and Methods

3.1 LD samples

In the present work P-THG images of TAG, CE and TAG:CE (in equal proportions) solutions have been taken. For each solution, samples are obtained by pipetting an appropriate volume of the chosen LD on a layer of agarose gel, which is in turn mounted on the top of a glass microscope slide.

The LDs are prepared by means of a chemical process involving the samples:

- PURE TAG (triacylglyceride)
- PURE CE (cholesteryl ester)
- CE:TAG (50% CE – 50% TAG)

These lipid samples are dissolved in 9:1 chloroform-methanol mixture. They are stored at -75°C for long term usage and at -20°C for frequently usage. The stock concentration is 100 mg/mL (this yields to a concentration of 112.93 mM for PURE TAG and 154.06 mM for PURE CE).

In order to get a LD concentration in sterile water of 100 mM (0.1 mol/dm^3) and a total LDs volume of 100 μL , we took 88.55 μL of a PURE TAG droplet, 64.90 μL of a PURE CE droplet and 32.45 μL CE, 44.27 μL TAG for CE:TAG. The chemical process is composed of the following steps:

- 1) Evaporation of the chloroform-methanol mixture by using nitrogen gas (inert gas, not reactive), so that the lipid droplets are isolated.
- 2) Storage of the lipid droplets in a high pressure vacuum chamber for 1-1.5h
- 3) Dissolution in sterile water such that the concentration of 100 mM is obtained.
- 4) Hydration in a water bath at 60°C: this step makes it possible to form the lipid droplets due to hydrophobic effect.

In general, the melting point of a lipid mostly depends on the structure of its attached fatty acids; in particular, higher chain lengths and carbon saturation lead to higher melting points [58]. Therefore, TAG droplets are liquid because they have a melting point much lower than room temperature, whereas TAG / CE solutions are solid at room temperature [17].

3.2 Sample preparation

The LDs described in the previous section have been used for preparing samples suitable for THG imaging. The procedure followed for the sample preparation is made of several simple steps. First, the LDs (TAG, CE or mixed solution), previously placed in a fridge at 3-5°C, were submerged in tap water heated at 60°C by a heating plate. The heating process is necessary to avoid the presence of clusters in the sample. Then, two rounded coverslips (12 mm diameter, 1.5 µm thick) were attached to a microscope slide (24x60 mm, 7.5 µm thick) by the help of ~ µL drops of epoxy. Also, agarose gel was obtained by mixing agarose powder with 10 mL of sterile water and by heating this mixture in the microwave (~ 100°C) for 1 min. After this time, the just formed agarose gel was put into the baker with tap water at 60°C; this step is critical because, if it is not readily accomplished, the agarose gel turns into a crystalline phase (solid) due to a lowering of the temperature and therefore it is no longer usable. The typical chemical structure of agarose is shown in Figure 3.1.

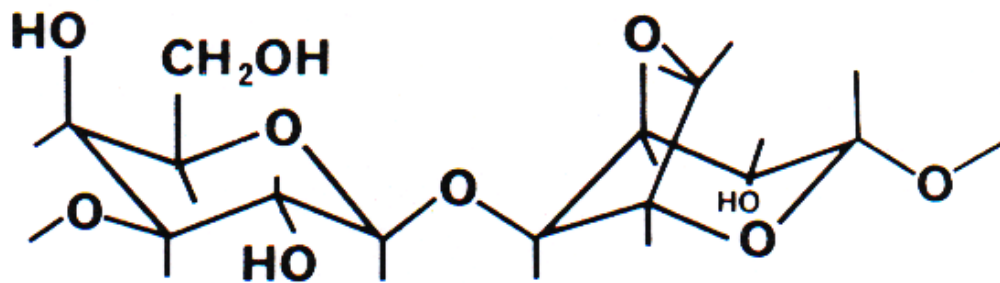


Figure 3.1: Basic chemical structure of agarose. Agarose is a polysaccharide composed of n repetitive units of a disaccharide, i.e. D-galactose (left-hand side) and 3,6-anhydro-L-galactopyranose (right-hand side). It is clear the typical linear arrangement of this polymer. [60]

Agarose is often used in many biomedical applications, e.g. electrophoresis, protein purification as well as a substrate for biomolecules in microscope slides, because of its physical, chemical and thermal stability and it does not interact with biomolecules.

The microscope slide equipped with the two coverslips was then put on the heating plate in order to maintain an appropriate temperature (at least 45°C) for the agarose and the LDs. 10 μ L of agarose gel was placed in between the coverslips, slightly upward, so as to allow a better positioning of the sample during imaging. The chosen LD was then taken out of the baker filled with water and stirred for a few seconds by means of a vortex mixer. This is done to avoid LDs clusters but instead to have sparsely distributed LDs throughout the sample. After this, 5 μ L of LDs were placed at the top of the agarose drop. A rounded coverslip (18 mm diameter, 1.5 μ m thick) was gently put on the mixture agarose/LDs, with the particular effort of slightly pushing it toward the bottom of the glass slide to avoid air bubbles in the sample. Finally, 200 μ L of agarose were used to surround the last mentioned coverslip in order to attach it firmly to the glass slide.

3.3 THG microscopy setup

In our experiments, a custom-built THG microscope was used. Figure 3.2 depicts a schematic of the THG microscope setup. The microscope was configured in transmission mode. The laser source was a mode-locked femtosecond Nd:glass laser (GLX-100; Time-Bandwidth Products) with the following characteristics: wavelength 1060 nm, pulse length 200 fs and repetition rate 82 MHz. The beam first passes through a linear polarizer (LP), so that from this point its polarization state is known. Then it is spatially filtered, collimated and expanded by the combination of two lenses (L) and a pinhole (P). The laser polarization is controlled by using motorized half- and quarter-wave plates (HWP and QWP, respectively). After the polarization optics, the beam is directed to an infinity-corrected and strain-free microscopy objective (EO) with NA = 0.8, which focuses the light onto the sample. The sample (S) is mounted on a 3-axis piezo scanner (Thorlabs); coarse tuning of the 3D position of the sample is performed by using knobs, whereas fine tuning is performed via LabView. The signal is then collected by a condenser with NA=0.5; this condenser is equipped with infrared blocking and interference (353 nm; Semrock) filters. The last part of the setup is represented by a cooled photomultiplier tube (PMC-100; Becker & Hickl GmbH), which detects the third harmonic signal. In addition, a transmission bright field imaging arm was used to view and select a region of interest in the sample. The bright field configuration is obtained adopting a LED light source, a tube lens and a CMOS camera. The average input power level was 40 mW for the all imaging experiments. Axial and lateral resolutions of the microscope are 2.4 μm and 0.8 μm , respectively.

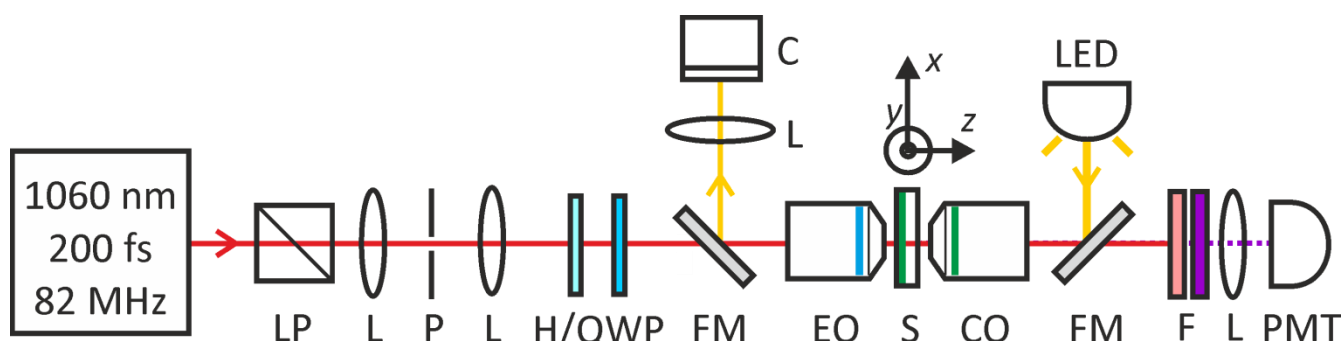


Figure 3.2: THG microscope setup. LP = linear polarizer; L = lens; P=pinhole; H/QWP = half/quarter-wave plate; FM = flip mirror; C = CMOS camera; EO = excitation objective; S = sample; CO = collection objective; F = filter; PMT = photomultiplier tube.

Chapter 3: *Materials and Methods*

The THG signals were collected per pixel (100 ms) or sample position. Subsequently, image analysis was performed using MATLAB and/or ImageJ.

This chapter presented the procedures followed for the sample preparation and the microscopy setup. The next one focuses on the results of our experimental measurements.

Chapter 4

Experimental THG imaging of various lipid samples and discussion

4.1 Polarized THG imaging of LDs

In this chapter we first present P-THG images of TAG, CE and mixed solutions of LDs. We then move on to CD-THG (circular dichroism THG) images, which are computed by combining the THG values obtained when using left and right circular polarizations.

4.1.1 TAG-enriched lipid droplets

In the following, THG images of the TAG-enriched LDs obtained using the NLO microscopy setup are presented. We focused on two sites of the sample, called site 1 and site 2. For site 2, the set of images is taken at different depths (coordinate z), providing 3D resolution and insights on the 3D structure of the TAG sample. The depth z is computed from the bottom of the microscope glass slide

Site 1

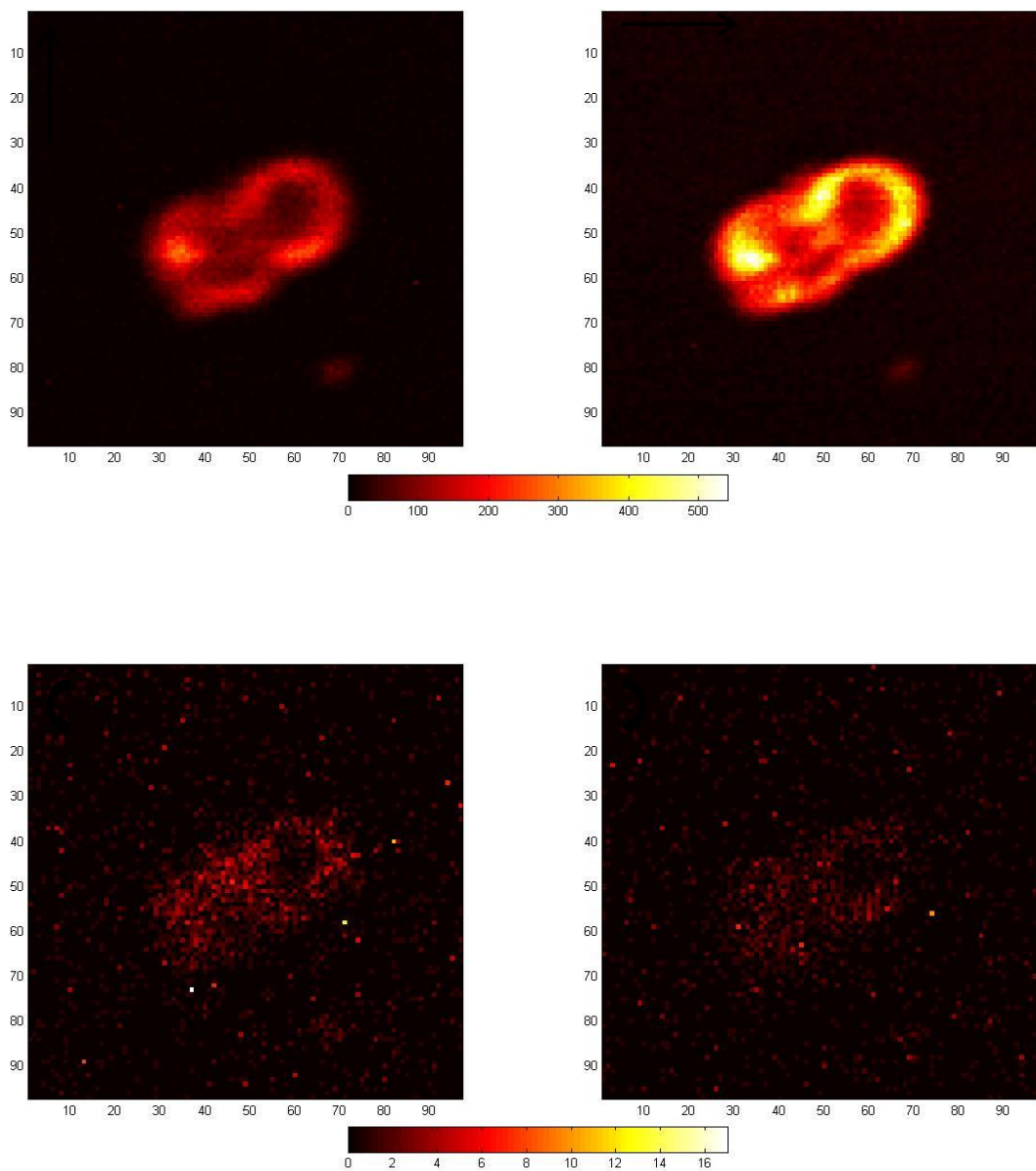


Figure 4.1: Top figure: TAG image (site 1) taken with two linear polarizations perpendicular to one another. Bottom figure: TAG image taken with left and right circular polarization.

Site 2 (3D, $z = 10 \mu\text{m}$)

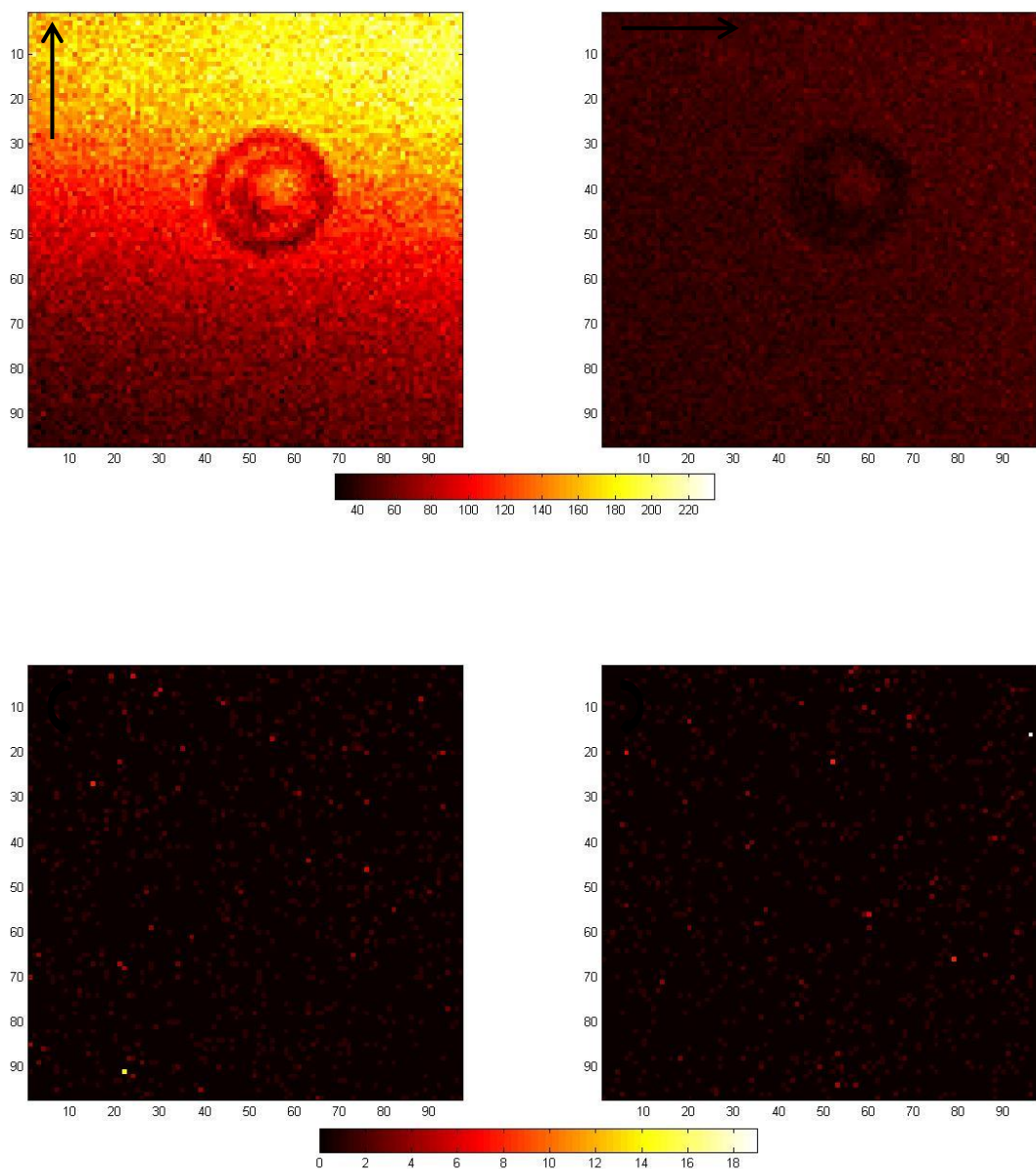


Figure 4.2: Top figure: TAG image (site 2) taken with two linear polarizations perpendicular to one another. Bottom figure: TAG image taken with left and right circular polarization. $z = 10 \mu\text{m}$.

Site 2 (3D, $z = 12 \mu\text{m}$)

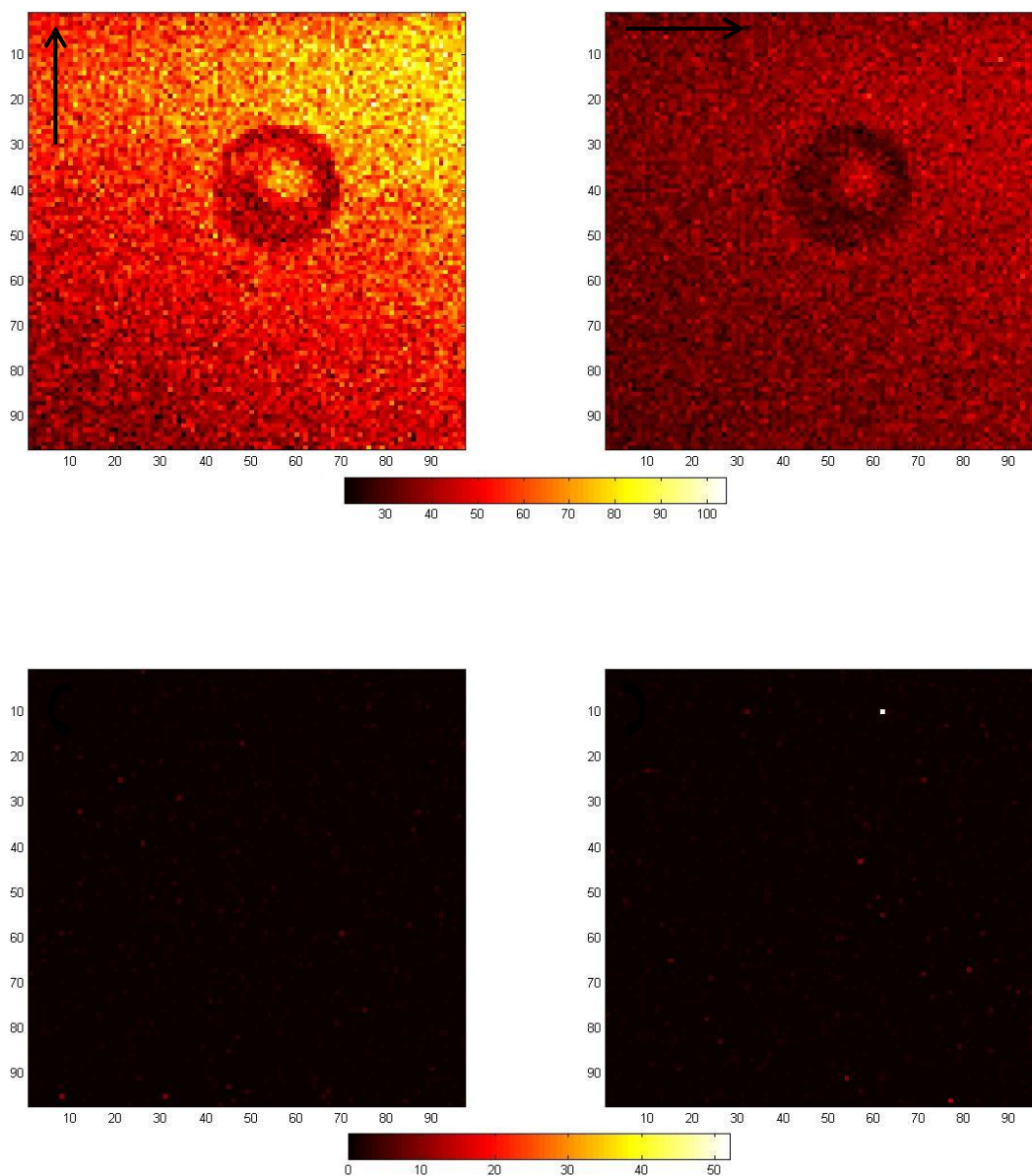


Figure 4.3: Top figure: TAG image (site 2) taken with two linear polarizations perpendicular to one another. Bottom figure: TAG image taken with left and right circular polarization. $z = 12 \mu\text{m}$.

Site 2 (3D, $z = 14 \mu\text{m}$)

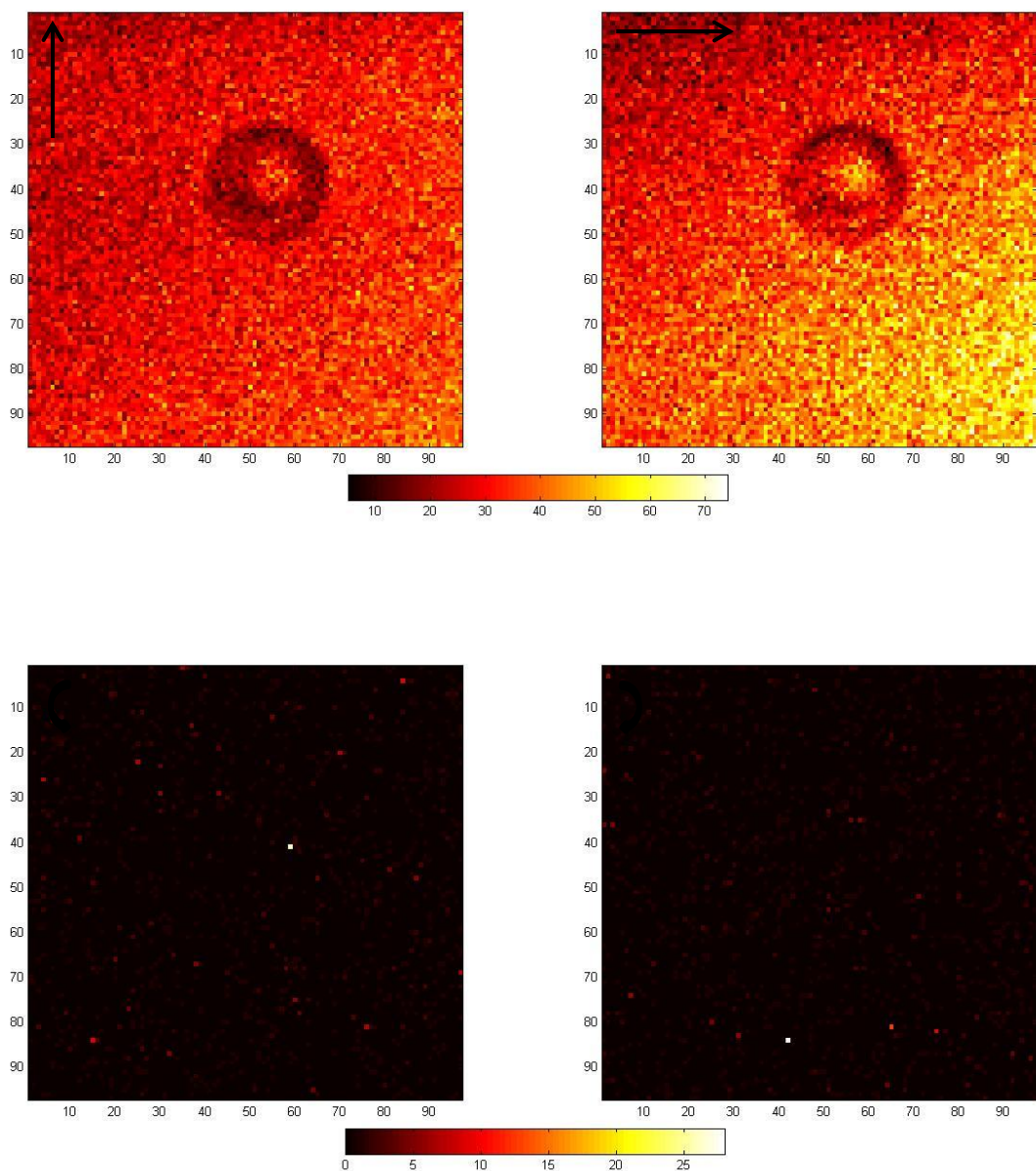


Figure 4.4: Top figure: TAG image (site 2) taken with two linear polarizations perpendicular to one another. Bottom figure: TAG image taken with left and right circular polarization. $z = 14 \mu\text{m}$.

Chapter 4: *Experimental THG imaging of various lipid samples and discussion*

Linear polarization highlights interfaces and inhomogeneity within the sample as earlier explained. In this case, TAG LDs emerge over the background due to a difference in the $\chi^{(3)}$ of the two materials. The strong background signal is due to the glass/agarose interface. Specific areas of the lipid droplets (i.e. site 1 and 2) light up, specifically the boundary of the droplet with the surrounding medium, as expected from theory. The level of signals varies with respect to the direction of the linear polarization. It is higher in the vertical direction than in the horizontal one for the case of site 2, $z = 10 \mu\text{m}$ and $z = 12 \mu\text{m}$, whereas linear polarization oscillating in the horizontal direction yields the highest values for site 1 and site 2, $z = 14 \mu\text{m}$. In the images taken with linear polarization, we also observe a truncated doughnut, which is due to the depolarization effect. The notable differences between these images are caused by the focus asymmetry issue as previously discussed; therefore, focused linear polarizations are not reliable for anisotropy measurements

We notice that the signal level for the linear P-THG images is always higher than that obtained with circular polarization; the maximum difference is found for site 1 and is roughly 400 counts. The average counts for circular P-THG images is close to zero, which is around the laser noise level. Therefore these images are almost totally blank. This fact is a proof that these samples are highly isotropic. We still notice the presence of a very small signal in the circular P-THG images, but this is expected when a laser beam is focused at an interface between a birefringent medium (the background) and an isotropic one [52].

4.1.2 CE-enriched lipid droplets

In this section we present the P-THG images of CE LDs.

Site 1 (3D, $z = 8.4 \mu\text{m}$)

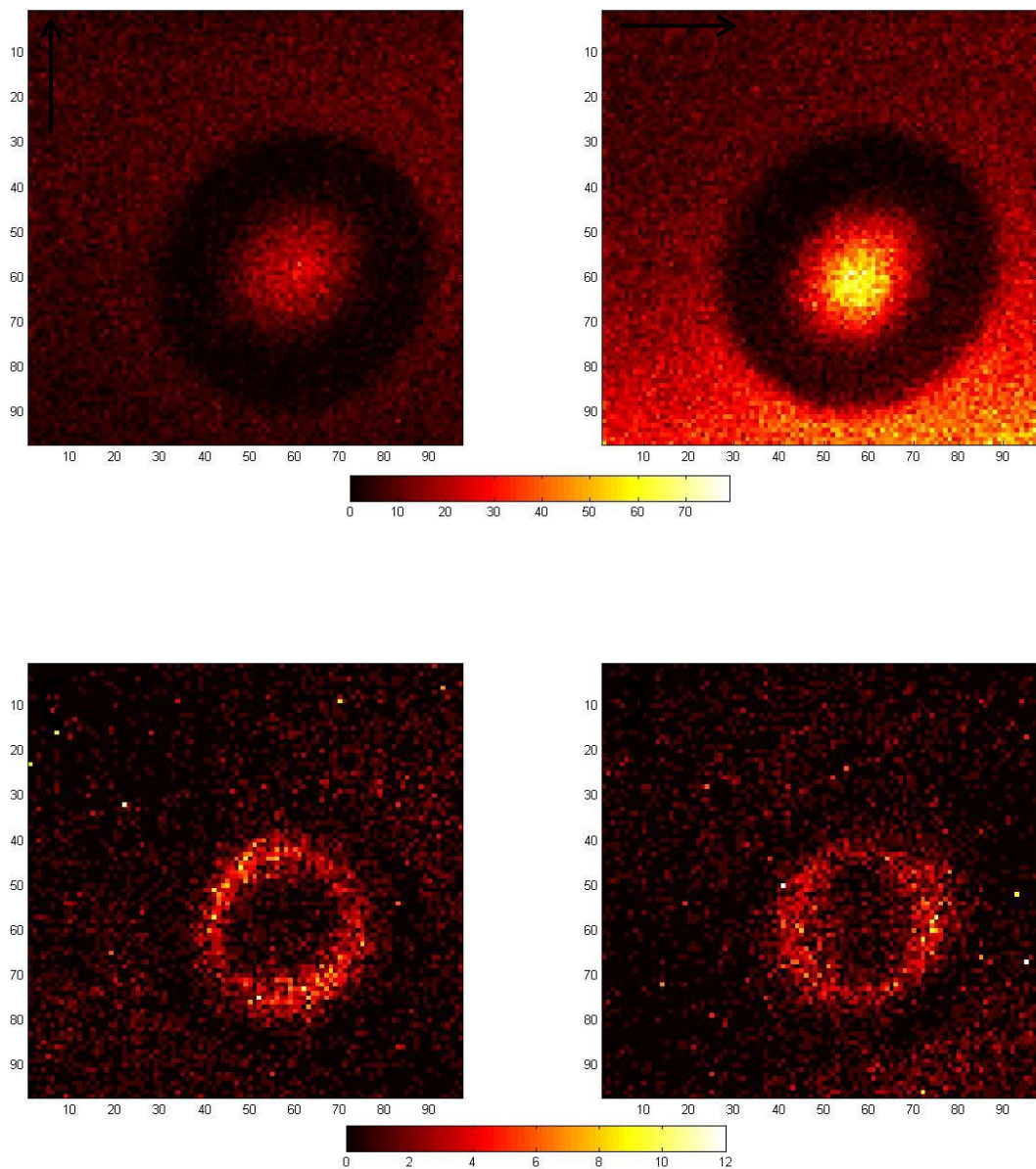


Figure 4.5: Top figure: CE image (site 1) taken with two linear polarizations perpendicular to one another. Bottom figure: CE image taken with left and right circular polarization. $z = 8.4 \mu\text{m}$.

Site 1 (3D, $z = 10.4 \mu\text{m}$)

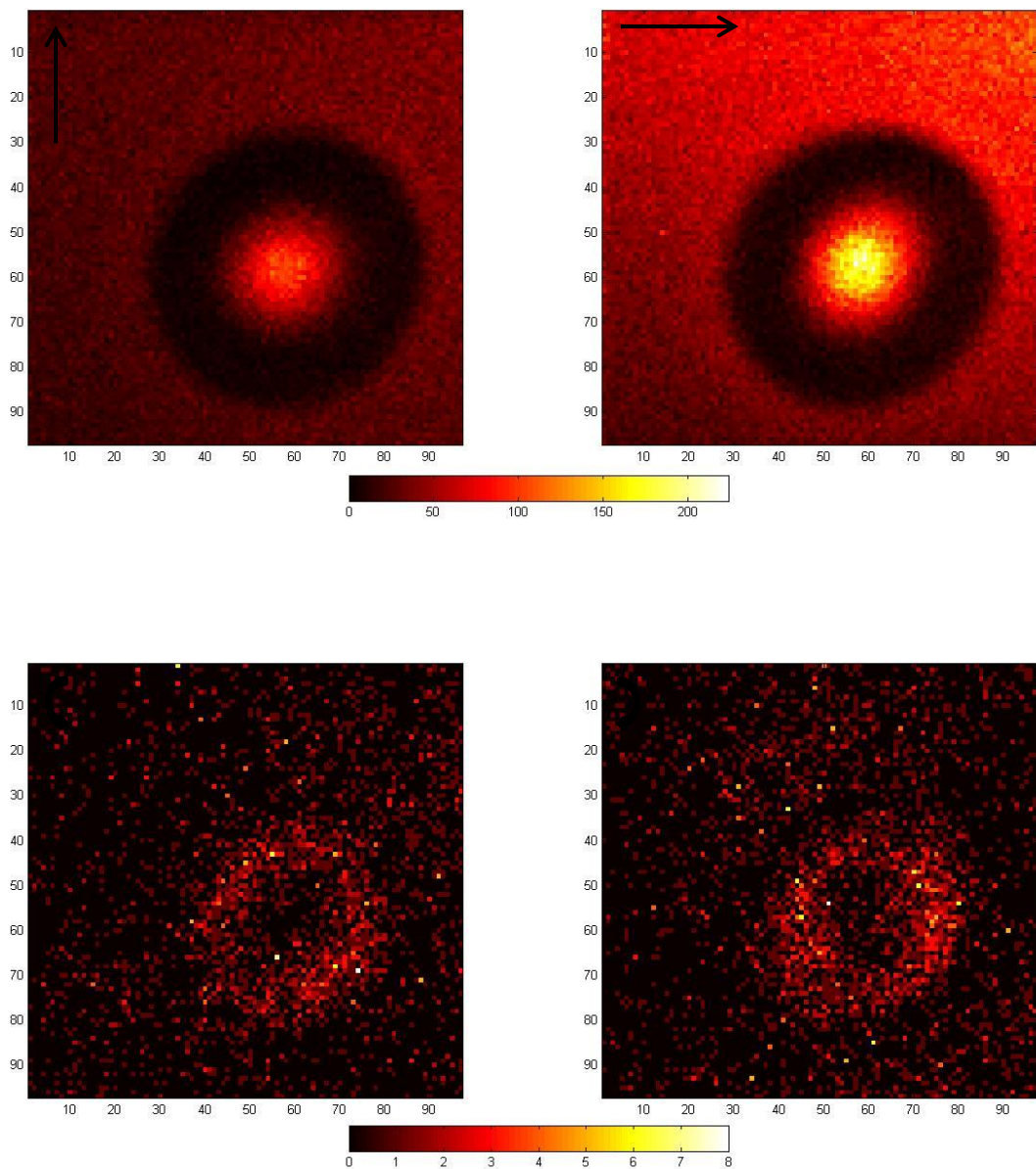


Figure 4.6: Top figure: CE image (site 1) taken with two linear polarizations perpendicular to one another. Bottom figure: CE image taken with left and right circular polarization. $z = 10.4 \mu\text{m}$.

Site 1 (3D, $z = 12.4 \mu\text{m}$)

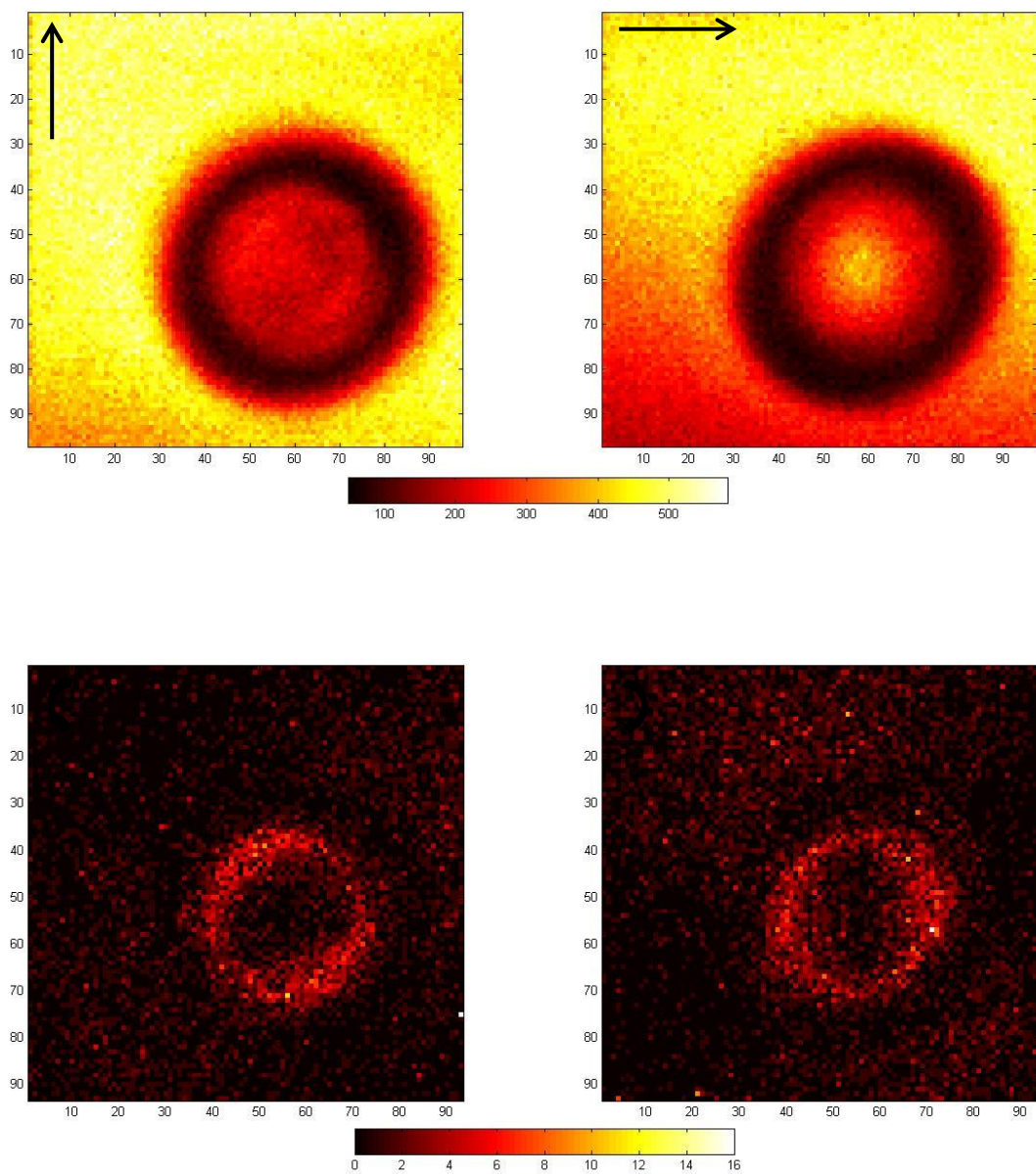


Figure 4.7: Top figure: CE image (site 1) taken with two linear polarizations perpendicular to one another. Bottom figure: CE image taken with left and right circular polarization. $z = 12.4 \mu\text{m}$.

Site 2 (3D, $z = 10 \mu\text{m}$)

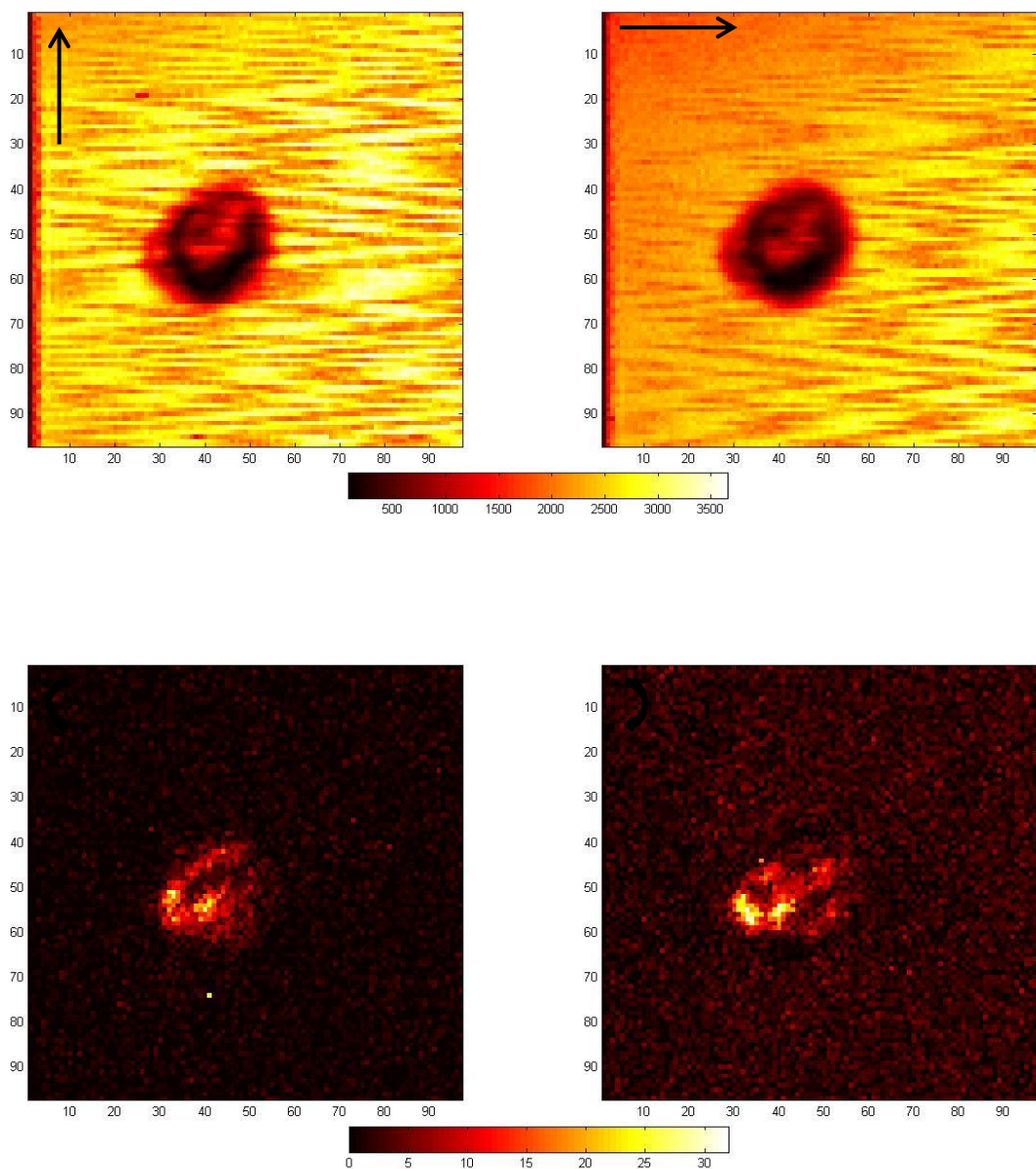


Figure 4.8: Top figure: CE image (site 2) taken with two linear polarizations perpendicular to one another. Bottom figure: CE image taken with left and right circular polarization. $z = 10 \mu\text{m}$.

Site 2 (3D, $z = 12 \mu\text{m}$)

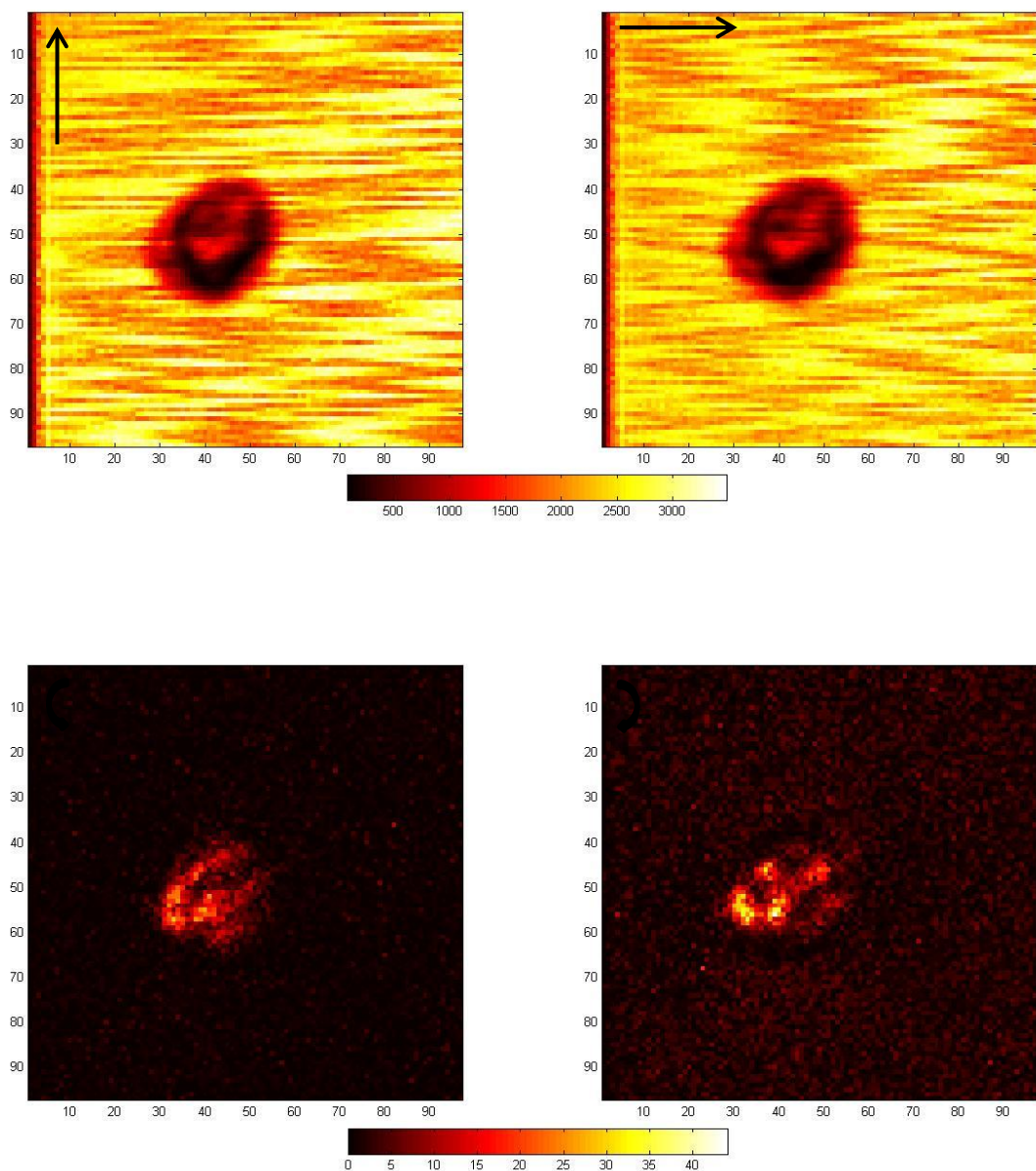


Figure 4.9: Top figure: CE image (site 2) taken with two linear polarizations perpendicular to one another. Bottom figure: CE image taken with left and right circular polarization. $z = 12 \mu\text{m}$.

Site 2 (3D, $z = 14 \mu\text{m}$)

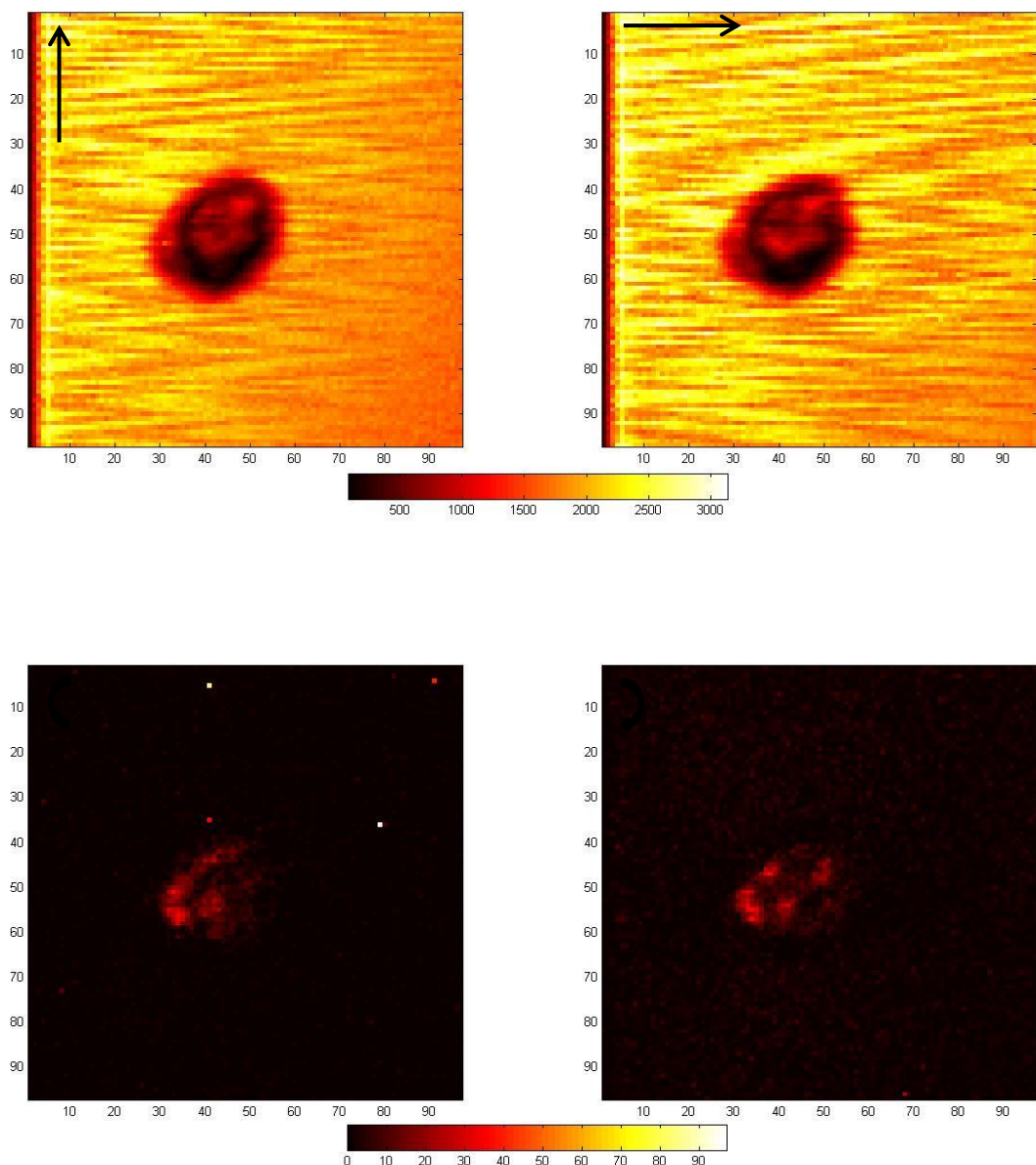


Figure 4.10: Top figure: CE image (site 2) taken with two linear polarizations perpendicular to one another. Bottom figure: CE image taken with left and right circular polarization. $z = 14 \mu\text{m}$.

Site 2 (3D, $z = 16 \mu\text{m}$)

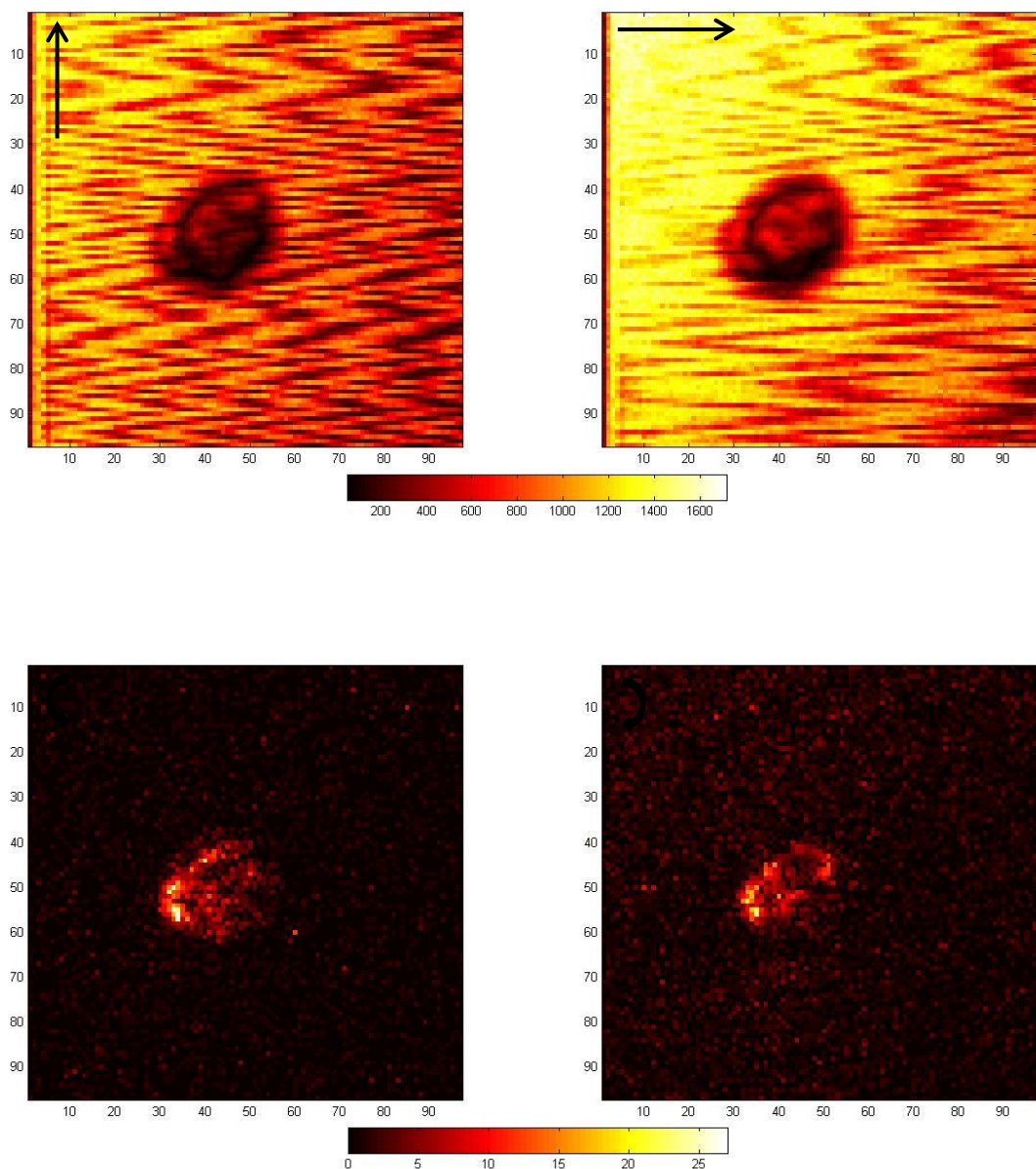


Figure 4.11: Top figure: CE image (site 2) taken with two linear polarizations perpendicular to one another. Bottom figure: CE image taken with left and right circular polarization. $z = 16 \mu\text{m}$.

Chapter 4: *Experimental THG imaging of various lipid samples and discussion*

With regard to the linear P-THG images, we notice differences between the results obtained for two orthogonal directions; as for TAG images, this fact can be attributed to focus asymmetry. In this case, we can attribute the intense signal to anisotropic domains within the LD. This result is in accordance with earlier findings, i.e. CE-rich inclusions may possibly exhibit different levels of ordering [61].

The level of the signals is always higher in the case of linear P-THG compared with circular P-THG. It is interesting to point out that, as the focus is moved away from the substrate, the background signal increases and it soon becomes higher than that coming from the interface between the droplet and the substrate.

Circularly polarized light efficiently maps the anisotropic regions of the sample. In the case of site 1, these regions seem to be mostly the boundaries of the droplet, whereas site 2 exhibits anisotropy within the core as well. We remind that CE LDs can exhibit different degree of ordering, which is usually dependent on the region of interest in the sample. At the moment, we do not know the full symmetry of the structures for careful characterization but our results suggest that anisotropic domains indeed exist in such samples.

The level of the signals for left and right circular P-THG are comparable. These signals, for site 2, are roughly at the same level than those from the TAG samples (both sites), although peaks of ~ 90 counts are reached for site 2 as opposed to a maximum of ~ 50 counts for the TAG sample. Site 1 of the CE sample shows instead less intense signals in comparison with those of the TAG sample.

4.1.3 Mixed TAG and CE-enriched lipid droplets

We now present P-THG images of TAG/CE LDs.

Site 1 (3D, $z = 8.5 \mu\text{m}$)

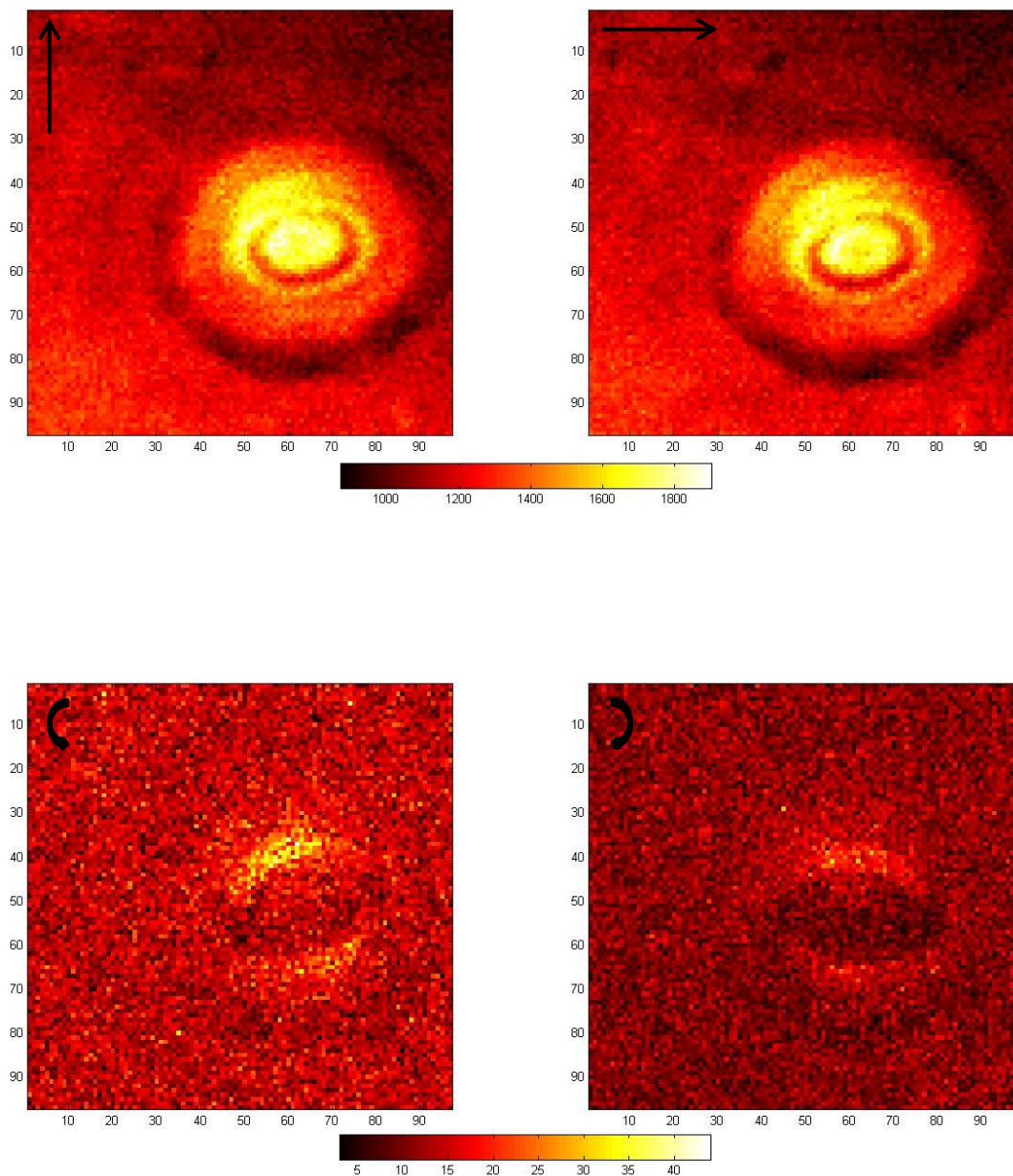


Figure 4.12: Top figure: TAG/CE image (site 1) taken with two linear polarizations perpendicular to one another. Bottom figure: TAG/CE image taken with left and right circular polarization. $z = 8.5 \mu\text{m}$.

Site 1 (3D, $z = 10 \mu\text{m}$)

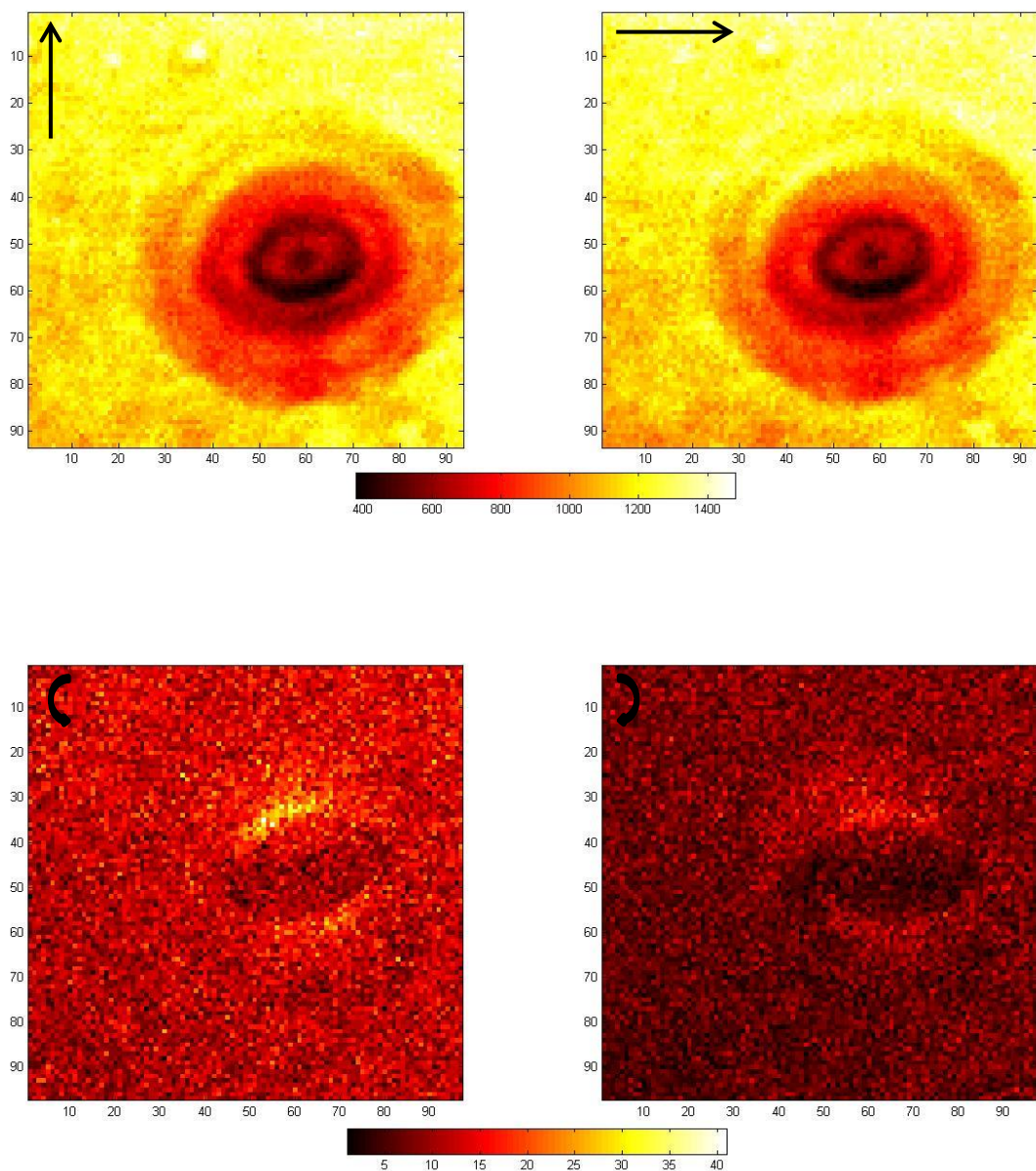


Figure 4.13: Top figure: TAG/CE image (site 1) taken with two linear polarizations perpendicular to one another. Bottom figure: TAG/CE image taken with left and right circular polarization. $z = 10 \mu\text{m}$.

Site 1 (3D, $z = 11.5 \mu\text{m}$)

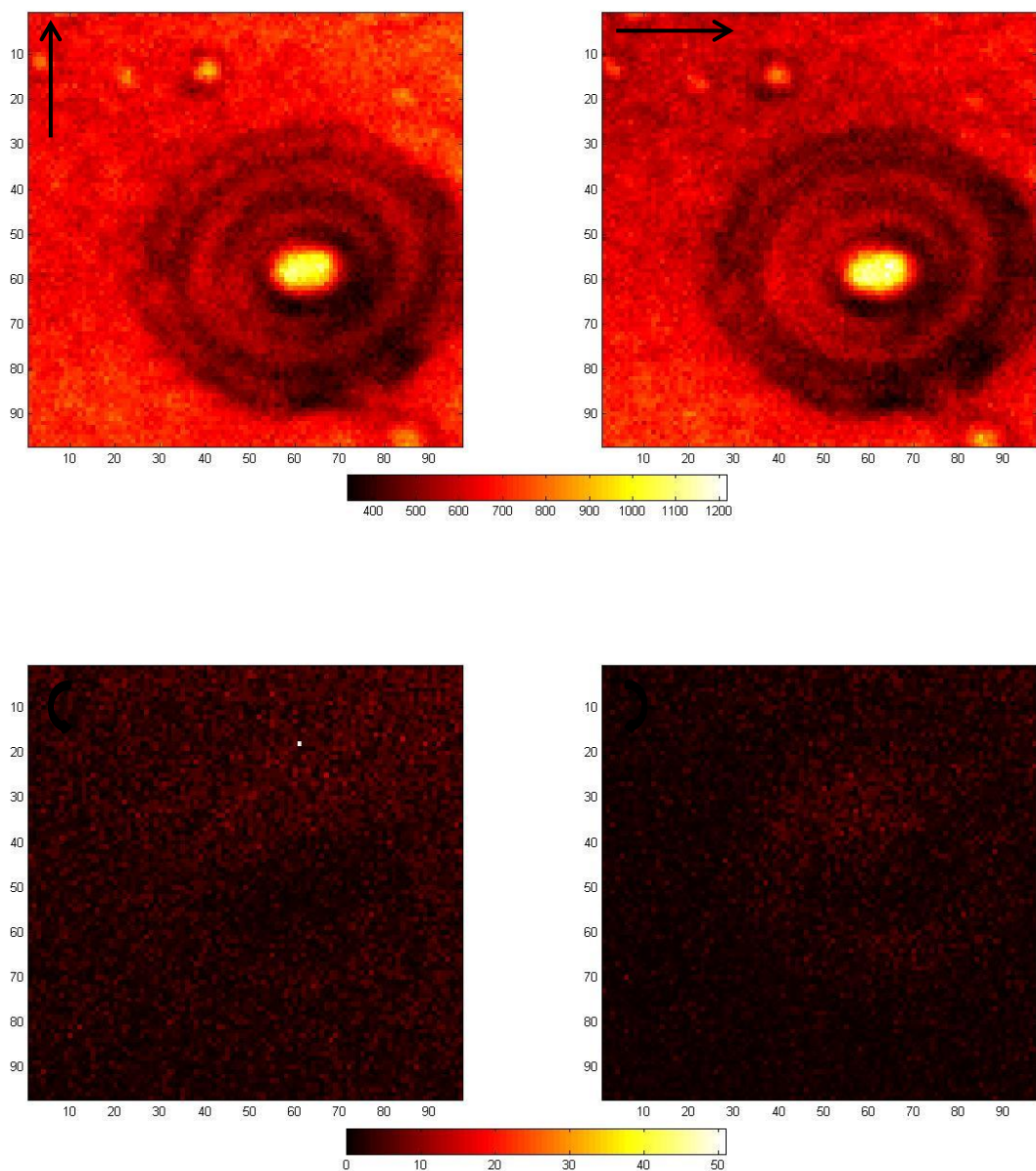


Figure 4.14: Top figure: TAG/CE image (site 1) taken with two linear polarizations perpendicular to one another. Bottom figure: TAG/CE image taken with left and right circular polarization. $z = 11.5 \mu\text{m}$.

Chapter 4: *Experimental THG imaging of various lipid samples and discussion*

From the linear P-THG images concerning site 1, we notice the presence of one large droplet surrounded by smaller ones. Linear polarization allows for the discrimination of all these droplets from the background, but it does not provide information about the level of ordering of these structures. As always, linear P-THG images are associated with higher counts compared with circular P-THG images. If we examine the latter, it is clear that the small droplets are no longer visible. This fact may mean that these domains are mostly isotropic, i.e. they are composed of TAG LDs. Conversely, the large droplet is still distinguishable from the background when using circular polarization, therefore it has to be associated with CE LDs, which might contain strongly anisotropic domains. In fact, as described in Chapter 1, these LDs introduce a degree of ordering in the sample [23], meaning that they make it more anisotropic. Also in this case, we highlight that this degree of ordering may vary with respect to the region under investigation for lipid samples containing CE LDs.

Site 2 (3D, $z = 10 \mu\text{m}$)

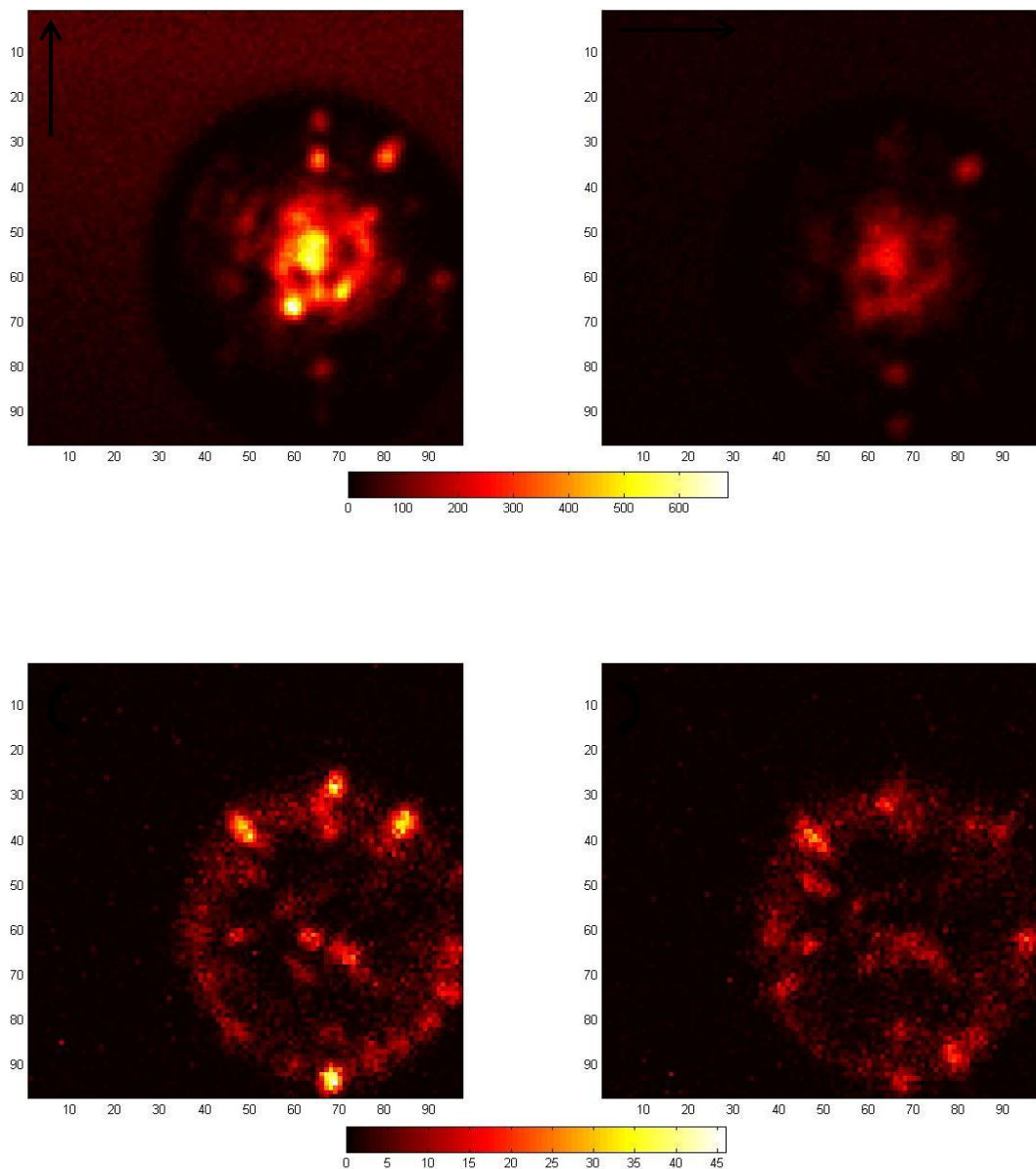


Figure 4.15: Top figure: TAG/CE image (site 2) taken with two linear polarizations perpendicular to one another. Bottom figure: TAG/CE image taken with left and right circular polarization. $z = 10 \mu\text{m}$.

Site 2 (3D, $z = 12 \mu\text{m}$)

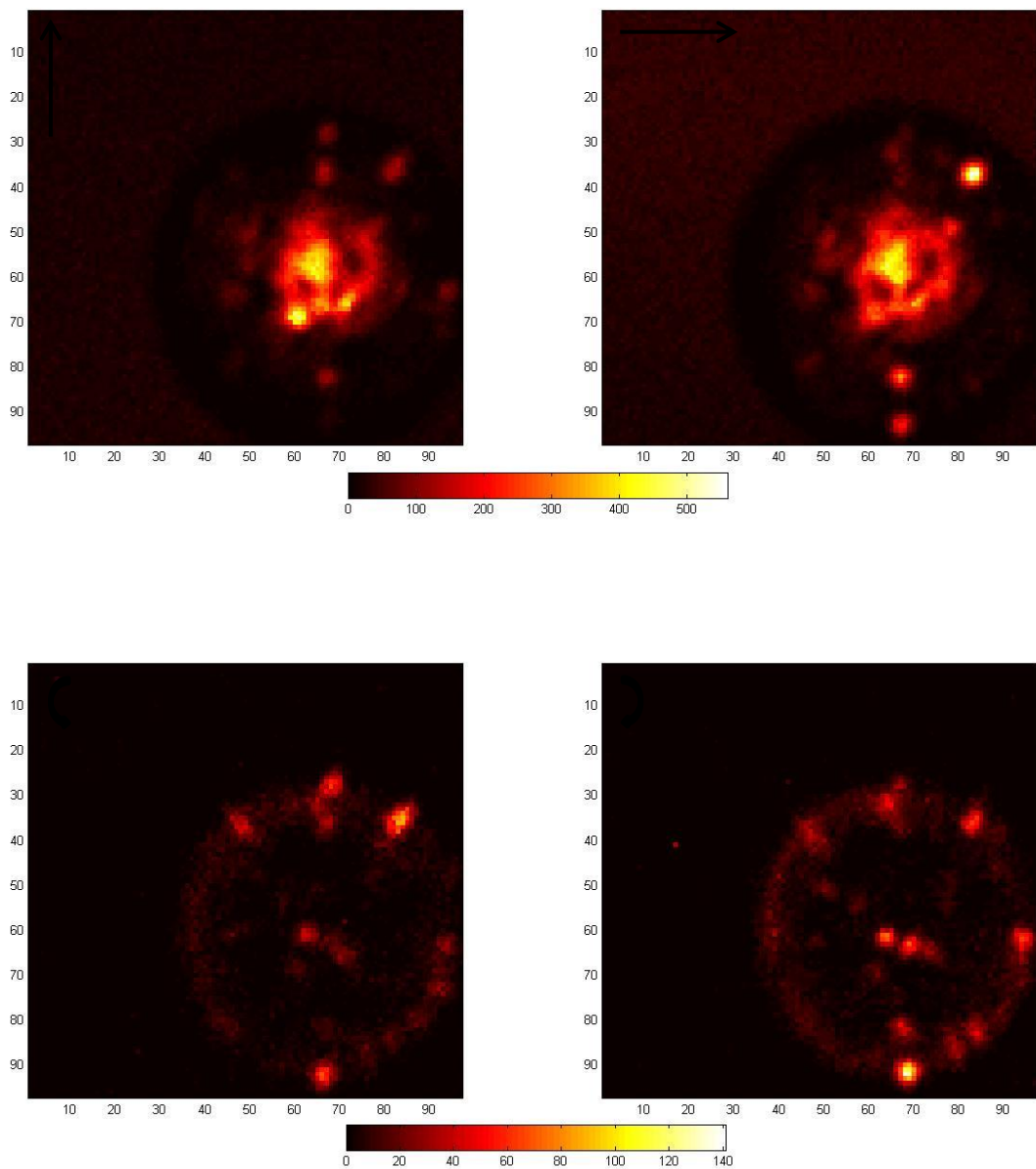


Figure 4.16: Top figure: TAG/CE image (site 2) taken with two linear polarizations perpendicular to one another. Bottom figure: TAG/CE image taken with left and right circular polarization. $z = 12 \mu\text{m}$.

Site 2 (3D, $z = 14 \mu\text{m}$)

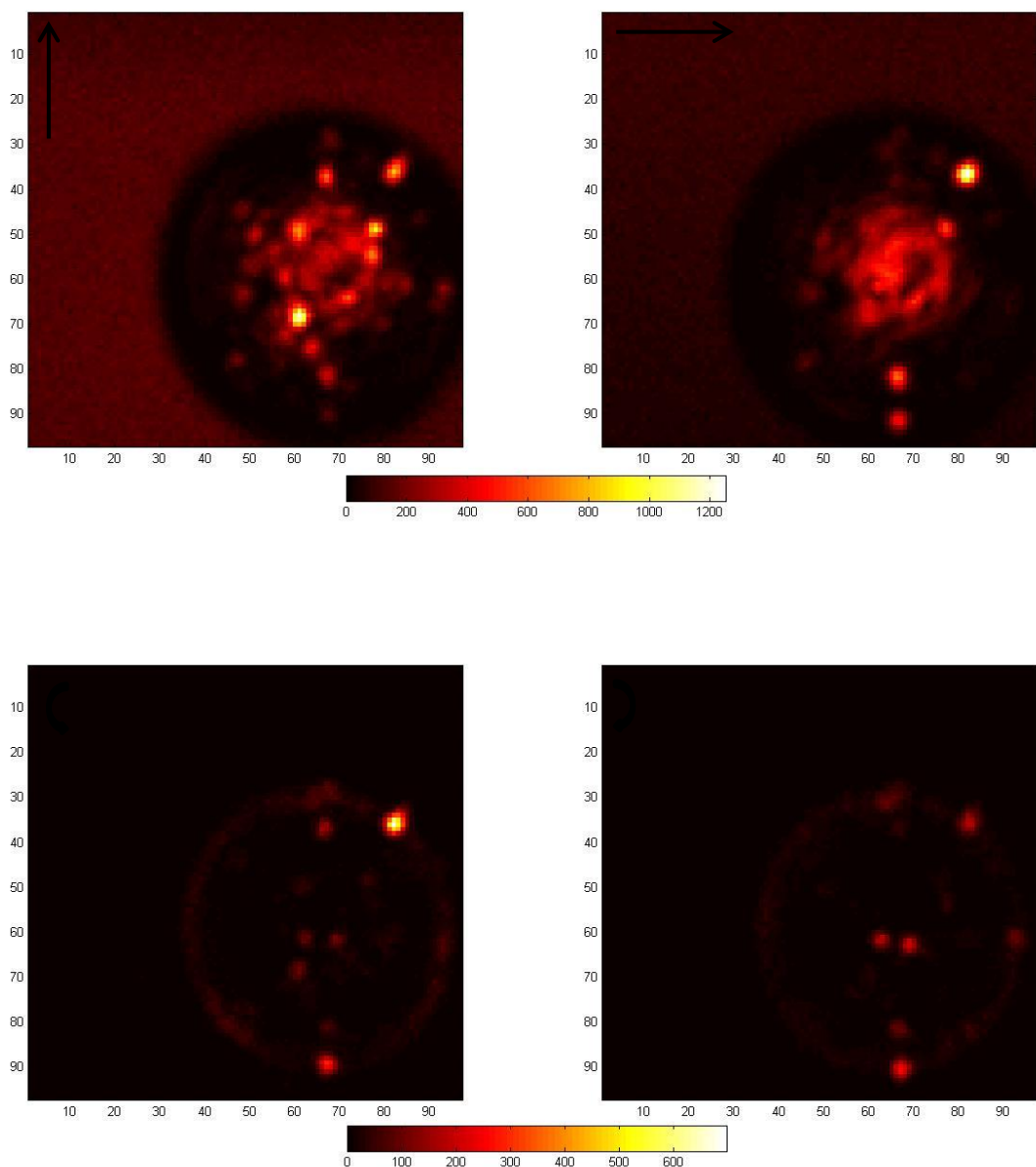


Figure 4.17 Top figure: TAG/CE image (site 2) taken with two linear polarizations perpendicular to one another. Bottom figure: TAG/CE image taken with left and right circular polarization. $z = 14 \mu\text{m}$.

Site 2 (3D, $z = 16 \mu\text{m}$)

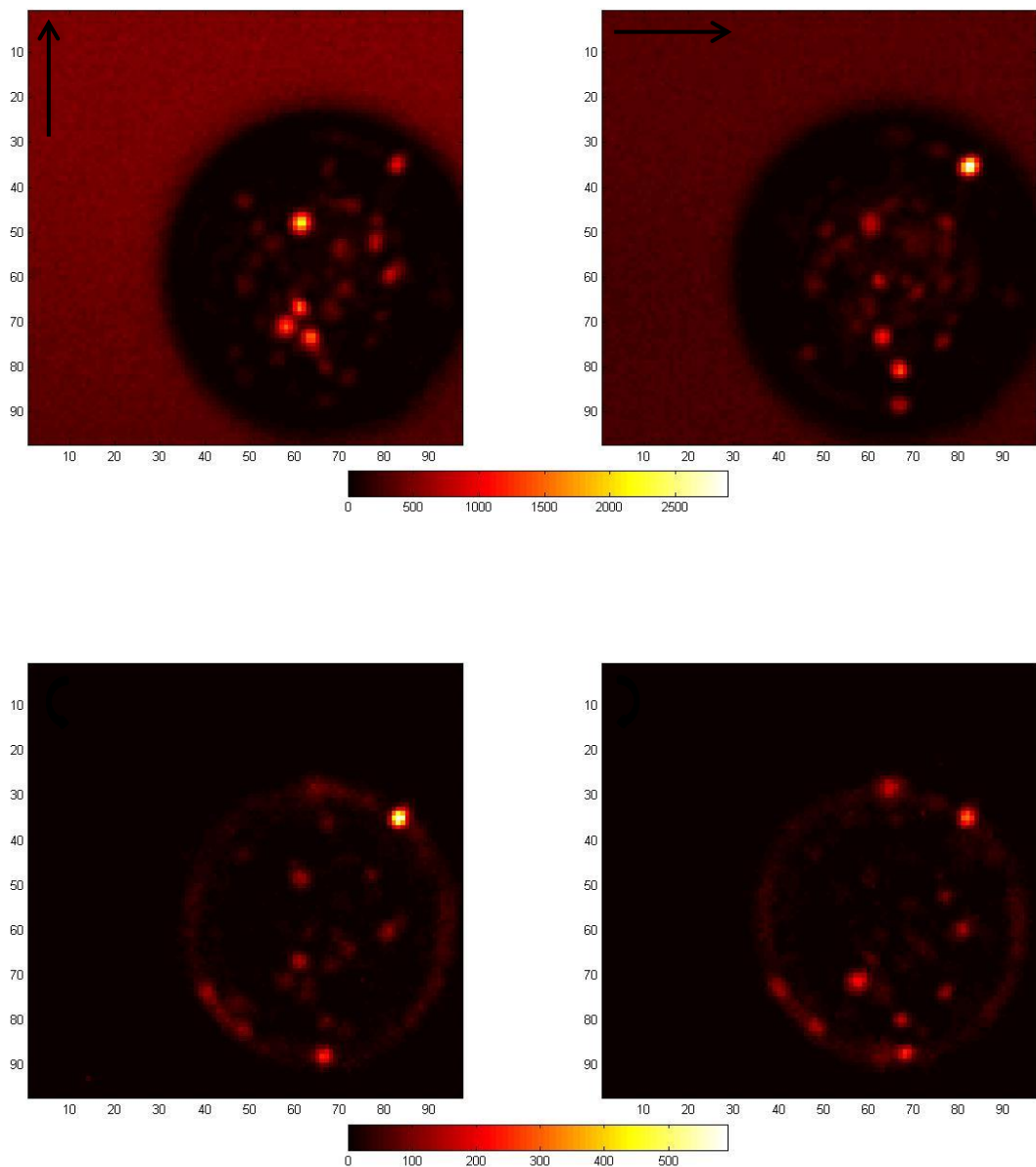


Figure 4.18: Top figure: TAG/CE image (site 2) taken with two linear polarizations perpendicular to one another. Bottom figure: TAG/CE image taken with left and right circular polarization. $z = 16 \mu\text{m}$.

Chapter 4: *Experimental THG imaging of various lipid samples and discussion*

As for all the previous images, linear P-THG images have the highest pixel values compared with circular P-THG images also in this case.

Site 2 shows a much complex behavior because we clearly notice the presence of micrometer-sized domains, i.e. very small LDs, along the boundary and within the core of the cluster. When using circular polarization, the edges lights up, whereas the central part becomes less visible. Although it is difficult to exactly establish the nature of these structures, we can hypothesize the simultaneous presence of small TAG and CE LDs, where the first tend to disappear when performing anisotropy measurements, i.e., if circular polarization is used.

In addition to the just presented TAG/CE images, for the plane $z = 16 \mu\text{m}$ in site 2 we also varied the linear polarization between two orthogonal directions. This lead to Figure 4.19, which is shown below.

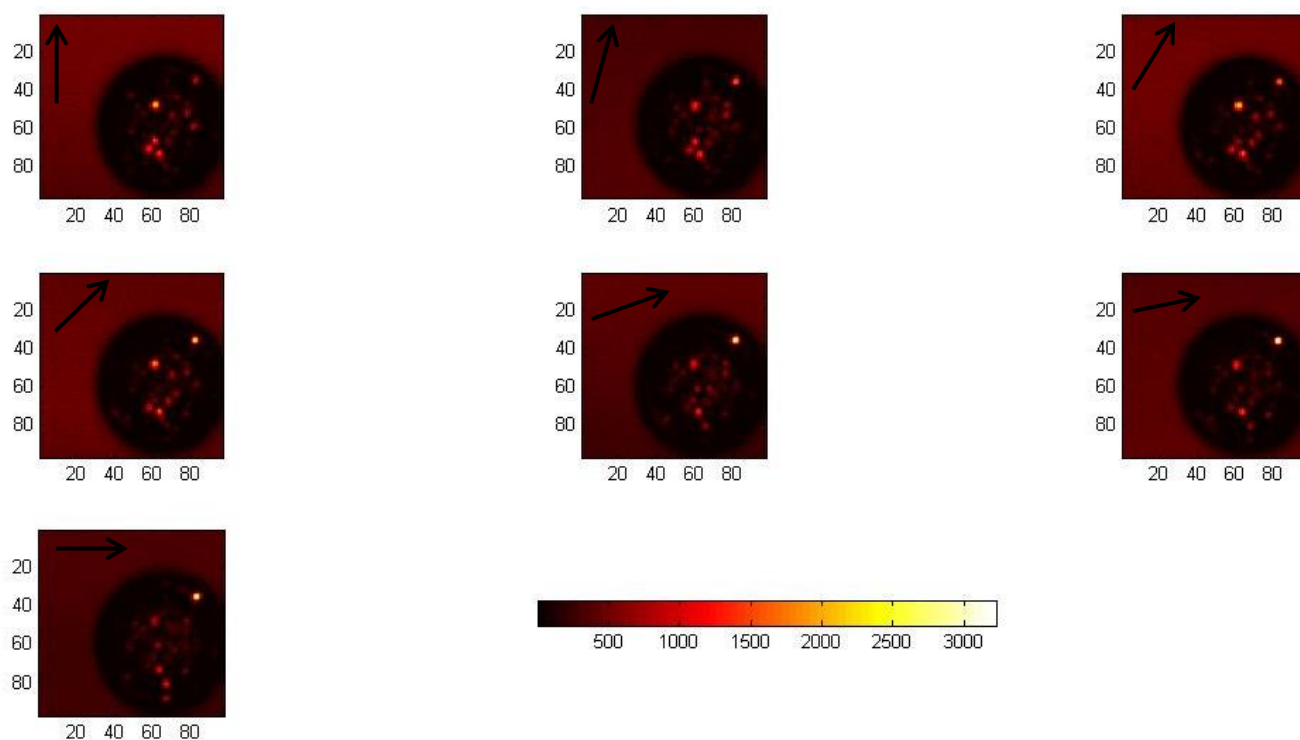


Figure 4.19: TAG/CE image taken by using linear polarization at different directions.

Chapter 4: *Experimental THG imaging of various lipid samples and discussion*

We notice that, as the direction of the linear polarization is varied, some structures of the sample become more visible and some other tend to disappear. This image shows that the sample is composed of crystalline domains, i.e. anisotropic regions, that of course respond differently depending on the direction of the electric field of the excitation beam. These domains present non-uniformities, in the sense that this sample does not behave as a single crystalline region, but indeed it exhibits areas each of which has a specific response to the linear polarization.

We have chosen to first present TAG images because TAG LDs are the most disordered ones, i.e. nearly isotropic. This is confirmed by the above results. Secondly, we showed images of the more disordered LDs, meaning CE and TAG/CE mixtures. We now move on to describe THG-CD images of LDs.

4.2 THG-CD imaging of LDs

In the following, THG circular dichroism (THG-CD) images are shown. These are computed according to (e.g. [62]):

$$THG - CD = \frac{I_{left-handed\ circ} - I_{right-handed\ circ}}{(I_{left-handed\ circ} + I_{right-handed\ circ})/2} \quad (4.1)$$

where $I_{left-handed\ circ}$ and $I_{right-handed\ circ}$ are the intensities of the pixels associated with a left- and right-handed circular polarizations, respectively. The normalization factor is simply the arithmetic mean of the two images. THG-CD are proved to give best image contrast in anisotropic samples.

4.2.1 TAG-enriched lipid droplets

Site 1

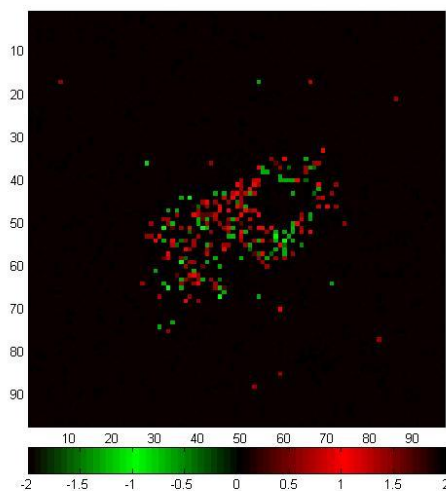


Figure 4.20: THG-CD image (site 1) of a TAG sample.

Site 2 (3D, $z = 10 \mu\text{m}$)

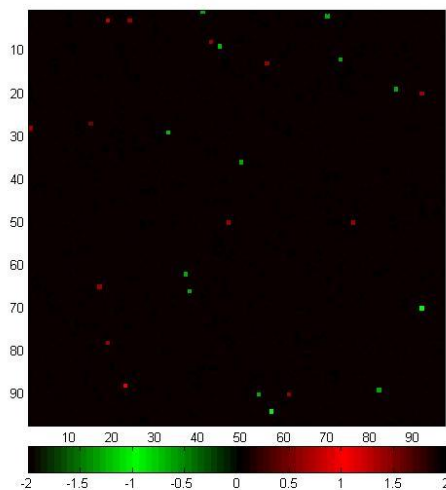


Figure 4.21: THG-CD image (site 2) of a TAG sample. $z = 10 \mu\text{m}$.

Site 2 (3D, $z = 12 \mu\text{m}$)

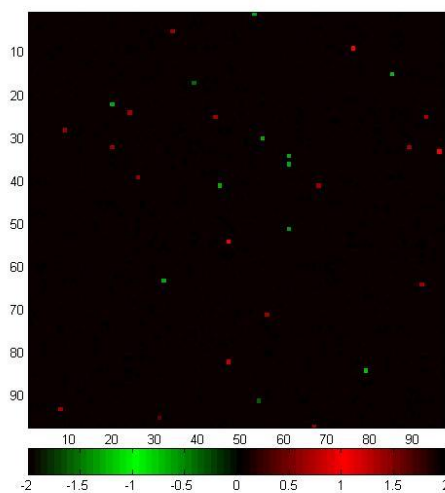


Figure 4.22: THG-CD image (site 2) of a TAG sample. $z = 12 \mu\text{m}$.

Site 2 (3D, $z = 14 \mu\text{m}$)

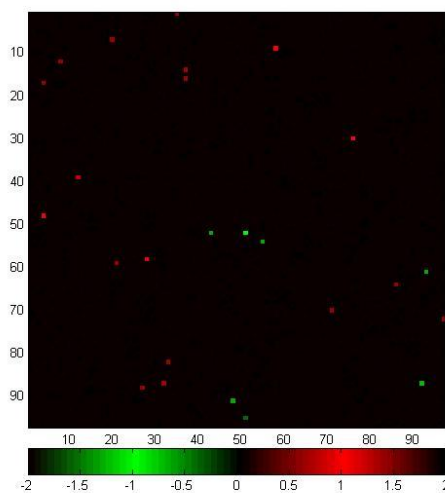


Figure 4.23: THG-CD image (site 2) of a TAG sample. $z = 14 \mu\text{m}$.

Chapter 4: *Experimental THG imaging of various lipid samples and discussion*

We first notice that THG-CD is a secondary effect, meaning that it is not directly available from the raw measured data, but instead it requires some simple processing operations on them.

It is important to point out that for a TAG LD sample, the THG-CD image is nearly blank, proving that TAG LDs are highly isotropic. This finding further confirms the results showed by the previous P-THG images of these LDs, that is, the high level of isotropy exhibited by TAG LDs.

4.2.2 CE-enriched lipid droplets

Site 1 (3D, $z = 8.4 \mu\text{m}$)

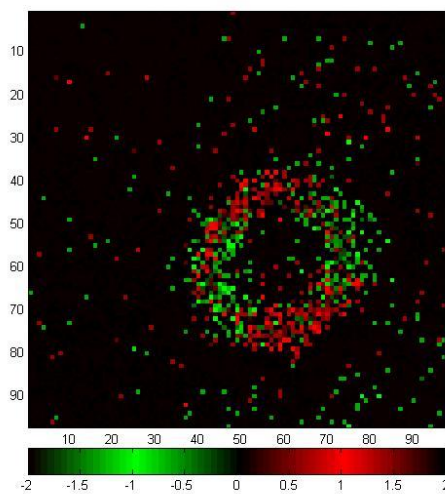


Figure 4.24: THG-CD image (site 1) of a CE sample. $z = 8.4 \mu\text{m}$.

Site 1 (3D, $z = 10.4 \mu\text{m}$)

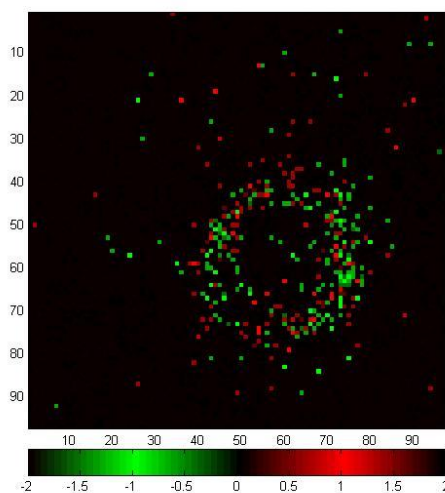


Figure 4.25: THG-CD image (site 1) of a CE sample. $z = 10.4 \mu\text{m}$.

Site 1 (3D, $z = 12.4 \mu\text{m}$)

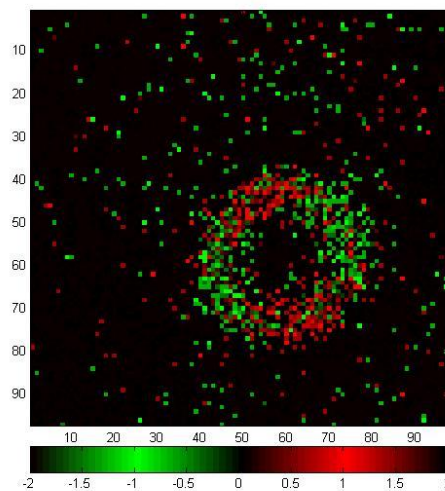


Figure 4.26: THG-CD image (site 1) of a CE sample. $z = 12.4 \mu\text{m}$.

Site 2 (3D, $z = 10 \mu\text{m}$)

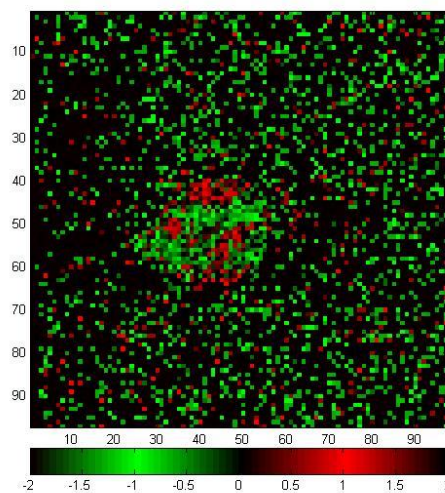


Figure 4.27: THG-CD image (site 2) of a CE sample. $z = 10 \mu\text{m}$.

Site 2 (3D, $z = 12 \mu\text{m}$)

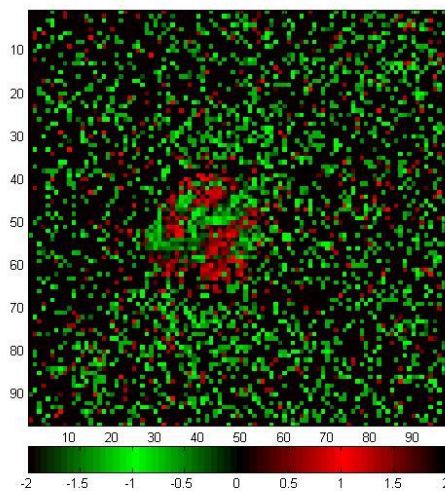


Figure 4.28: THG-CD image (site 2) of a CE sample. $z = 12 \mu\text{m}$.

Site 2 (3D, $z = 14 \mu\text{m}$)

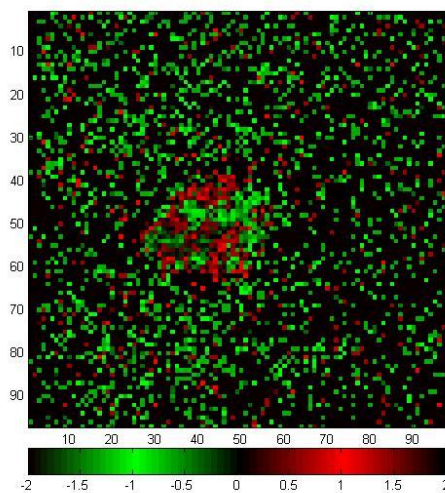


Figure 4.29: THG-CD image (site 2) of a CE sample. $z = 14 \mu\text{m}$.

Site 2 (3D, $z = 16 \mu\text{m}$)

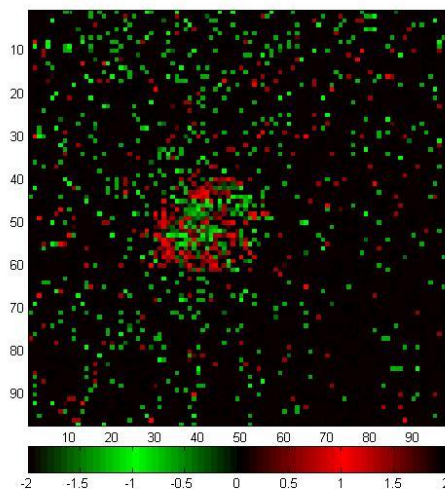


Figure 4.30: THG-CD image (site 2) of a CE sample. $z = 16 \mu\text{m}$.

Especially for site 1, we point out that THG-CD in the CE samples are usually more localized than signals from the TAG samples, meaning that they tend to organize themselves in clusters. In site 1 it is clear that these LDs form a characteristic domain with precise boundaries, which are the areas highlighted by the THG-CD imaging. As a result, we conclude that these areas of the sample exhibit high anisotropy. With regard to site 2, the CE molecules tend to be more ordered at the center of the droplet than at the edges.

4.2.3 Mixed TAG and CE-enriched lipid droplets

Site 1 (3D, $z = 8.5 \mu\text{m}$)

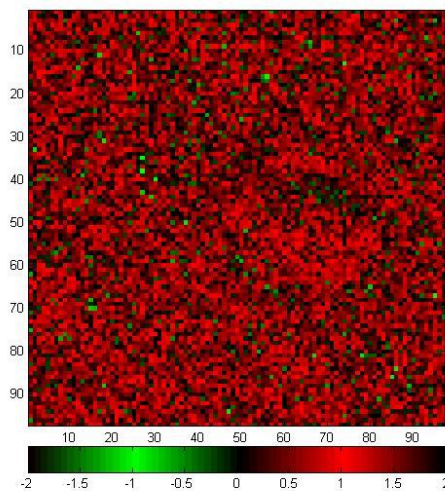


Figure 4.31: THG-CD image (site 1) of a TAG/CE sample. $z = 8.5 \mu\text{m}$.

Site 1 (3D, $z = 10 \mu\text{m}$)

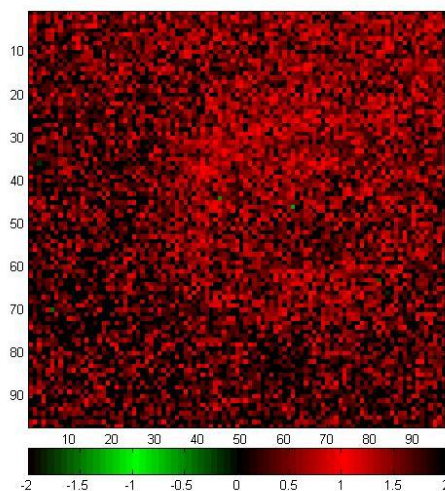


Figure 4.32: THG-CD image (site 1) of a TAG/CE sample. $z = 10 \mu\text{m}$.

Site 1 (3D, $z = 11.5 \mu\text{m}$)

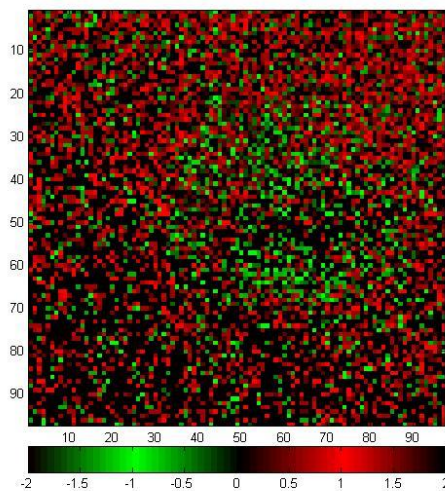


Figure 4.33: THG-CD image (site 1) of a TAG/CE sample. $z = 11.5 \mu\text{m}$.

Site 2 (3D, $z = 10 \mu\text{m}$)

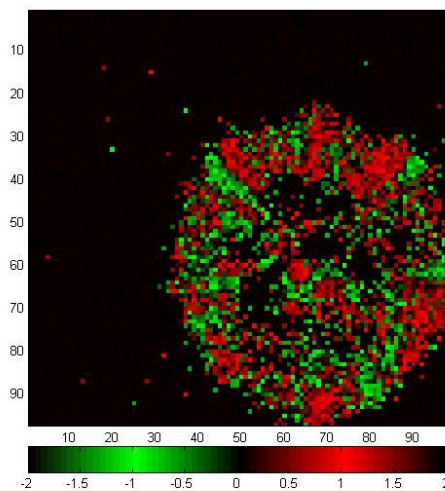


Figure 4.34: THG-CD image (site 2) of a TAG/CE sample. $z = 10 \mu\text{m}$.

Site 2 (3D, $z = 12 \mu\text{m}$)

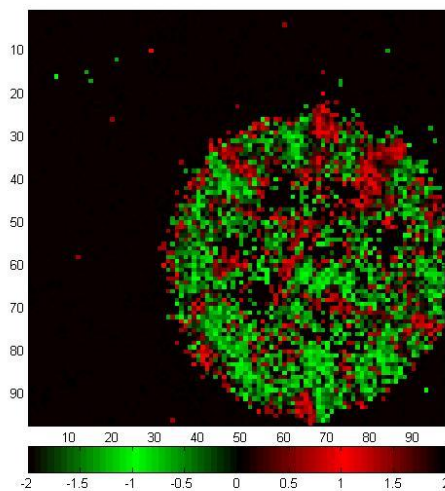


Figure 4.35: THG-CD image (site 2) of a TAG/CE sample. $z = 12 \mu\text{m}$.

Site 2 (3D, $z = 14 \mu\text{m}$)

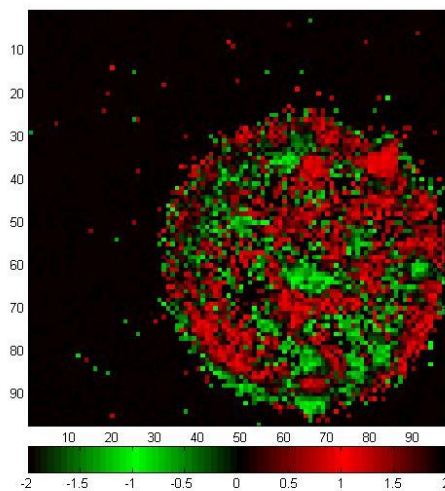


Figure 4.36: THG-CD image (site 2) of a TAG/CE sample. $z = 14 \mu\text{m}$.

Site 2 (3D, $z = 16 \mu\text{m}$)

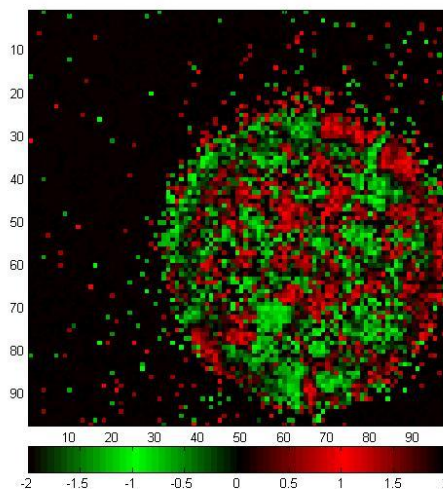


Figure 4.37: THG-CD image (site 2) of a TAG/CE sample. $z = 16 \mu\text{m}$.

Site 1 is composed of highly sparse TAG/CE LDs, as seen from the Figures. From the THG-CD imaging performed at different depths of this sample no structural differences along the z direction are notable, with the exception of a rounded cluster of LDs which slightly appears over the background for $z = 10 \mu\text{m}$. Overall, this site exhibits anisotropy because the associated THG-CD images are not blank. The degree of anisotropy is essentially determined by the CE LDs. We also notice that, for site 1, left circular polarization elicits a stronger THG response than right circular polarization does, i.e. red is prevalent over green in the THG-CD images.

As far as site 2 is concerned, it is basically a rounded cluster of TAG/CE LDs. From Figure 4.34 to Figure 4.37, we notice that black regions within the sample tend to disappear: this fact shows that CE effects may vary in 3D, as in such sample. In contrast, TAG's CD signals are always small even in 3D. The THG-CD images associated with site 2 confirms that the level of ordering of TAG/CE samples may be somehow thought as a weighted combination of the contributions coming from TAG LDs, i.e. mostly isotropic structures, and

those from CE LDs, i.e. anisotropic domains. The weights are tied to the relative concentration of TAG and CE LDs in the sample.

4.3 Polarized THG imaging of lipid films

After the THG microscopy studies of the above described LDs, we decided to characterize a more advanced biomedically relevant lipid assembly, i.e. a lipid film. These measurements are performed in order to gain insights on the behavior of LDs when they are assembled in a structure that mimics their ordering in a biological tissue.

The lipid film taken into consideration was composed of CE molecules. It was prepared by adding drop wise a CE solution (10 mg/ml in chloroform : methanol (9:1)) to a cover glass and by evaporating the solvent by nitrogen.

We now present P-THG images of a lipid film. The following set of images starts off with the comparison of five images taken at different depths with linear polarization. Then, circular P-THG images are presented.

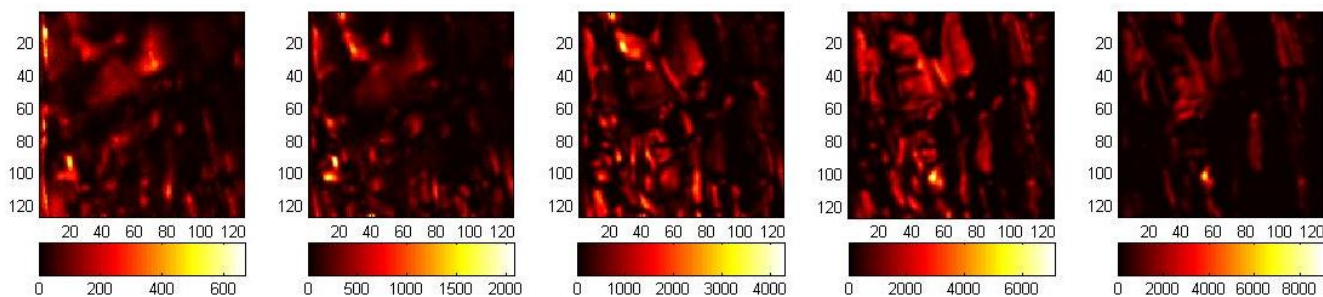


Figure 4.38: Image of a CE lipid film taken by keeping constant the direction of the linear polarization and by varying the plane of imaging. From left to right: $z = 8 \mu\text{m}$, $9 \mu\text{m}$, $10 \mu\text{m}$, $11 \mu\text{m}$, $12 \mu\text{m}$.

From Figure 4.38, it is possible to notice that a lipid film exhibits a much complex behavior when illuminated with a linearly polarized laser beam. Complexity is associated to the level of heterogeneities of the lipid sources that are illuminated within the focal volume [54]. Different structures light up when the plane of imaging is varied, showing that CE molecules response is dependent on the plane of imaging.

Chapter 4: *Experimental THG imaging of various lipid samples and discussion*

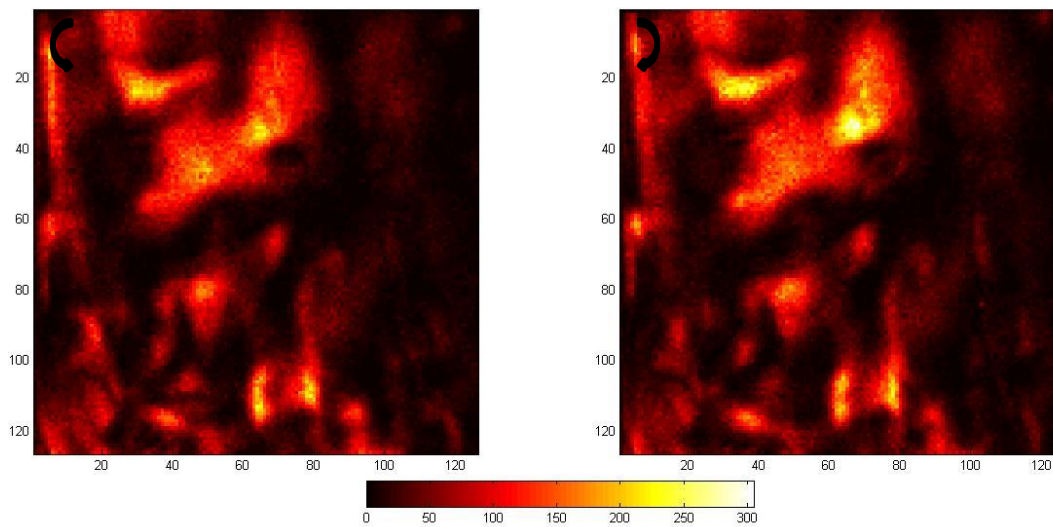


Figure 4.39: Image of a CE lipid film taken with left and right circular polarization. $z = 8 \mu\text{m}$.

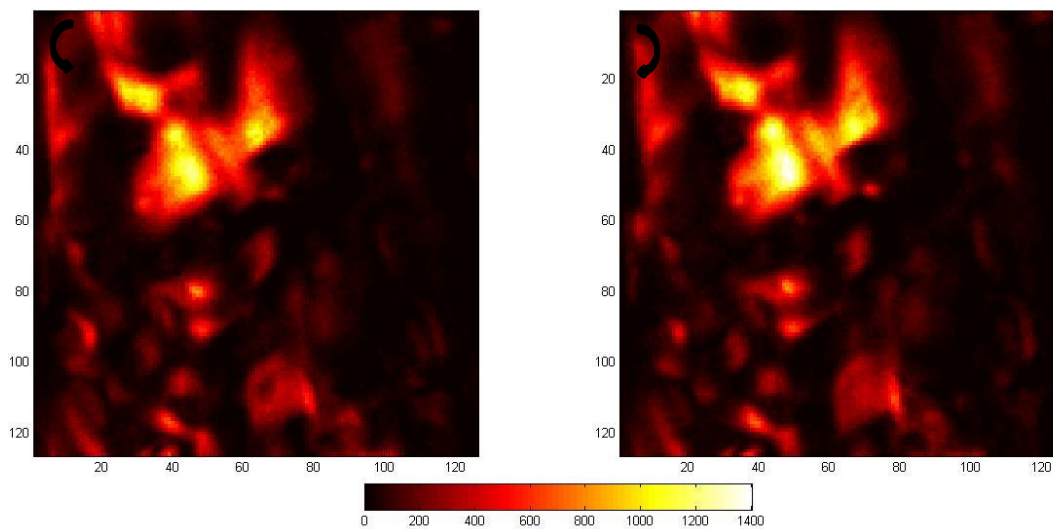


Figure 4.40: Image of a CE lipid film taken with left and right circular polarization. $z = 9 \mu\text{m}$.

Chapter 4: *Experimental THG imaging of various lipid samples and discussion*

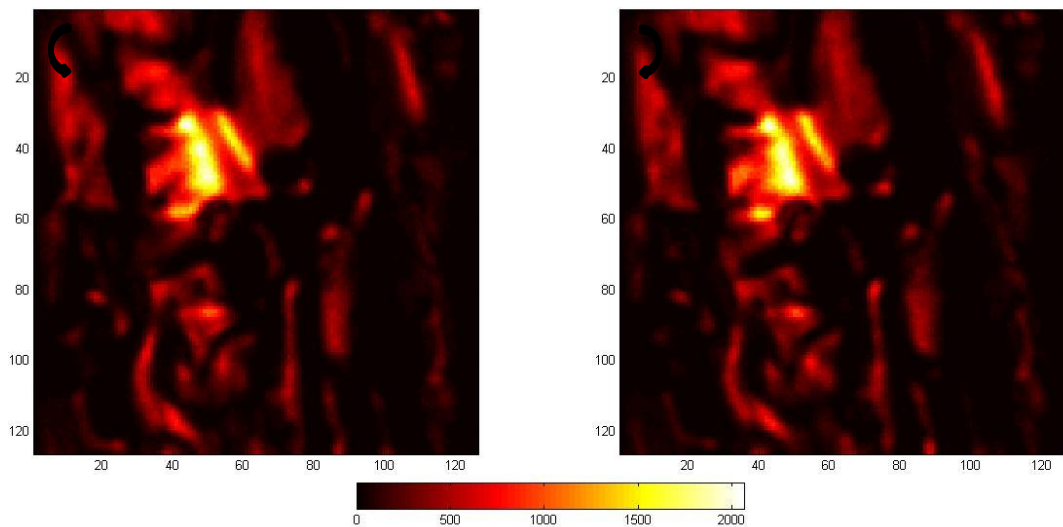


Figure 4.41: Image of a CE lipid film taken with left and right circular polarization. $z = 11 \mu\text{m}$.

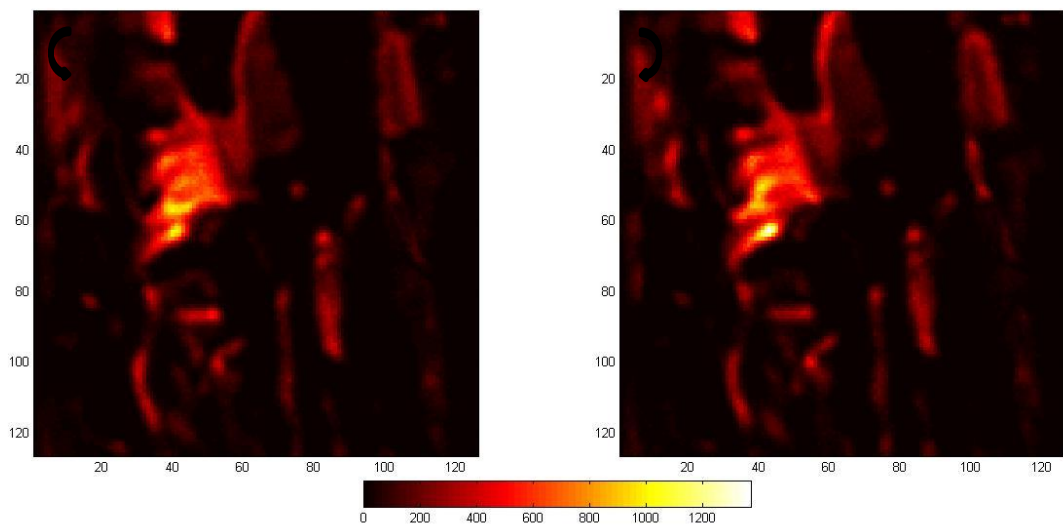


Figure 4.42: Image of a CE lipid film taken with left and right circular polarization. $z = 12 \mu\text{m}$.

The following is a THG-CD image of the CE lipid film at varying depth.

Chapter 4: *Experimental THG imaging of various lipid samples and discussion*

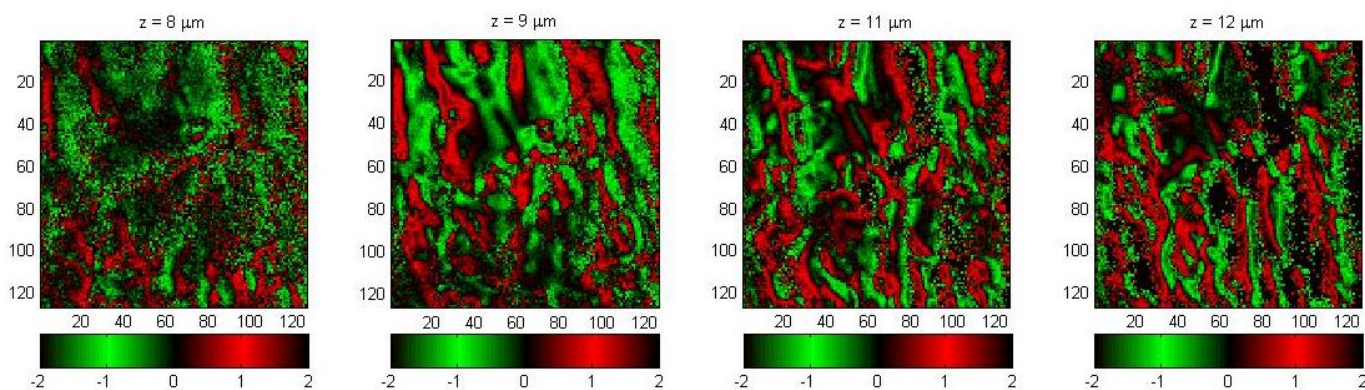


Figure 4.43: THG-CD image of a CE lipid film at varying depth z .

From the circular P-THG images we conclude that a CE lipid film is formed by micrometer-sized domains which are highly anisotropic. The THG-CD images show that this sample respond differently with respect to the direction of the circular polarization. In fact we notice the presence of both red and green regions; the first are associated with higher THG values for a left circular polarization than for a right one, whereas the other way around is true for the latter. These results suggest that the amount and symmetry of the scatterers within the focal volume have to be taken into account when considering the response of a given region within the sample. These factors determine the differences seen in the circular P-THG images of the CE lipid film.

The fourth chapter has experimentally showed that TAG LDs mostly form isotropic structures, whereas CE LDs anisotropic ones; in the case of a mixture TAG/CE LD sample, we found an intermediate behavior between the two previous situations. CE lipid films also exhibit a high level of ordering.

The next chapter presents conclusions, insights and future development of this work.

Chapter 5: Conclusions

We experimentally showed the possibility of probing the micrometer-scale arrangement of selected artificial lipid droplets by using polarization-dependent third-harmonic generation microscopy. In particular, we demonstrated that the use of incident circular polarization provides the best contrast in anisotropic samples.

The information drawn from the images can be used to study the level of ordering of lipid droplets in model systems, but also to gain insights on the arrangement of lipids in real biological tissues. The choice of imaging tryglycerides and cholesteryl esters makes this work particularly useful to model the lipid organization in the context of diseased tissues, especially in the case of tuberculosis (associated with tryglycerides) and atherosclerosis (associated with cholesteryl esters).

A promising future development would be the use of more complex model systems, which are able to better mimic real biological tissues. Moreover, the combination of THG imaging with other multiphoton techniques such as SHG or CARS represents an interesting challenge to study lipid structural properties.

Polarized THG imaging may also be used to characterize lipid droplets with more specific features, e.g. the presence of saturated bonds, the effect of fatty acid tails and the cis/trans transformations. With regard to this last feature, intuitively we expect the trans configuration to be more ordered than the cis; therefore, circular P-THG microscopy studies have the potential to detect changes in the cis/trans configuration for a given molecule.

At this point, THG microscopy is still not able to provide insights on the distribution and packing of lipids inside a cell. This fact is due to inherent convolution effects of the imaging

process, meaning that the maximum achievable spatial resolution is always limited by the point spread function of the imaging system.

In this sense we expect that THG microscopy combined with subdiffraction-limited focusing techniques could open in the future the possibility of studying and visualizing nanometer-sized regions of ordered lipids in cellular environments.

References

- [1] http://mhchem.org/221/COTW/fats_and_oils/FatsANDOils.html (visited on 2/6/2014)
- [2] K. Simons, J. L. Sampaio, “Membrane Organization and Lipid Rafts”, *Cold Spring Harb Perspect Biol* 2011; originally published online May 31, 2011.
- [3] F. D. Meyer, B. Smit, “Effect of cholesterol on the structure of a phospholipid bilayer”, *Proc Natl Acad Sci USA*. Mar 10, 2009; 106(10): 3654–3658, Published online Feb 18, 2009, *Applied Physical Sciences, Biophysics and Computational Biology*.
- [4] J. Pan, T. T. Mills, S. Tristram-Nagle, J. F. Nagle, “Cholesterol Perturbs Lipid Bilayers Nonuniversally”, *Phys Rev Lett*. Author manuscript; available in PMC Jun 12, 2009, Published online May 15, 2008.
- [5] K. Simons, G. van Meer, “Lipid sorting in epithelial cells”, *Biochemistry* 1988, Aug 23; 27(17):6197-202.
- [6] K. Simons, E. Ikonen, “Functional rafts and cell membranes”, *Nature* 387, 569-572, 5 June 1997.
- [7] T. Fujimoto, Y. Ohsaki, J. Cheng, M. Suzuki, Y. Shinohara, “Lipid droplets: a classic organelle with new outfits”, *Histochem Cell Biol* (2008) 130:263–279.
- [8] K. Tauchi-Sato, S. Ozeki, T. Houjou, R. Taguchi, T. Fujimoto, “The surface of lipid droplets is a phospholipid monolayer with a unique Fatty Acid composition”, *J. Biol. Chem.* 2002 Nov 15; 277(46):44507-12. Epub 2002 Sep 6.

References

- [9] S. Storey, A. McIntosh, S. Senthivinayagam, K. Moon, B. Atshaves, “The phospholipid monolayer associated with perilipin-enriched lipid droplets is a highly organized rigid membrane structure”, *Am. J. Physiol. Endocrinol Metab* 2011 Nov; 301(5):E991-E1003. Epub 2011 Aug 16.
- [10] T. Fujimoto, R. G. Parton, “Not Just Fat: The structure and function of the lipid droplet”, *Cold Spring Harb Perspect Biol* 2011; originally published online, January 26, 2011.
- [11] H. Wan, R. Melo, Z. Jin, A. Dvorak, P. Weller, “Roles and origins of leukocyte lipid bodies: proteomic and ultrastructural studies”, *FASEB J.* 2007 Jan; 21(1):167-78. Epub 2006 Nov 29.
- [12] L. Listenberger, X. Han, S. Lewis, S. Cases, R. Jr. Farese, D. Ory, J. Schaffer, “Triglyceride accumulation protects against fatty acid-induced lipotoxicity”, *Proc. Natl. Acad. Sci. USA* 2003 Mar 18; 100(6):3077-82. Epub 2003 Mar 10.
- [13] S. Jambunathan, J Yin, W. Khan, Y. Tamori, V. Puri, “FSP27 Promotes Lipid Droplet Clustering and Then Fusion to Regulate Triglyceride Accumulation”, *PLoS ONE* 6(12): e28614. Published: December 14, 2011.
- [14] M. Depla, R. Uzbekov, C. Hourieux, E. Blanchard, A. Le Gouge, L. Gillet, P. Roingeard, “Ultrastructural and quantitative analysis of the lipid droplet clustering induced by hepatitis C virus core protein”, *Cell. Mol. Life Sci.* 2010 Sep; 67(18):3151-61. Epub 2010 Apr 27.
- [15] A. S. Go, D. Mozaffarian, V. L. Roger, E. J. Benjamin, J. D. Berry, M. J. Blaha, S. Dai, E. S. Ford, C. S. Fox, S. Franco, H. J. Fullerton, C. Gillespie, S. M. Hailpern, J. A. Heit, V. J. Howard, M. D. Huffman, S. E. Judd, B. M. Kissela, S. J. Kittner, D. T. Lackland, J. H. Lichtman, L. D. Lisabeth, R. H. Mackey, D. J. Magid, G. M. Marcus, A. Marelli, D. B. Matchar, D. K. McGuire, E. R. Mohler III, C. S. Moy, M. E. Mussolino, R. W. Neumar, G.

References

Nichol, D. K. Pandey, N. P. Paynter, M. J. Reeves, P. D. Sorlie, J. Stein, A. Towfighi, T. N. Turan, S. S. Virani, N. D. Wong, D. Woo and M. B. Turner, “Heart Disease and Stroke Statistics--2014 Update: A Report From the American Heart Association”, *Circulation*. Published online December 18, 2013.

[16] J. Daniel, H. Maamar, C. Deb, T. Sirakova, P. Kolattukudy, “Mycobacterium tuberculosis uses host triacylglycerol to accumulate lipid droplets and acquires a dormancy-like phenotype in lipid-loaded macrophages”, *PLoS Pathog.* 2011 Jun;7(6): e1002093. Epub 2011 Jun 23.

[17] S. Ekman, B. Lundberg, “Phase diagrams of systems containing cholesterol, cholesteryl esters, and tryglycerides”, *Acta Chem. Scand.* B 30 (1976) No. 9.

[18] K. J. Williams, I. Tabas, “The Response-to-Retention Hypothesis of Early Atherogenesis”, *Arterioscler. Thromb. Vasc. Biol.* 1995 May; 15(5):551-61.

[19] D. Small, “Progression and regression of atherosclerotic lesions. Insights from lipid physical biochemistry”, *Arteriosclerosis* Volume 8, N. 2, March/April 1988.

[20] M. Nichols, N. Townsend, P. Scarborough, M. Rayner, “European cardiovascular disease statistics 2012 edition”, *European heart network and European society of cardiology*, September 2012.

[21] D. Engelman, G. Hillman, “Molecular organization of the cholesteryl ester droplets in the fatty streaks of human aorta”, *J. Clin. Invest.* Oct 1976; 58(4): 997–1007.

[22] D. Engelman, G. Hillman, “Compositional mapping of cholesteryl ester droplets in the fatty streaks of human aorta”, *J. Clin. Invest.* Oct 1976; 58(4): 1008-18.

References

- [23] J. Snow, H. McCloskey, J. Glick, G. Rothblat, M. Phillips, “Physical state of cholesteryl esters deposited in cultured macrophages”, *Biochemistry* 1988 May 17; 27(10):3640-6.
- [24] S. Lund-Katz, M. C. Phillips, “Packing of cholesterol molecules in human low-density lipoprotein”, *Biochemistry*, 1986, 25 (7), pp 1562–1568.
- [25] K. Li, C. Tihal, M. Guo, R. Stark, “Multinuclear and magic-angle spinning NMR investigations of molecular organization in phospholipid-triglyceride aqueous dispersions”, *Biochemistry* 1993 Sep 28; 32(38): 9926-35.
- [26] P. Horn, N. Ledbetter, C. James, W. Hoffman, C. Case, G. Verberck, K. Chapman, “Visualization of lipid droplet composition by direct organelle mass spectrometry”, *J. Biol. Chem*, 2011 Feb 4; 286(5):3298-306. Epub 2010 Nov 30.
- [27] D. Semwogerere, E. R. Weeks, “Confocal microscopy”, *Encyclopedia of Biomaterials and Biomedical Engineering*, Copyright 2005 by Taylor & Francis.
- [28] M. Minsky, “Memoir on inventing the confocal scanning microscope”, *Scanning*, vol. 10, pp. 128—138, 1988.
- [29] M. Dailey, E. Manders, D. Soll, M. Terasaki, “Confocal microscopy of living cells”, *Handbook of biological confocal microscopy*, 3rd edition, James Pawley ed., 1995.
- [30] X. Nan, J. Cheng, X. Xie, “Vibrational imaging of lipid droplets in live fibroblast cells with coherent anti-Stokes Raman scattering microscopy”, *J. Lipid Res.* 2003 Nov; 44(11):2202-8. Epub 2003 Aug 16.

References

- [31] A. Zumbusch, G. R. Holtom, X. S. Xie, “Three-Dimensional Vibrational Imaging by Coherent Anti-Stokes Raman Scattering”, *Phys. Rev. Lett.* 82, 4142 – Published 17 May 1999.
- [32] R. Carriles, D. Schafer, K. Sheetz, J. Field, R. Cisek, V. Barzda, A. Sylvester, J. Squier, “Imaging techniques for harmonic and multiphoton absorption fluorescence microscopy”, *Rev. Sci. Instrum.* 2009 Aug; 80(8): 081101.
- [33] T. Parasassi, E. Gratton, W. Yu, P. Wilson, M. Levi, “Two-photon fluorescence microscopy of laurdan generalized polarization domains in model and natural membranes”, *Biophys J.* Jun 1997; 72(6): 2413–2429.
- [34] X. Chen, O. Nadiarynkh, S. Plotnikov, P. Campagnola, “Second harmonic generation microscopy for quantitative analysis of collagen fibrillar structure”, *Nat. Protoc.* 2012 Mar 8; 7(4): 654-69.
- [35] R. Wampler, D. Kissick, C. Dehen, E. Gualtieri, J. Grey, H. Wang, D. Thompson, J. Cheng, G. Simpson, “Selective detection of protein crystals by second harmonic microscopy”, *J. Am. Chem. Soc.* 2008 Oct 29; 130(43): 14076-7. Epub 2008 Oct 3.
- [36] J. Suhalim, C. chung, M. Lilledahl, R. Lim, M. Levi, B. Tromberg, E. Potma, “Characterization of cholesterol crystals in atherosclerotic plaques using stimulated Raman scattering and second-harmonic generation microscopy”, *Biophys. J.* 2012 Apr 18; 102(8): 1988-95.
- [37] H. Lee, M. Huttunen, K. Hsu, M. Partanen, G. Zhuo, M. Kauranen, S. Chu, “Chiral imaging of collagen by second-harmonic generation circular dichroism”, *Biomed. Opt. Express* 2013 May 20 ;4(6):909-16.

References

- [38] D. Débarre, W. Supatto, A. Pena, A. Fabre, T. Tordjman, L. Combettes, M. Schanne-Klein, E. Beaurepaire, “Imaging lipid bodies in cells and tissues using third-harmonic generation microscopy”, *Nature Methods*, vol. 3 n.1, January 2006.
- [39] M. Zimmerley, P. Mahou, D. Débarre, M. Schanne—Klein, E. Beaurepaire, “Probing ordered lipid assemblies with polarized third-harmonic generation microscopy”, *American physical society*, 2160-3308/13/3(1)/011002(16), published 14 January 2013.
- [40] H. Rinia, K. Burger, M. Bonn, M. Müller, “Quantitative label-free imaging of lipid composition and packing of individual cellular lipid droplets using multiplex CARS microscopy”, *Biophys. J.* 2008 Nov 15; 95(10): 4908-14. Epub 2008 Aug 8.
- [41] W. R. Zipfel, R. M. Williams, W. W. Webb, “Nonlinear magic: multiphoton microscopy in the biosciences”, *Nature Biotechnology*, vol. 21 n.11, November 2003.
- [42] F. Helmchen, W. Denk, “Deep tissue two-photon microscopy”, *Nature Methods*, vol.2 n.12, December 2005.
- [43] E. Wolf, “Electromagnetic diffraction in optical systems. I: An integral representation of the image field”, *D. Gabor, F.S.R.*, 4 June 1959.
- [44] J. Squier, M. Müller, “High resolution nonlinear microscopy: a review of sources and methods for achieving optimal imaging”, *Rev. Sci. Instrum.* 72, 2855 (2001).
- [45] V. Centoze, J. White, “Multiphoton excitation provides optical sections from deeper within scattering specimens than confocal imaging”, *Biophys. J.* 1998 Oct; 75(4): 2015-24.
- [46] R. W. Boyd, “Nonlinear optics”, third edition, April 2008.

References

- [47] T. Y. F. Tsang, "Optical third-harmonic generation at interfaces", *Phys. Rev. A* 52, 4116-4125 (1995).
- [48] Y. Barad, H. Eisenberg, M. Horowitz, Y. Silberberg, "Nonlinear scanning laser microscopy by third harmonic generation", *Appl. Phys. Lett.* 70, 922 (1997).
- [49] J. Squier, M. Müller, G. J. Brakenhoff, K. R. Wilson, "Third harmonic generation microscopy", *Optics Express* 315, Vol. 3, No. 9, 26 October 1998.
- [50] V. V. Yakovlev, S. V. Govorkov, "Diagnostics of surface layer disordering using optical third harmonic generation of a circular polarized light", *Applied Physics Letters*, 0003-6951/2001/79(25)/4136/3, 11 October 2001.
- [51] N. Olivier, F. Aptel, K. Plamann, M. C. Schanne-Klein, E. Beaufort, "Harmonic microscopy of isotropic and anisotropic microstructure of the human cornea", *Optics Express*, vol. 18, No. 5, 1 March 2010.
- [52] D. Oron, E. Tal, Y. Silberberg, "Depth-resolved multiphoton polarization microscopy by third harmonic generation", *Optics Letters*, Vol. 28, No. 23, 1 December 2003.
- [53] D. Oron, D. Yelin, E. Tal, S. Raz, R. Fachima, Y. Silberberg, "Depth-resolved structural imaging by third harmonic generation microscopy", *Journal of Structural Biology*, 23 June 2003.
- [54] D. Débarre, W. Supatto, E. Beaufort, "Structure sensitivity in third harmonic generation microscopy", *Optics Letters*, Vol. 30, No. 16, 15 August 2005.

References

- [55] D. Débarre, W. Supatto, A. Pena, A. Fabre, T. Tordjmann, L. Combettes, M. Schanne-Klein, E. Beaurepaire, “Imaging lipid bodies in cells and tissues using third-harmonic generation microscopy”, *Nature Methods*, Vol. 3, No. 1, January 2006.
- [56] M. Zimmerley, P. Mahou, D. Débarre, M. Schanne-Klein, E. Beaurepaire, “Probing ordered lipid assemblies with polarized third harmonic generation”, *Physical Review*, 2160-3308/13/3(1)/011002(16), 14 January 2013.
- [57] F. Kajzar, J. Messier, “Third harmonic generation in liquids”, *Phys. Rev. A* 32, 2352. Published 1 October 1985.
- [58] M. Huttunen, “Second-harmonic generation with focused vector beams”, Thesis for the degree of Doctor of Science in Technology at Tampere University of Technology, Finland, 2013.
- [59] F. Gunstone, “Fatty acid and lipid chemistry”, Glasgow, Blackie Academic & Professional, 1996, 1-34.
- [60] http://www.siumed.edu/~bbartholomew/course_material/protein_methods.htm (visited on 4/6/2014)
- [61] S. Adelman, J. Glick, M. Phillips, G. Rothblat, “Lipid composition and physical state effects on cellular cholesteryl ester clearance”, *J. Biol. Chem.*, 1984 Nov 25; 259(25): 13844-50.
- [62] T. Verbiest, S. V. Elshocht, S. Sioncke, M. Kauranen, A. Persoons, K. U. Leuven, “Circular-difference effects in second-harmonic generation from thin films”, Conference paper, *Organic thin films*, Santa Clara, California, September 24, 1999.